PLANETARY SCIENCE

Compositionally and density stratified igneous terrain in Jezero crater, Mars

Copyright © 2022 The Authors, some rights reserved; exclusive licensee American Association for the Advancement of Science. No claim to original U.S. Government Works. Distributed under a Creative Commons Attribution NonCommercial License 4.0 (CC BY-NC).

Roger C. Wiens[1]†*, Arya Udry[2], Olivier Beyssac[3], Cathy Quantin-Nataf[4], Nicolas Mangold[5], Agnès Cousin[6], Lucia Mandon[7], Tanja Bosak[8], Olivier Forni[6], Scott M. McLennan[9], Violaine Sautter[3], Adrian Brown[10], Karim Benzerara[3], Jeffrey R. Johnson[11], Lisa Mayhew[12], Sylvestre Maurice[6], Ryan B. Anderson[13], Samuel M. Clegg[1], Larry Crumpler[14], Travis S. J. Gabriel[13], Patrick Gasda[1], James Hall[8], Briony H. N. Horgan[15], Linda Kah[16], Carey Legett IV[1], Juan Manuel Madariaga[17], Pierre-Yves Meslin[6], Ann M. Ollila[1], Francois Poulet[18], Clement Royer[7], Shiv K. Sharma[19], Sandra Siljeström[20], Justin I. Simon[21], Tayro E. Acosta-Maeda[19], Cesar Alvarez-Llamas[22], S. Michael Angel[23], Gorka Arana[17], Pierre Beck[24], Sylvain Bernard[3], Tanguy Bertrand[7], Bruno Bousquet[25], Kepa Castro[17], Baptiste Chide[1], Elise Clavé[25], Ed Cloutis[26], Stephanie Connell[26], Erwin Dehouck[4], Gilles Dromart[4], Woodward Fischer[27], Thierry Fouchet[7], Raymond Francis[28], Jens Frydenvang[29], Olivier Gasnault[6], Erin Gibbons[30], Sanjeev Gupta[31], Elisabeth M. Hausrath[2], Xavier Jacob[32], Hemani Kalucha[27], Evan Kelly[19], Elise Knutsen[33], Nina Lanza[1], Javier Laserna[22], Jeremie Lasue[6], Stéphane Le Mouélic[5], Richard Leveille[30], Guillermo Lopez Reyes[34], Ralph Lorenz[11], Jose Antonio Manrique[34], Jesus Martinez-Frias[35], Tim McConnochie[36], Noureddine Melikechi[37], David Mimoun[38], Franck Montmessin[33], Javier Moros[22], Naomi Murdoch[38], Paolo Pilleri[6], Cedric Pilorget[18], Patrick Pinet[6], William Rapin[6], Fernando Rull[34], Susanne Schröder[39], David L. Shuster[40], Rebecca J. Smith[9], Alexander E. Stott[38], Jesse Tarnas[28], Nathalie Turenne[26], Marco Veneranda[34], David S. Vogt[39], Benjamin P. Weiss[8], Peter Willis[28], Kathryn M. Stack[28], Kenneth H. Williford[28,41], Kenneth A. Farley[27], The SuperCam Team‡

Before Perseverance, Jezero crater's floor was variably hypothesized to have a lacustrine, lava, volcanic airfall, or aeolian origin. SuperCam observations in the first 286 Mars days on Mars revealed a volcanic and intrusive terrain with compositional and density stratification. The dominant lithology along the traverse is basaltic, with plagioclase enrichment in stratigraphically higher locations. Stratigraphically lower, layered rocks are richer in normative pyroxene. The lowest observed unit has the highest inferred density and is olivine-rich with coarse (1.5 millimeters) euhedral, relatively unweathered grains, suggesting a cumulate origin. This is the first martian cumulate and shows similarities to martian meteorites, which also express olivine disequilibrium. Alteration materials including carbonates, sulfates, perchlorates, hydrated silicates, and iron oxides are pervasive but low in abundance, suggesting relatively brief lacustrine conditions. Orbital observations link the Jezero floor lithology to the broader Nili-Syrtis region, suggesting that density-driven compositional stratification is a regional characteristic.

Downloaded from https://www.science.org on November 01, 2022

INTRODUCTION

Jezero crater was selected as the landing site of the Perseverance rover based on strong astrobiological potential and attributes important for sample return (*1*). Jezero is located (18.4°N, 77.5°E) near the western edge of Isidis Planitia and east of Nili Fossae in Noachian terrain. Orbital images indicate that this crater hosted a lake with two major inlet channels and one outlet channel, suggested to be fluvially active as early as the late Noachian period (*2*). The western sedimentary fan was recently confirmed as a delta deposited within a lake with fluctuating water levels (*3*). These features suggest a formerly habitable environment with a high biosignature preservation potential, motivating exploration and plans for sample return. Moreover, constraining the time period(s) of fluvial activity at Jezero could provide important information about the timing of global fluvial activity on Mars. Jezero also contains the largest, most obvious deposits of carbonates detected on Mars from orbit that typically exhibit strong olivine signatures as well (*4*–*10*). Surface exploration of these deposits could yield unique insights into the climate history and carbon cycle of Mars. Specifically, a formerly water-rich planet with a CO_2-dominated atmosphere should have left ubiquitous carbonate deposits (*11*), but these are unexpectedly sparse. Exploration of the existing carbonates at Jezero and the specific conditions that produced these carbonates should help understand the common association of carbonate and olivine signals in orbital spectra and the processes that formed the rare carbonate deposits on Mars. Last, Jezero crater has been suggested to contain an igneous mafic floor unit (*7*, *8*, *10*–*17*), which may facilitate the return of radiometrically datable samples to calibrate Mars' crater-derived surface ages, as well as a high priority for sample return (*18*, *19*). However, before the landing of the Perseverance rover, the origin of the units on Jezero crater's floor remained debated; earlier igneous interpretations (*7*, *8*, *12*, *13*, *20*) were called into question in favor of ashfall, aeolian, or sedimentary emplacement [e.g., (*15*–*17*)].

Here, we present the first mineralogy and chemistry results of SuperCam observations made along the rover traverse in the mission's first 286 solar days (sols) on Mars (e.g., to mid-December 2021). SuperCam coaligned observations include the first surface-based near–infrared (IR) reflectance spectra in the 1.3 to 2.6 μm range

along with visible-range (VIS) spectra (0.4 to 0.85 μm), elemental compositions obtained by laser-induced breakdown spectroscopy (LIBS), remote time-resolved Raman spectra, and the rover's highest-resolution remote images using SuperCam's remote micro-imager (RMI) (*21–23*). More than 1450 observations for chemistry and a similar number of VISIR (VIS+IR) reflectance spectra on >180 targets up to Sol 286 provide a record of chemical and mineral compositions and alteration at nearly every rover stop along the traverse (Fig. 1A). These observations reveal the igneous nature of the rocks encountered so far, which shows a gradient toward progressively more mafic compositions with lower stratigraphic position, and a generally low level of aqueous alteration.

RESULTS

Geological description and stratigraphic nomenclature

Initial observations of mineralogy and chemistry were made at the Octavia E. Butler (OEB) landing site, ~2.2 km southeast of the nearest deposits of the main delta formation (fm) (*3*). OEB is on the western edge of a geologic unit that is relatively homogeneous in morphology as seen from orbit and covers nearly 400 km^2 (*14*) of the Jezero crater surface (Fig. 1A). This relatively thin (~13 m) (*14*) stratigraphic unit exhibits a rough surface texture and distinctive lobate margins. It has been mapped recently (*15–17*) as the crater floor fractured rough (Cf-fr) unit and is called the Máaz fm (*24*) in the region of the initial rover traverse (Fig. 1A). Just west of OEB lies an exposure of a stratigraphically lower unit visible as an inlier in the Máaz fm. The unit exhibits layered ridges and was mapped from orbit as the crater floor fractured (Cf-f-1) unit and is informally called "Séítah" ("among the sand" in Navajo) by the Perseverance team. From OEB, Perseverance traveled ~1.5 km south until it rounded the southernmost point of Séítah (Fig. 1A). From there and after producing and making observations on an abrasion patch ("Guillaumes"), Perseverance traveled ~1 km northwest below and along an exposed ridge ("Artuby") that protrudes above Séítah, producing and observing another abrasion patch ("Bellegarde") and collecting two samples at the same location at the top of the ridge (Fig. 1A). Thereafter, Perseverance entered Séítah and explored this unit until Sol 340, producing and observing two more abrasion patches ("Garde" and "Dourbes") and collecting four more samples.

The crater floor surface is relatively flat in the area covered in the rover's first 286 sols. Elevations along the initial southward traverse ranged from −2570 m at OEB down to −2583 m at Rochette on Sol 168, at the southern tip of Séítah (Fig. 1A). The trough along the southwest edge of Séítah is at the same general elevation. For example, the rover was at −2584 m on Sol 171. The top of Artuby ridge is as high as −2580 m. On the northeast side of the trough, Séítah is actually higher than Artuby ridge in most locations, as shown in the topographic profile in Fig. 1, ranging from −2574 to −2568 m. The slightly higher elevations of Séítah relative to the Máaz fm were also noted before the landing [e.g., (*15*)]. Surface observations show that strata along Artuby ridge dip to the south-southwest, away from Séítah, by up to ~10°. Observations made by the Radar Imager for Mars' Subsurface Experiment (RIMFAX) confirm this dip and indicate further that rocks dip away from Séítah on all sides, observed on traverses on sols 135 (east of Séítah), 168 to 170 (south), 180 (southwest), and 200 to 202 [southwest; (*25*)].

The Mars 2020 team has adopted a nomenclature for the region traversed thus far by the rover, in which the Máaz fm (Fig. 1A) is divided into several members based on morphology (*24*). We found that adjacent morphological members in the early part of the traverse (to Sol 173) are compositionally indistinguishable, and so we refer to all rocks in this eastern area as "Máaz." We make a distinction between lighter-toned flat rocks ("pavers") and darker, higher-standing rocks ("Ch'al-like"), the latter in reference to a member proposed (*24*) to consist of massive high-standing rocks to the east of the traverse (text S1), which were sampled later, on the return route, not covered in this work. Starting at Sol 177, SuperCam observed variably recessive layered outcrops below Artuby ridge (Fig. 1A) and massive outcrops at the top of the ridge (*26*). As we show later, both members have similar compositions that are distinct from that of Máaz, so we group these together as Artuby observations. References to Máaz fm compositions in this paper exclude observations along Artuby ridge, which are distinct. Last, we use the designation of Séítah fm for all rocks from sols 202 to 286 except for observations of six pitted targets that are part

[1]Space and Planetary Exploration Team, Los Alamos National Laboratory, Los Alamos, NM, USA. [2]Department of Geoscience, University of Nevada Las Vegas, Las Vegas, NV, USA. [3]Institut de Minéralogie, de Physique des Matériaux et de Cosmochimie, CNRS, Sorbonne Université, Muséum National d'Histoire Naturelle, Paris, France. [4]Laboratoire de Géologie de Lyon, Université de Lyon, Université Claude Bernard Lyon1, Ecole Normale Supérieure de Lyon, Université Jean Monnet Saint Etienne, CNRS, Villeurbanne, France. [5]Laboratoire de Planétologie et Géosciences, CNRS UMR 6112, Nantes Université, Université d'Angers, Université du Mans, Nantes, France. [6]Institut de Recherche en Astrophysique et Planetologie (IRAP), Université de Toulouse 3 Paul Sabatier, UPS, CNRS, CNES, Toulouse, France. [7]Laboratoire d'Etudes Spatiales et d'Instrumentation en Astrophysique, Observatoire de Paris-PSL, CNRS, Sorbonne Université, Université de Paris Cité, Meudon, France. [8]Earth, Atmospheric, and Planetary Sciences, Massachusetts Institute of Technology, Cambridge, MA, USA. [9]Stony Brook University, Stony Brook, NY, USA. [10]Plancius Research, Severna Park, MD, USA. [11]Space Exploration Sector, Johns Hopkins University Applied Physics Laboratory, Laurel, MD, USA. [12]Department of Geological Sciences, University of Colorado, Boulder, CO, USA. [13]U.S. Geological Survey Astrogeology Science Center, Flagstaff, AZ, USA. [14]New Mexico Museum of Natural History, Albuquerque, NM, USA. [15]Earth, Atmospheric, and Planetary Sciences, Purdue University, West Lafayette, IN, USA. [16]Earth and Planetary Sciences, University of Tennessee, Knoxville, TN, USA. [17]University of Basque Country, UPV/EHU, Leioa, Bilbao, Spain. [18]Institut d'Astrophysique Spatiale, CNRS, Univ. Paris-Saclay, Orsay, France. [19]University of Hawai'i, Honolulu, HI, USA. [20]RISE Research Institutes of Sweden, Stockholm, Sweden. [21]Center for Isotope Cosmochemistry and Geochronology, NASA Johnson Space Center, Houston, TX, USA. [22]Universidad de Malaga, Malaga, Spain. [23]Department of Chemistry and Biochemistry, University of South Carolina, Columbia, SC, USA. [24]Institut de Planétologie et d'Astrophysique de Grenoble, CNRS, Université Grenoble Alpes, Grenoble, France. [25]Centre Lasers Intenses et Applications, CNRS, CEA, Université de Bordeaux, Bordeaux, France. [26]University of Winnipeg, Winnipeg, MB, Canada. [27]California Institute of Technology, Pasadena, CA, USA. [28]Jet Propulsion Laboratory, California Institute of Technology, Pasadena, CA, USA. [29]University of Copenhagen, Copenhagen, Denmark. [30]McGill University, Montreal, QC, Canada. [31]Department of Earth Science and Engineering, Imperial College London, London, UK. [32]Institut de Mécanique des Fluides, Université de Toulouse 3 Paul Sabatier, Institut National Polytechnique de Toulouse, Toulouse, France. [33]Laboratoire Atmosphères, Milieux, Observations Spatiales, CNRS, Université Saint-Quentin-en-Yvelines, Université Paris Saclay, Sorbonne Université, Guyancourt, France. [34]Research Group ERICA, Universidad de Valladolid, Valladolid, Spain. [35]Agencia Estatal Consejo Superior de Investigaciones Cientificas, Madrid, Spain. [36]University of Maryland, College Park, MD, USA. [37]Department of Physics and Applied Physics, Kennedy College of Sciences, University of Massachusetts, Lowell, MA, USA. [38]Institut Supérieur de l'Aéronautique et de l'Espace (ISAE-SUPAERO), Université de Toulouse, Toulouse, France. [39]Deutsches Zentrum für Luft- und Raumfahrt (DLR), Institute of Optical Sensor Systems, Berlin, Germany. [40]Department of Earth and Planetary Science, University of California, Berkeley, CA, USA. [41]Blue Marble Space Institute of Science, Seattle, WA, USA.
*Corresponding author. Email: rwiens@purdue.edu
†Present address: Earth, Atmospheric, and Planetary Sciences, Purdue University, West Lafayette, IN, USA.
‡List of authors and their affiliations appear in Supplementary Text.

Downloaded from https://www.science.org on November 01, 2022

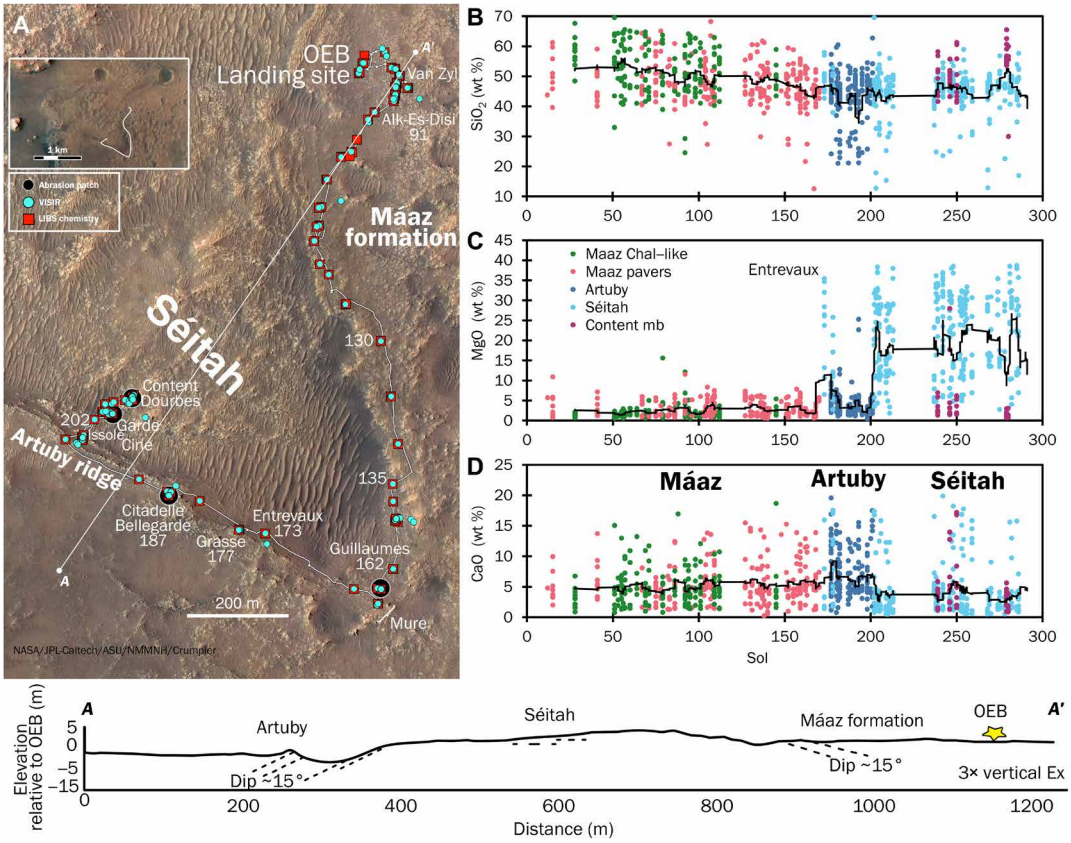

Fig. 1. Perseverance rover traverse and compositions over the first 286 sols of the mission. (**A**) Traverse is shown as a light gray line starting at the OEB landing site. Inset: Traverse location relative to a larger portion of Jezero crater floor. Locations of SuperCam VISIR spectral (blue circles) and LIBS chemistry observations (red squares) as well as abrasion patches (black circles) are indicated. Names of targets mentioned in this work and sol numbers are also indicated. The topographic profile follows the white line and has been extracted from the Mars Reconnaissance Orbiter High-Resolution Imaging Science Experiment (MRO/HiRISE) digital elevation model (DEM) sampled every 100 m. The dip angles are from (*25*). Vertical exaggeration ("Ex") is 3×. (**B** to **D**) Elemental abundances versus sol number for bedrock observations. Scatter in the data is due to the influence of individual mineral grains at or near the size of the laser beam (~350 μm; see Methods). The solid line is a 31-point running average, showing trends. Overhead images in (A) are from MRO/HiRISE. NASA/JPL-Caltech/ASU.

of the compositionally and morphologically distinct "Content member" (mb) (*24*, *26*).

Morphology and textures

The Máaz fm rocks near OEB are composed of pavers juxtaposed with Ch'al-like rocks (Fig. 2, A and B, and fig. S1, A to F) with no obvious layering. Contacts between the two morphologies are exposed in some locations, which show that pavers grade into darker, taller protrusions (fig. S1, A to D). Both morphologies were present along the early traverse although more Ch'al-like rocks were observed close to OEB and Van Zyl (Fig. 1A). To the east, these morphologies transition into a landscape dominated by massive, blocky outcrops that were not analyzed at close range (<20 m). Elongated, curved patterns were also observed from a distance (>20 m) that appeared to show viscous flow textures (*26*). A number of rocks observed locally along the traverse in the Máaz fm contain distinct pits (fig. S1, G and H).

RMI images from the Máaz fm show a rough texture (Fig. 2, A and B) characterized by coarse grains (0.5 to 3 mm) protruding from rock surfaces of both pavers and Ch'al-like rocks. Pavers frequently have a rough surface, in which 1- to 3-mm-wide grains with angular shapes protrude, suggesting euhedral crystals (arrows in Fig. 2B, inset). The surfaces of Ch'al-like rocks are smoother, with local color differences suggesting variable grain compositions or polymineralic grains (fig. S1, E and F). However, aeolian abrasion precludes identification of distinct grains across much of the observed Máaz fm.

The rover first reached clearly layered rocks at the "Mure" outcrop shortly after Sol 160, at the southern extremity of the rover traverse (Fig. 1A). Relatively indistinct subhorizontal fabric with one to several centimeter-thick layers is isolated to one small (meter size) outcrop. More layering was observed to the northwest below massive rocks comprising the top of Artuby ridge (Fig. 2C). These outcrops are variably recessive and typically exhibit a broken-up surface texture, suggesting relatively low resistance to mechanical erosion. Layers are generally indistinct and were not visible across the entire length of the outcrops, preventing identification of depositional beds or planar joints. At close range, rocks from Artuby ridge and Máaz terrain are both dominated by 1- to 2-mm-size grains, but Artuby rocks have more variability in grain size and have a strong imprint of the planar fabric/layering visible down to the millimeter scale that complicates a more definitive assessment of the texture (Fig. 2D).

Downloaded from https://www.science.org on November 01, 2022

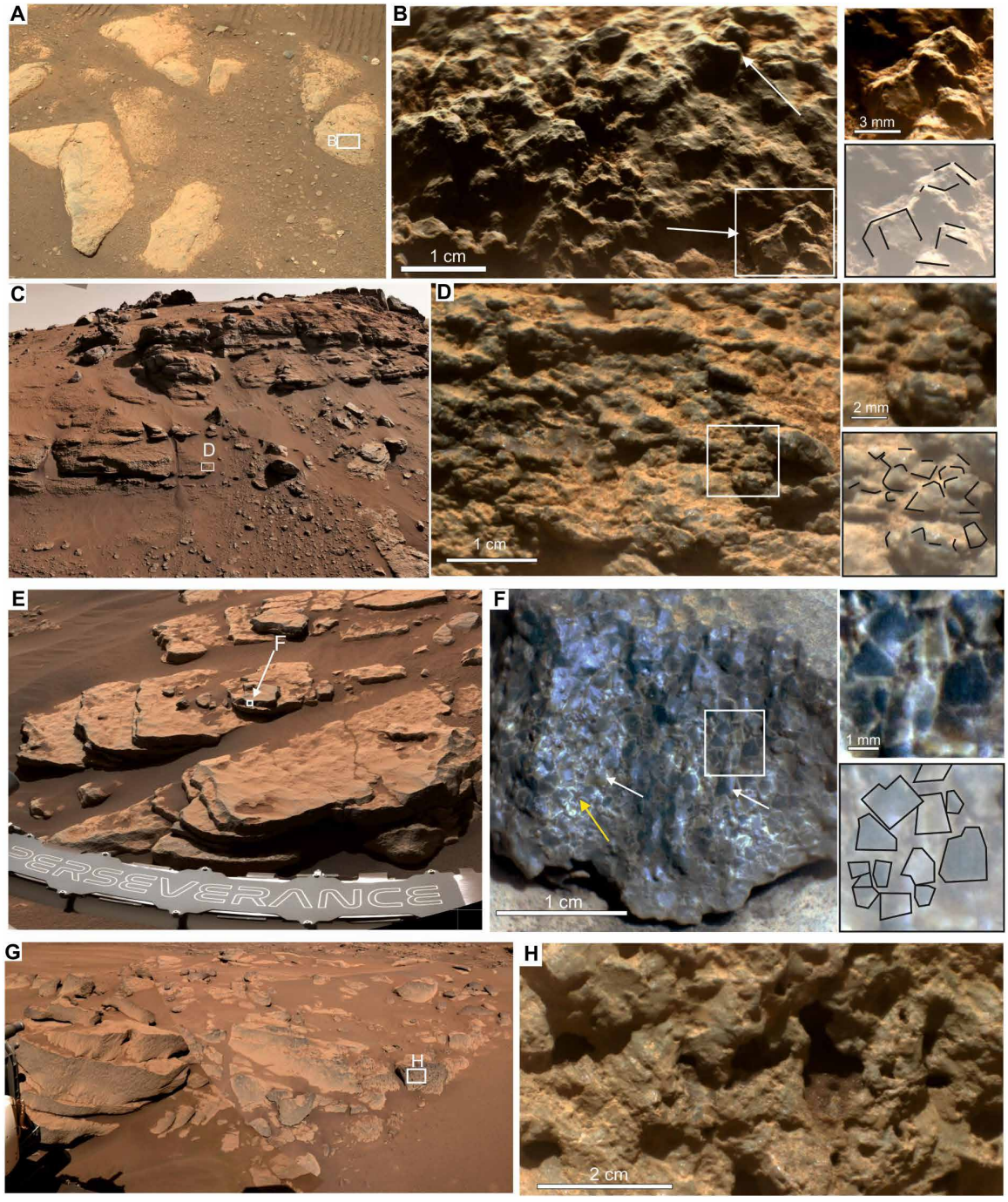

Fig. 2. Rock texture of the units observed during the traverse. Textures are shown at Mastcam-Z and Navcam scales (left side) and SuperCam RMI scales (right side); hand-drawn lines at far right indicate potential grain boundaries for several targets. (**A** and **B**) Target Peppermint (Sol 46), a Máaz fm paver near the OEB landing site. The tangential sunlight highlights grains with angular shapes (nearly cubic for one of them) reaching up to 3 mm in size (white arrows). (**C** and **D**) Rock texture at Artuby ridge, which displays a subhorizontal parallel-layer fabric with poor continuity from one layer to the other. The target Grasse (Sol 175) displays a granular texture with millimeter-size grains with planar arrangements of platy cumulus minerals. Grains appear subangular to subrounded. (**E** and **F**) Target Cine (Sol 204) at the Bastide outcrop in Séítah (fig. S2) showing centimeter-thick layers, using Gaussian color stretch for the RMI image. The clean ledges (E) have relatively fresh surfaces dominated by angular grains (1 to 2 mm) suggestive of euhedral crystals (F). White arrows indicate euhedral grain shapes; yellow arrows indicate interstitial fill with noneuhedral shapes. (**G** to **H**) Target Content (Sol 238), defining the Content mb within the Séítah fm, showing pitted rocks in continuity with layered outcrops. Image designations are described in text S10 and provided in table S6.

Downloaded from https://www.science.org on November 01, 2022

In contrast to the Máaz fm, rocks in the Séítah fm have well-developed layering at scales from a few centimeters to tens of centimeters (Fig. 2E), traceable more than tens of meters in some cases. Layers near the edge of Séítah dip in the same direction as layers in Artuby ridge (10°SSW); however, some layers farther into the interior of Séítah are flatter. Rocks in Séítah show a distinctive holocrystalline texture, most evident in broken rock faces (Fig. 2F). Table S1 shows grain size distributions observed in several locations in Séítah. Overall, the sizes cluster in a relatively tight distribution with a mean and SD of 1.45 ± 0.20 mm (text S2 and table S1). Grains are predominantly angular to very angular, suggesting euhedral shapes (Fig. 2F) with predominantly equant dimensions (defined as the ratio between the longest axis and the perpendicular short axis being >1:2). The space between grains is filled by relatively homogeneous material with irregular boundaries at the scale of the RMI. One exception to the granular nature of the Séítah fm is a group of pitted rocks observed to be in continuity (e.g., no clear boundary) with the layered rocks of Séítah, typified by a target named Content (Figs. 1A and 2, G and H). In addition to being pitted, their textures appear less crystalline.

Elemental compositions and inferred minerals present along the traverse

The overall trend of elemental compositions observed by SuperCam LIBS along the traverse is shown in Fig. 1 (B to D). The trend shows progressively decreasing mean SiO_2 abundances with increasing sol number, as seen by the solid line showing the running average in Fig. 1B with a strong increase in MgO in Séítah (Fig. 1D). Observations along the traverse up to Sol 173 indicate that the Ch'al-like rocks are the richest in SiO_2, with a Ch'al-like mean abundance of 52.6 ± 0.6 weight % (wt %) versus 47.5 ± 0.5 wt % for the pavers, where the uncertainties are the SEMs (table S2).

As the rover encountered Artuby ridge (sols 177 to 201), SiO_2 continued to decrease. Artuby ridge has a mean SiO_2 abundance of 43.5 ± 0.6 wt %, nearly 10 SDs of the mean below that of the Máaz fm (Table 1). Other differences are observed in Artuby compositions. In particular, more high-CaO points are seen in Artuby, leading to a higher mean CaO abundance (Table 1). Artuby also has distinctly higher TiO_2 abundances (Table 1 and fig. S3). Comparison of Fig. 3 (B to A) shows that Artuby compositions also differ from Máaz in Al/Si and (Mg + Fe)/Si. The statistical differences between Artuby and Máaz are described and illustrated further in text S3 and figs. S4 and S5.

The Séítah fm is characterized most strongly by a large increase in MgO (Fig. 1C). The first Séítah target, Entrevaux, was encountered on Sol 173 in the trough along the southwest edge of Séítah (Fig. 1A). MgO returned to its previously low values on Artuby ridge and rose again as soon as the rover descended into Séítah on Sol 201.

The differences in elemental compositions suggest variable mineralogies for the different localities and rock types as represented in Fig. 3, which shows the compositional ranges of Máaz and Séítah in Al/Si and (Mg + Fe)/Si. In this figure, felsic minerals plot along the y axis and mafic minerals plot along the x axis. Onboard standards representing igneous mineral compositions (andesine, diopside, enstatite, ferrosilite, and olivine) provide reference points for these observations. Máaz compositions at the scale of the laser beam (~350 μm) appear to be mostly mixtures between plagioclase and pyroxene. These mineralogies are also inferred directly from the elemental abundances.

Overall, we infer that Artuby ridge has a different mineral assemblage than the Máaz fm, and, based on the CaO and TiO_2 abundances, it contains more augite. Plagioclase abundances appear lower in Artuby compared to the Máaz fm. In particular, plagioclase grains matching the size of the laser beam were not observed in Artuby, as indicated in Fig. 3B by the lack of Artuby data points near the andesine standard. The statistical differences between Artuby and Máaz are described and illustrated further in text S3 and figs. S4 and S5. VISIR observations confirm the presence of high-calcium pyroxene in Artuby and Máaz; given that VISIR spectroscopy lacks the ability to identify plagioclase, pyroxene is the main observable primary mineral in these units (see Methods).

In contrast to Máaz and Artuby, Séítah is dominated by olivine, confirmed by all three SuperCam spectral techniques. LIBS observations cluster around the onboard olivine standard in Fig. 3B, with trends toward the onboard orthopyroxene (enstatite and ferrosilite) and augite (diopside) standards. SuperCam's VISIR spectra detect olivine by a broad absorption near 1 μm (Fig. 4B) with strong downturns in both SuperCam's visible (up to 0.85 μm) and IR (down to 1.3 μm) spectral ranges (Fig. 4A). The IR spectral slope between 1.3 and 1.8 μm (fig. S6) provides a good indicator of the olivine signal strength and mimics the MgO trends (Fig. 1C). Olivine is also

Table 1. Major element compositions of major units and the abrasion patches where proximity instruments were used. Numbers in parentheses are SEM. *N* is the number of observation points. Abrasion patches are described in text S9.

Mean wt %	SiO_2	TiO_2	Al_2O_3	FeO_T	MgO	CaO	Na_2O	K_2O	Total	*N*
Máaz (sols <177)	49.6(0.4)	0.57(0.02)	9.4(0.2)	18.4(0.6)	2.7(0.1)	5.1(0.1)	2.9(0.1)	1.07(0.05)	89.8	438
Artuby (sols 177–201)	43.5(0.6)	0.90(0.04)	6.9(0.2)	22.2(0.8)	3.9(0.2)	7.0(0.3)	2.4(0.1)	0.53(0.04)	87.4	179
Séítah (sols 202–286)	45.1(0.4)	0.24(0.02)	4.1(0.2)	23.0(0.4)	21.4(0.5)	3.8(0.2)	1.3(0.1)	0.21(0.02)	99.8	344
Content mb (sols 239–279)	51.8(1.0)	0.49(0.08)	12.1(0.9)	15.9(2.2)	3.2(0.7)	4.5(0.5)	4.0(0.2)	1.39(0.15)	93.3	47
Abrasion patches										
Guillaumes (Máaz)	44.4(1.7)	0.42(0.11)	8.1(1.1)	22.7(3.0)	2.0(0.2)	6.5(0.8)	2.7(0.3)	0.56(0.15)	87.5	23
Bellegarde (Artuby)	44.6(1.4)	0.92(0.07)	7.0(0.5)	25.9(2.1)	2.0(0.1)	5.7(0.5)	2.6(0.2)	0.69(0.11)	89.4	31
Garde (Séítah)	42.0(1.9)	0.12(0.07)	4.2(0.5)	21.9(1.1)	17.5(1.6)	3.1(0.8)	0.9(0.2)	0.13(0.06)	89.9	22
Dourbes (Séítah)	41.4(1.9)	0.10(0.03)	2.8(0.2)	25.6(1.9)	21.0(1.7)	5.1(1.2)	0.7(0.1)	0.01(0.01)	96.6	23

Downloaded from https://www.science.org on November 01, 2022

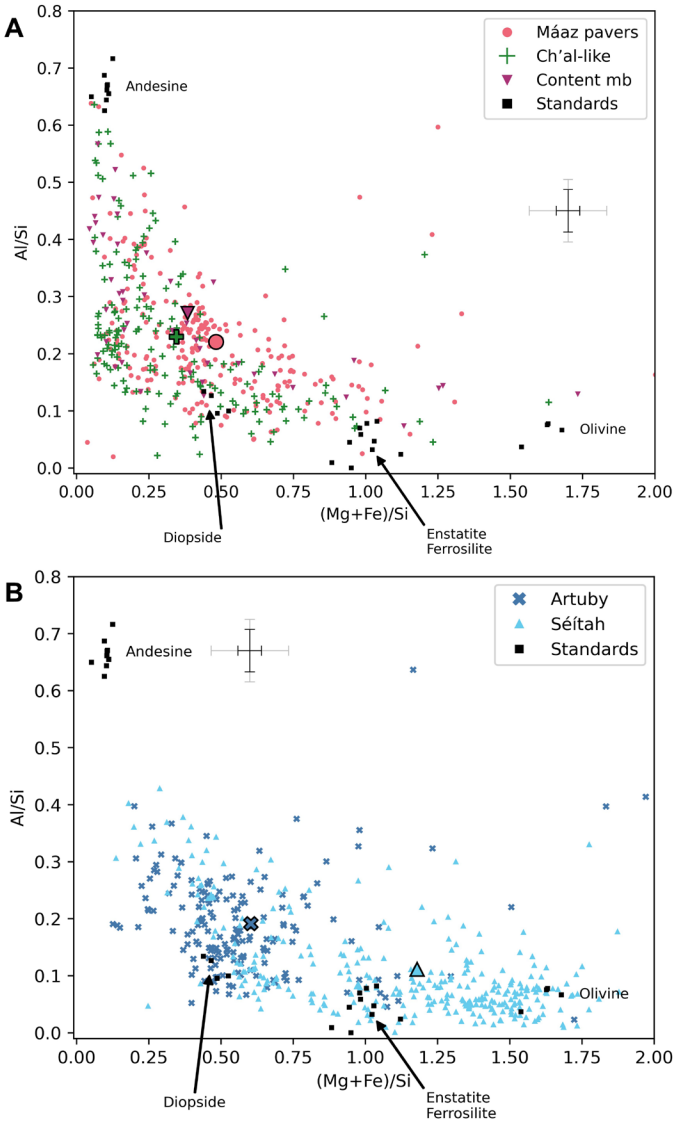

Fig. 3. Molar ratios showing contrasting compositions sampled by SuperCam's 350-μm laser beam. (**A**) Plagioclase- and silica-rich compositions observed in the Máaz fm pavers and Ch'al-like rocks and later in the Content mb of the Séítah fm. In (A), the points consist of mixtures of plagioclase, represented by the onboard andesine target (black squares in top left) with pyroxene, represented by the diopside (high-calcium pyroxene), and enstatite and ferrosilite (low-calcium pyroxene) targets. A few iron oxide points scatter up and to the right of the main group. (**B**) Observations from Artuby ridge, which clusters around the diopside standard (but are the Fe-rich variety of augite), with trends toward ferrosilite and andesine, although there is a clear lack of points near the andesine standard. Also shown in (B) are the Séítah observations, most of which trend between the olivine and pyroxene standards, with a small amount of scatter partway in the direction of plagioclase. Both panels show the mean compositions of each unit in larger symbols. SEMs are shown in fig. S7. The mean single-observation precision and accuracy are represented on each panel as superposed dark and light crosses, respectively.

confirmed by Raman spectra exhibiting the characteristic doublet peaks around 820 and 850 cm^{-1}. A small number of Séítah points trend upward and to the left in Fig. 3B, indicating the presence of plagioclase at a low abundance in this unit. Last, the Content mb differs from the main body of Séítah in that it lacks olivine (not observed by any of the three SuperCam spectral techniques) and is compositionally similar to Máaz. In particular, it shows relatively high Al/Si, similar to Máaz (Fig. 3A) and unlike Artuby or Séítah (Fig. 3B).

In terms of mineral stoichiometry derived from LIBS, Máaz and Séítah fms show considerable differences, including in their inferred pyroxene compositions (Fig. 5A). The Máaz fm actually contains both augite ($Wo_{43-48}En_{25-30}Fs_{22-31}$) and Fe-rich orthopyroxene/pigeonite grains ($Wo_{3-15}En_{4-11}Fs_{74-93}$). By contrast, in Séítah, both the augites and the low-Ca pyroxene are much more Mg-rich, showing a trend from low-Ca pyroxene ($Wo_{3-10}En_{44-50}Fs_{40-51}$) to augite ($Wo_{32-38}En_{38-44}Fs_{18-27}$). Olivine compositions in Séítah range from Fo_{54} to Fo_{72} (Fig. 5A).

The overall results show at least four compositionally distinct units: Máaz fm, Artuby ridge, Séítah fm, and Content mb, for which we present the mean abundances in Table 1. Here, we combine pavers and Ch'al-like into a single Máaz fm entry due to their colocation and contiguous nature. On the other hand, the Content mb, while located within Séítah, is kept separate because of its very significant difference in composition relative to the surrounding Séítah rocks. We will use the four sets of mean abundances in Table 1 as the basis for discussion and comparison.

Aqueous alteration and deposition: VISIR observations and constraints from chemistry

Nearly all of SuperCam's VISIR reflectance spectra indicate some degree of hydration. We evaluate these data to understand the secondary phases and the extent of aqueous alteration. While a few (<10) fine-grained Máaz fm targets show almost featureless VISIR spectra (Fig. 4A, gray spectrum), most targets indicate some degree of hydration, most commonly seen as a ~1.9-μm absorption feature exceeding a 0.02–band depth threshold on 92% of observation points, and extending up to 0.2 band depth. The depth of this hydration band is greater than that observed in spectra from the Mars Reconnaissance Orbiter's Compact Reconnaissance Imaging Spectrometer for Mars (CRISM) (0.05 to 0.1). The Máaz rocks also commonly show a 2.28-μm absorption feature in SuperCam spectra, with a downturn above 2.3 μm due to a 2.4-μm absorption (Fig. 4A, dark mean spectra of Máaz fm rocks). The 2.28-μm absorption band is frequently paired with absorptions at 1.42, 1.92, and 2.4 μm, indicating that Fe(III)-rich phyllosilicates such as nontronite or hisingerite are relatively abundant (20% of points surpass a 0.02–band depth threshold for the 2.28-μm feature, and 40% surpass 0.01). While these absorptions are frequently present, their features are weak—the majority of the 2.28-μm band depths does not exceed 0.02 to 0.03—suggesting a limited proportion of Fe-phyllosilicates and/or the presence of (an) additional hydrous phase(s) in the Máaz fm rocks.

We identified possible monohydrated Mg sulfates in the abraded surfaces of the Máaz fm by a combination of 1.92- and 2.14-μm absorptions and a downturn of >2.3 μm (Fig. 4, A and B, yellow spectra). These measurements from the cleanest surfaces, exposed by the rover's abrasion tool, may explain the widely observed shallow downturn past 2.3 μm in the Máaz fm rocks, although this feature is not unique to sulfates and might be attributed to any poorly crystalline mineral with water, including oxyhydroxides and sulfates. VISIR observations also show the presence of an absorption near 2.2 μm, either indicative of Al-OH species, hydrated silica, or gypsum (Fig. 4A, orange spectrum). In addition to VISIR spectra,

Downloaded from https://www.science.org on November 01, 2022

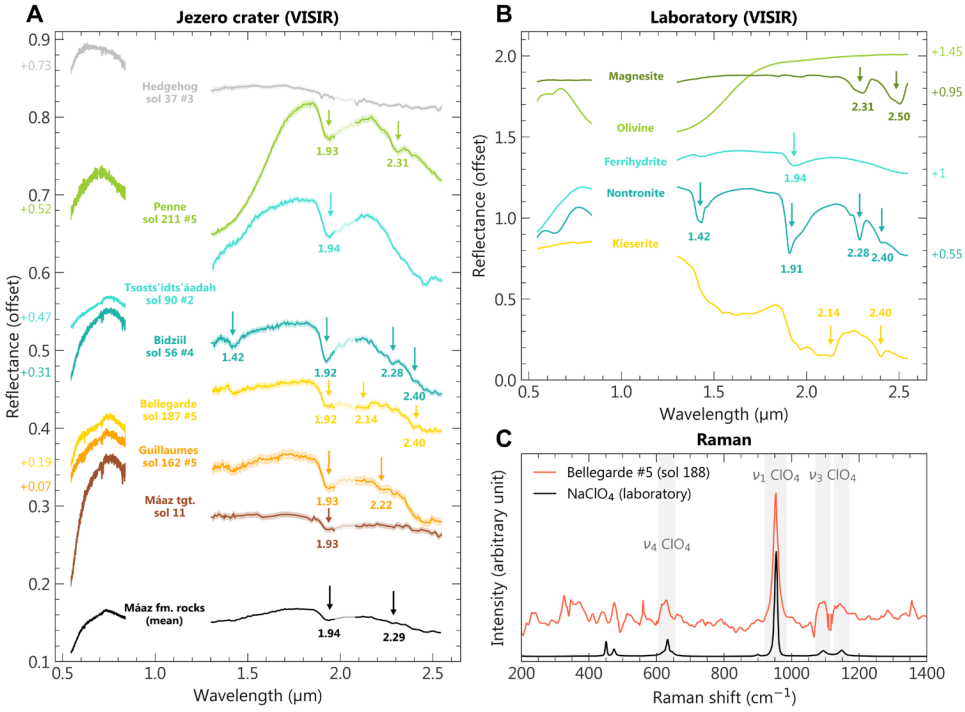

Fig. 4. Representative spectra showing the diversity of VISIR and Raman spectral features. (**A**) VISIR reflectance spectra observed in the Séítah ("Penne," second from top) and Máaz fms (all other plots). (**B**) Laboratory spectra of pure minerals (see text S7). Spectra are offset for clarity. A few targets have nearly featureless spectra [e.g., "Hedgehog" in (A)], but the mean signature of the Máaz fm [(A), bottom] is consistent with the presence of hydrated surfaces. The spectral features best exemplified in targets "Tsosts'idts'áadah," "Bidziil," Bellegarde, and Guillaumes are potentially explained by contributions of oxyhydroxide, Fe-phyllosilicate, monohydrated sulfate or perchlorate, and gypsum or an Al-OH or Si-OH phase, respectively (see the text S7 for band attribution). The "Máaz tgt." spectrum is from the namesake of the fm and is typical of targets with strong dust coatings. The Penne spectrum was collected in Séítah and is consistent with the presence of olivine and traces of a Mg-OH phase and/or a carbonate (e.g., magnesite). (**C**) Raman spectrum of sodium perchlorate observed on one point in the Bellegarde abrasion patch, compared with a laboratory spectrum of sodium perchlorate (*69*).

a Raman spectrum from the Bellegarde abrasion patch (Fig. 4C) indicated the presence of sodium perchlorate.

The VISIR spectra of Séítah rocks also contain alteration-related absorption bands in the form of a wide band centered at 2.31 μm accompanied by a 1.93-μm band (Fig. 4A, green spectrum). A complex mixture of Mg-rich phyllosilicate and/or Fe-Mg carbonates can explain these signatures. A few LIBS observations in Séítah have low SiO_2 (Fig. 1B) and increased C emission-line peak areas, indicating carbonates. Carbonate was also detected in a Raman spectrum of the Garde abrasion patch (Sol 209). Overall, Fe-Mg carbonates comprise a very small fraction (likely <5%) of the composition of Séítah based on the fraction of occurrences and extent of influence in LIBS observations.

While VISIR observations identify the alteration species, we look to a combination of chemistry and VISIR spectra to understand the magnitude and style of alteration. Figure 6 shows the chemistry relevant for characterizing aqueous alteration in a plot of molar Al_2O_3 versus ($CaO + Na_2O + K_2O$) and ($FeO_T + MgO$). We do not detect enrichment of Al_2O_3 relative to the more water-soluble cations, Ca, Na, and K. Such an enrichment, the direction of which is indicated by arrows in Fig. 6, would result in compositions plotting well above the line between plagioclase and the FeO + MgO apex (*27*). Their absence indicates limited removal of soluble cations. The relatively low abundances of some cations also constrain the amounts of secondary materials added by precipitation. For example, MgO ≤ 2.0 wt % in the Ch'al-like rocks and in abrasion patches Guillaumes and Bellegarde (Table 1 and table S2) limits Mg-dominated sulfates and carbonates in these locations to at most only several percent on average. As discussed below, the extent of bulk chemical weathering and addition of precipitated salts are limited by the overall chemistry and the fact that we observe the primary igneous mineral signatures such as olivine in VISIR spectra in Séítah (Fig. 4, A and B, green spectrum). Isochemical weathering still played a role in producing some in-place alteration. In particular, IR spectra suggest that rocks include some Fe(III) phyllosilicates.

Modal mineral abundances estimated from elemental compositions

The relatively limited extent of alteration allows us to study the igneous compositions of the rocks observed along the traverse. However, some alteration materials were part of the LIBS observations. Máaz fm and Artuby ridge observations included points with low SiO_2 (e.g., <35 wt %; Fig. 1B) and low totals of the eight major elements (see Methods and data file S1), signaling the occasional presence of up to >20 wt % of other elements such as S, C, H, and Cl that are not currently quantified. After excluding these LIBS observation points (text S4), using the remaining dataset, we estimated the mean igneous compositions, CIPW normative mineral compositions, An (plagioclase) and Mg numbers, and corresponding rock densities of Máaz, Artuby, and Séítah, presented in Table 2. We

Downloaded from https://www.science.org on November 01, 2022

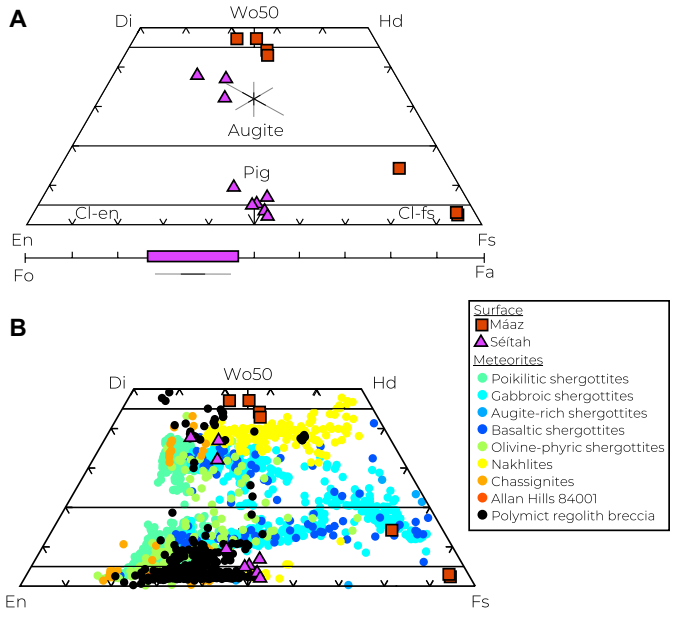

Fig. 5. Pyroxene quadrilateral. (**A**) Pyroxene compositions observed in Máaz fm (red squares) and Séítah (purple triangles). The range of Mg numbers of Séítah olivines is shown below (see fig. S8). Superposed error bars show mean precision (dark lines) and accuracy (light lines). (**B**) Comparison with pyroxene composition found in martian meteorites. The Máaz fm contains augite and Fe-rich pyroxenes, similar to basaltic shergottite meteorites, whereas the Séítah fm contains pyroxenes more enriched in Mg, similar to poikilitic and olivine-phyric shergottites. End members and compositions are indicated as follows: Di, diopside; Hd, hedenbergite; Wo50, wollastonite 50%; Pig, pigeonite; Cl-en, clinopyroxene enstatite; Cl-fs, clinopyroxene ferrosilite; En, enstatite; Fs, ferrosilite; Fo, forsterite; Fa, fayalite. Meteorite data in (B) are from references given in reference file S1.

Table 2. CIPW norms and calculated parameters derived from normalized abundances of the main observed units. Elemental abundance totals are normalized to 100 wt % as described in Methods and assume Fe^{2+}/total Fe = 0.95. Error on density is propagated from SEMs for compositions (see Methods).

Weight %	Máaz	Artuby	Séítah
SiO_2	54.2	49.7	44.8
TiO_2	0.6	0.9	0.2
Al_2O_3	10.5	7.4	3.9
FeO_T	20.2	25.3	22.6
MgO	2.7	3.8	21.4
CaO	5.5	7.7	3.6
Na_2O	3.3	2.7	1.3
K_2O	1.2	0.6	0.2
Quartz	5.6	0.0	0.0
Plagioclase	37.9	30.0	15.2
Orthoclase	7.1	3.6	1.2
Diopside	4.8	16.7	1.5
Hypersthene	37.9	41.5	34.7
Olivine	0.0	0.9	41.1
Ilmenite	1.1	1.7	0.4
Magnetite	1.6	2.0	1.8
An # plagioclase	25.3	22.7	26.5
Mg #	19.3	21.1	62.8
Density (g/cm^3)	3.10	3.27	3.37
	±0.02	±0.03	±0.01

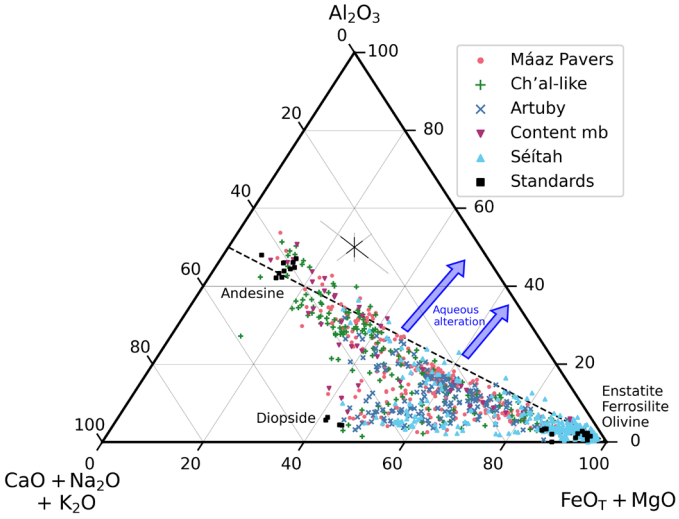

Fig. 6. Elemental compositions indicating the relative absence of chemical weathering by aqueous leaching of soluble elements. Trends in the direction of the blue arrows, above the dashed line from the iron-magnesium corner to the ideal plagioclase composition on the left, would indicate leaching of mobile elements represented at the base of the triangle. Observations of onboard standards (*63*) are plotted along with the compositions of observed points. Dark error bars indicate precision; light error bars indicate mean accuracy (*62*).

ignore the Content mb here due to its relatively few observations. Relative to the less mafic Máaz, the Artuby normative mineral abundances decrease in amounts of silica (as quartz in the norm calculation), plagioclase, and orthoclase while increasing in diopside (to 17 wt %), hypersthene (to 42 wt %), and the metal oxides ilmenite and magnetite. For these four minerals, Artuby has the highest normative abundances among the three units, resulting in a significantly higher inferred density than Máaz. CIPW norm calculations of Séítah's mean igneous composition yield normative 41% olivine, while normative plagioclase drops to 15 wt %. Observations show similar results across three different regions of Séítah (fig. S2). This composition is strongly mafic although not technically ultramafic (defined as ≤10 wt % plagioclase). The Mg# [Mg/(Mg + Fe) molar ratio] of the bulk Séítah is 63 (Table 2). Comparison to the onboard olivine standard suggests that our calibration gives a slight overestimate of SiO_2 and underestimate of FeO_T, implying that Séítah could contain more than the 41% normative olivine given in Table 2, characterized by a slightly lower Mg number (cf. 28; text S4).

On Mars, the presence of igneous minerals does not necessarily imply an igneous deposit, given the low degree of alteration that is typically observed. For example, much of the Murray fm of Gale crater, which is a lacustrine deposit, consists of mostly igneous minerals (*28*). On that basis, careful consideration must be given to the depositional nature of the fms regardless of the presence of igneous minerals. Although Perseverance landed in a lacustrine basin

Downloaded from https://www.science.org on November 01, 2022

in Jezero crater, we present arguments in the next section in favor of an igneous deposition for all of the units traversed during these sols.

DISCUSSION

Igneous characteristics

A number of features suggest that the rocks observed along the traverse are igneous. We start with Séítah's defining features, in particular the abundant, euhedral, large (~1.5 mm), monocrystalline-appearing olivine grains (Fig. 2, E and F). Fine-scale observations in Séítah by the Planetary Instrument for X-ray Lithochemistry (PIXL) instrument show that olivine and pyroxene are intergrown in a pattern that clearly demonstrates they are cogenetic (*29*). The prevalence of olivine is consistent with a density-driven cumulate rather than classical coarse-grained igneous rocks that contain various crystals of similar sizes such as pyroxene, olivine, and plagioclase in a basalt. The observed olivine crystals do not show evidence of intergrowth with each other, but rather are closely packed with abundant face-to-face contacts (Fig. 2F) (*29*), suggesting settling as a mechanism for concentrating olivine. Settling by gravity within a melt is also consistent with the narrow grain size distribution observed in most of the SuperCam RMI images of Séítah (table S1). The mean composition of Séítah yields a Mg number (Table 2) in the same range as the individual olivine grains (Fig. 5A). This is generally consistent with CRISM orbital estimates of the unit inside and outside Jezero as $Fo_{44–65}$ (*30*). Given the Fe-Mg partitioning between olivine and basaltic melt [$K_D{}^{Fe\text{-}Mg}{}_{ol\text{-}melt} \sim 0.35$; (*31*) and references therein], the olivine grains are out of equilibrium with the bulk material, consistent with their concentration by density settling at the base of the melt. On Earth, most ultramafic rocks are intrusive cumulates and mantle peridotite but can be a product of eruptions, more common in the Archean eon [e.g., (*32*, *30*) and references therein]. Although layering is well known to occur in terrestrial lavas and intrusive bodies [cf., (*33*)], within Séítah, we do not observe either changes in mineralogy, chemistry, or grain size from one layer to the other, suggesting that layers may reflect reorganization of grains during cumulate packing (*34*). Séítah differs from terrestrial analogs in that its thin layers (Fig. 2E) occur without accompanying changes in chemistry, and we find this difference to be the biggest challenge to the cumulate hypothesis.

The layering of Séítah could be construed as an argument for a sedimentary instead of igneous origin. However, the internal structures of these layers do not readily fit those usually expected for sedimentary structures. Séítah layers, for instance, do not contain internal laminations (e.g., planar or cross-lamination) indicative of traction-deposited sediments (*35*, *36*). Although deposition from heavily laden turbidity currents or fallout associated with hypopycnal flows (*37*) can produce planar beds lacking sedimentary laminae, such deposits often display systematic changes in grain size associated with settling (*38*, *39*) that are not observed in Séítah. Observed grains within Séítah are predominantly angular and monomineralic (Fig. 2F), consisting of olivine and, more sparsely, pyroxene and plagioclase within interstitial spaces (*29*). Although the mean grain size and narrow range of sizes of Séítah are consistent with dynamic sorting typical of sedimentary deposits, grains do not show any indication of preferential sorting within individual layers (e.g., graded bedding) that might be attributed to either waning flow or fallout, with no obvious rounding of grains. We did not observe any systematic differences in grain size or the presence of fines between successive centimeter-scale layers (Fig. 2E) that could be attributed to fluctuations in the energy of successive depositional events [e.g., (*38*, *39*)].

Alternatively, regional olivine-bearing units observed from orbit have been hypothesized as tephra deposits (*40*, *41*). In contrast to pyroclastic deposits, Séítah rocks are predominantly crystalline, not glassy, based on spectra and imaging, and do not contain distinct clasts of pyroclastic origin, lapilli, indications of grain sorting, or extensive evidence for hydrolytic alteration (*42*), and so our observations do not favor a pyroclastic origin for Séítah. In summary, we find that Séítah is the first igneous cumulate body observed on another planet.

The Máaz fm, including Artuby ridge, also displays characteristics consistent with an igneous origin. Its textures contain 0.5- to 3-mm grains (e.g., Fig. 2, B and D) with local angular textures typical of euhedral shapes in the whole area. Local viscous-flow patterns similar to pahoehoe lavas could favor a lava flow origin, but the crystalline, phaneritic texture is distinct from classical aphanitic texture of lava flows and suggests a prolonged crystallization period for at least parts of Máaz. Similar to Séítah, there is a lack of features expected in a sedimentary unit, such as laminations, visible clasts, and cross-stratifications. The observed fabric at Mure and Artuby ridge could be related to either cumulate layers as in Séítah, which starts immediately below, or planar joints (*33*). Recessive layers in Mure and Artuby could represent poorly crystalline igneous material. This material was never successfully targeted by SuperCam.

Density stratification and scenarios for emplacement

The data from the entire traverse reveal a notable progression of increasingly mafic material and increasing inferred density from Máaz to Artuby to Séítah. This is best seen in Fig. 7B, which shows the compositions of SiO_2, Al_2O_3, and alkali elements all trending progressively downward across these three units. These decreases are accompanied by concomitant increases in mafic elements MgO and FeO_T (Table 2). Calcium oxide shows a peak at Artuby, which could be expected because of its higher abundance of augite as an intermediate density material. Figure 7B and Table 2 are ordered according to the inferred original stratigraphic position, illustrated in Fig. 7A and derived from the surface observations and RIMFAX subsurface observations [Fig. 1A and (*25*)]. The current observations allow for Artuby ridge to be stratigraphically below the portion of the Máaz fm traversed on the east side of Séítah and subsequently uplifted. In this scenario, SuperCam observations show a progression of compositions and derived density through three vertical regions of igneous material (Máaz, Artuby ridge, and Séítah).

The relationship between the three units poses several possibilities for their emplacement: (i) The units are part of one continuous igneous body, such as a thick cumulate, or (ii) they represent separate, increasingly evolved magmas (with or without genetic association). In both cases, Séítah is interpreted as a cumulate. In the first case, it is overlain by a more pyroxene-rich layer (Artuby), with lower-density material of the same igneous body above it (Máaz), as shown in Fig. 8A. Artuby ridge is enriched in normative pyroxene to 58% on average (Table 2) with higher abundances in some targets (data file S1). Artuby lacks the well-organized coarse grains that characterize Séítah (Fig. 2F); however, pyroxene zones in terrestrial cumulate bodies can also be characterized by finer grains. On Earth, not all cumulates may have pyroxene cumulate zones, and some concentrate clinopyroxene and orthopyroxene variably, depending

Downloaded from https://www.science.org on November 01, 2022

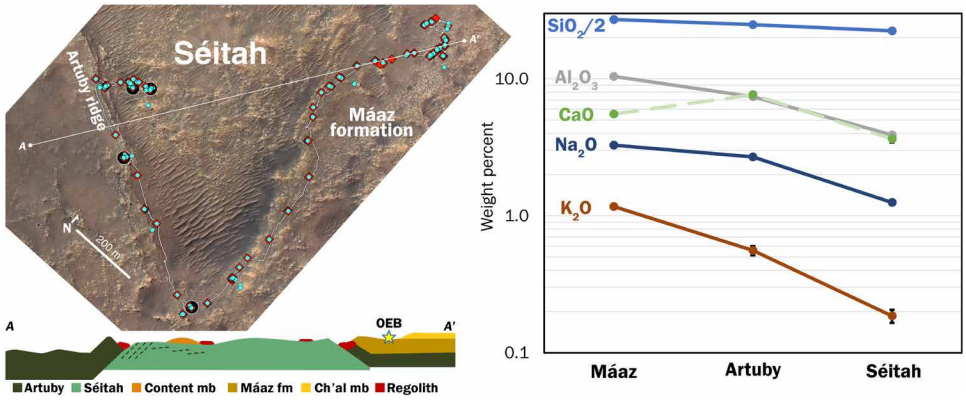

Fig. 7. Stratigraphic concept and mean elemental composition trends. (**A**) Conceptual view of the current stratigraphic positions of Máaz, Artuby, and Séitah. The outcropping portion of Artuby and the SW portion of Séitah adjacent to it show dipping strata in exposure and in RIMFAX radargrams. Artuby was not seen to be exposed on the NE side of Séitah. RIMFAX data indicated dipping strata on that side of Séitah too. Máaz is inferred to be overlying both Artuby and Séitah. All units were emplaced after the fm of Jezero crater and well above the base of the crater. (**B**) Elemental trends progressing from Máaz to Artuby to Séitah. This plot shows, on a logarithmic scale, a systematic decrease in felsic elements (SiO_2, Al_2O_3, Na_2O, and K_2O) with decreasing proposed original stratigraphic elevation. CaO (dashed line), which occurs in both plagioclase and orthopyroxene, is highest at Artuby due to its enrichment in augite. Error bars indicate SEMs where large enough to be seen, for comparison between points (see Methods).

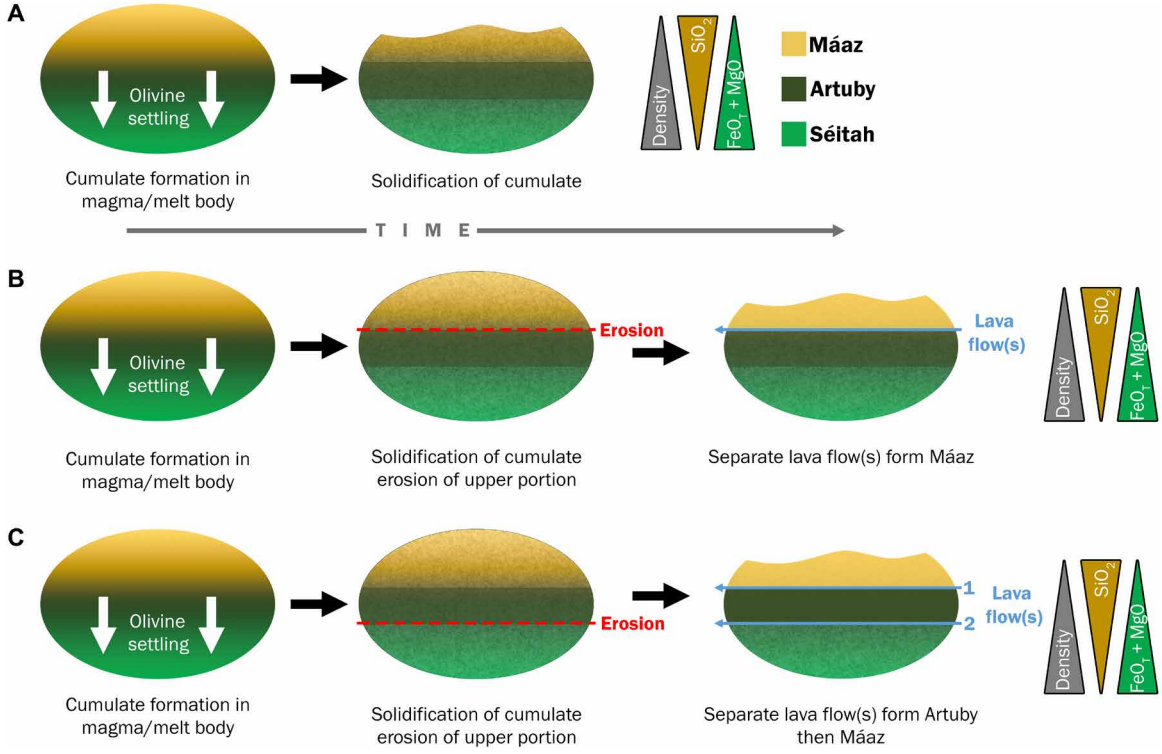

Fig. 8. Formation scenarios. (**A**) Cumulate formed from stratification of a single melt in which olivine phenocrysts were segregated by gravity in a magma body, which subsequently solidified. All of the rocks observed by SuperCam were produced within this igneous body in this scenario. (**B**) Cumulate plus lava flow(s) scenario, initiated with the fm of Séitah and Artuby as a cumulate as in (A). The depleted upper portions of the body were removed and subsequent lava flow(s) produced Máaz. (**C**) Third scenario in which Artuby was also produced by a relatively viscous lava flow before emplacement of Máaz by later and more evolved lava. Triangles at the right indicate overall composition and density trends.

on the physical conditions including convection, size of the melt region, cooling rates, duration, and chemistry [e.g., (*43*)]. Several other features of the Máaz and Séitah fm rocks appear to fit the cumulate model, including the lack of observed contacts between the different units.

In the second scenario, Séitah is an olivine cumulate, but the upper portions of that body were removed over time at the surface. Subsequently, successive surface or near-surface igneous activity emplaced material stratigraphically above Séitah. In one version of this scenario (Fig. 8B), Artuby is the pyroxene-enriched portion of

Downloaded from https://www.science.org on November 01, 2022

the same igneous body as Séítah, with Máaz emplaced later as a more evolved extrusive igneous unit. A third possibility, shown in Fig. 8C, is that Artuby was also emplaced as a lava flow, somewhat more mafic than Máaz and not originating from the same magmatic body. However, the pyroxene compositions show no distinction between Artuby ridge and the rest of the Máaz fm (Fig. 5A), suggesting a petrogenetic link between the two.

One exception to the olivine-rich nature of Séítah is the Content mb. Its existence and physical continuity with the rest of the Séítah rocks (Fig. 2G) call into question the cumulate scenario of Fig. 8A because of the abrupt change in composition. However, cumulates are known to have heterogeneous layering in different locations, attributed to injection of fresh material or entrainment of lighter material with denser, sinking material [e.g., (*30*)]. A second possibility is that the Content mb is a section of more differentiated Séítah cumulate that fell down the sequence during compaction. A third possibility is that the Content mb rocks are from a later-stage unconformable lava flow that was emplaced after Séítah was exhumed (Fig. 8, B or C). This may be more consistent with the pitted texture of the Content mb (Fig. 2H), which may be difficult to reconcile with a cumulate origin.

Current data do not enable a clear distinction among these scenarios, including the possibility of multiple lava flows from the same magma chamber producing progressively more evolved compositions over time. However, a potential weakness of this scenario is the lack of regional topography that would drive flows of relatively viscous material into this region. Melt sheets from a large, unidentified impact not far away (<150 km) might also produce these igneous features along with others outside of Jezero (see below). In the end, the first samples collected by the Perseverance rover may hold the clues needed to solve this question upon their return to Earth.

Comparisons to Mars meteorites

The mineralogical and chemical compositions of primary minerals in the Máaz and Séítah fms can be directly compared with the current suite of martian meteorites, which are igneous samples of other locations on Mars. Similarities shared by Jezero observations and Mars meteorites may suggest that these features are common on Mars, and their comparisons will aid in understanding Mars's igneous activity, chemical and mineralogical diversity, and thermal evolution.

The augite composition of Máaz (Fig. 5, A and B) is close to the compositions of the nakhlite pyroxene cores and Fe-rich rims as well as a few shergottites (*44*–*46*). The Máaz ferrosilite and pigeonite compositions are similar to those found in pyroxenes in basaltic shergottite Los Angeles and gabbroic shergottite Northwest Africa (NWA) 7320 (*47*), showing a similar evolution trend from calcic to ferric compositions, although Máaz pyroxenes are more Fe-rich than the corresponding meteorites. In general, pyroxenes in the Máaz and Séítah fms are lower in MgO and higher in FeO_T than most Mars meteorites (Fig. 5). The very high Fe compositions in Máaz pyroxenes likely indicate the presence of pyroxferroite, a metastable pyroxene formed at subsolidus, as also seen in Los Angeles and NWA 7320 (*47*, *48*). The pyroxene compositions observed in Séítah are similar to those in olivine-phyric shergottites and to the NWA 7034 polymict breccia pyroxenes (*49*, *50*). Olivine compositions in Séítah overlap those observed in olivine-phyric and poikilitic shergottites (*50*, *51*).

The Máaz and Content mb rocks are similar in bulk major element compositions to the basaltic shergottites, which contain pyroxene and plagioclase, although Máaz is enriched in SiO_2 compared to most martian meteorites. The basaltic shergottites represent flows, some of which have undergone fractionation of olivine and/or pyroxene. The Séítah fm bulk major element compositions fall within the compositions of poikilitic shergottites, also sharing a similar mineralogy. Last, the compositional relationships that we observed at Jezero crater appear to confirm the occurrence of density-driven fractionation on Mars that has been noted in martian meteorites [e.g., (*46*, *50*)]. This fractionation could occur early in Mars history in both melt sheets produced by large impacts and in magmatic processes, while the Mars meteorites are generally Amazonian and their fractionation is most likely from magmatic processes.

Martian meteorites preserve a long record of limited aqueous alteration in the form of carbonates, amorphous phases, and silicate minerals [e.g., (*52*)]. In the nakhlites, these carbonates are often associated with olivines and consist mainly of Fe carbonates with varying amounts of Mg, Ca, and Mn carbonate phases (*53*). Similar to carbonates in Séítah (*27*), carbonates in the martian meteorites appear to originate from aqueous alteration of olivines, suggesting that the source region of the carbonate-bearing martian meteorites experienced similar alteration processes to Séítah. Observation of organic materials associated with carbonates in ALH 84001 [e.g., (*54*)] suggests that organic-molecule production was likely active in association with carbonates in Jezero crater too.

Regional implications

The chemical and mineralogical information gained by in situ exploration and subsequent sample return of rocks on Jezero crater's floor may place valuable constraints on the origin of olivine-bearing rocks revealed by orbital and telescopic detection of olivine [e.g., (*50*, *51*, *53*)]. While the extent of olivine-rich rocks on Mars' surface appears limited, our study sheds light on Mars' largest olivine-bearing region, Nili Fossae. The nature of this peculiar, widespread regional unit is strongly debated: Studies have suggested various emplacement processes including volcanic flows, tephra deposits, impact melts, or sedimentary deposits (*40*, *41*, *55*–*58*). Our study provides an alternative scenario in which cumulates (formed intrusively or on the surface by thick lava flows or impact melts) explain the olivine enrichment.

However, the cumulate model does not easily extrapolate to the entire regional unit. In particular, a cumulate process cannot explain an olivine-rich unit with a draping geometry observed regionally and on Jezero crater's rim (*40*, *41*), since cumulates form by gravity either intrusively or by thick melt ponds on flat surfaces. Hence, it seems that olivine-rich materials may have been emplaced by a variety of processes, as may be expected for volcanism of highly mafic compositions [e.g., (*59*)]. The question of correlation between traverse observations and regional orbital observations is especially relevant for locations where a cap rock (<10 m in thickness) similar to Máaz capping Séítah exists over the olivine-bearing unit (*7*, *41*, *60*). In a scenario in which the whole crater floor is a cumulate, such cap rocks may correspond to the less mafic complement just as Máaz overlies Séítah. Future rover observations on the olivine-bearing unit on the rim or outside Jezero crater, especially if connected to a cap rock, will help to connect these findings within Jezero crater to the broader regional unit. Detailed investigation of other olivine-bearing regions on Mars could identify similar stratigraphic sections.

Downloaded from https://www.science.org on November 01, 2022

Our observations also highlight the role of aqueous alteration at a regional scale. Carbonates observed within Séítah provide a link to carbonates found regionally within the olivine-bearing unit (*4*, *7*, *8*, *10*, *41*), suggesting that the process of aqueous alteration is regional. Exploration by the rover of the marginal carbonates observed at the base of Jezero's inner rim where strong signatures of carbonates have been detected from orbit [e.g., (*8*)] will help identify the variability in this alteration and provide further constraints on its nature, diversity, and origin. Salts observed within Máaz were formed after the emplacement of these rocks, likely by filling pores and vesicles from a top-down aqueous circulation. Assuming the delta deposits were emplaced subsequent to the Cf-fr unit (*17*), the origin of salt deposition may be connected to the period of lake activity within Jezero crater, especially since the lake was closed for a substantial fraction of its history (*3*) and was therefore favorable to evaporative salt precipitation.

A notable finding of this work is the limited nature of alteration in the Jezero lake basin. It is difficult to extrapolate to any limits on the duration of the lake, since relative timing of the igneous activity can only be constrained to have occurred before the latest period of delta formation (*3*). A lake could well have existed before the igneous activity that emplaced the Máaz and Séítah fms. Other conditions such as an impermeable layer could have limited the alteration of the igneous materials during the subsequent lacustrine period. In any case, observation of relatively unweathered igneous material in the floor of Jezero crater does suggest a relatively limited lacustrine period postdating emplacement of these igneous bodies.

Before the landing of Perseverance, the origin and lithology of Jezero crater's floor were strongly debated, whether igneous (lava flows or pyroclastic) or sedimentary (*7*, *8*, *12*–*17*, *20*, *41*). SuperCam's compositional observations throughout the traverse indicate an igneous origin for all of the Máaz fm, Artuby ridge, and Séítah fm (including the Content mb), showing a compositional progression and implying a gradient of increasing density from upper to lower units. As the lowest observed unit, with the highest apparent density, the olivine-rich Séítah fm has the characteristics of a cumulate. Artuby ridge is a compositionally distinct unit, richer in pyroxene, and intermediate in inferred density, potentially located stratigraphically between the other two units. We find that the entire traversed region shows interesting comparisons to the igneous martian meteorites, regarding both mineralogy and bulk composition (e.g., *50*). At a larger scale, the cumulate scenario (formed intrusively or by lava flows or by impact melts) may provide important clues to the igneous nature of the Nili Fossae region with its olivine enrichment (*30*, *40*, *41*, *52*, *55*, *56*, *58*, *60*) and will provide a framework for analyzing the drill cores collected by Perseverance in the crater's floor after their return to Earth.

METHODS

Experimental design

SuperCam uses a 110-mm-diameter telescope on the mast of the rover to project laser beams and collect light for all of its optical observations (*21*, *22*). Fields of view of the various spectral techniques are coboresighted and coaligned but of varying diameter. Elemental composition observations cover the size of the focused IR laser beam used for LIBS, ~350 μm in diameter. Raman and VIS reflectance spectra cover ~0.71 mrad (e.g., 1.9 mm at the median target distance of 2.7 m), while the IR spectra cover ~1.15 mrad (3.2 mm at the same distance). SuperCam's images cover 18.8 mrad at a resolution of ~0.050 mrad. SuperCam operates in a raster mode, typically obtaining spectra from 5 to 10 locations per target and enough images to cover the raster. The IR spectrometer scans across the 1.3- to 2.6-μm spectral range using an acousto-optic tunable filter (*23*). All other spectrometers use gratings to disperse the light by wavelength (*21*). The sections below are presented in the order in which they appear in the manuscript, starting with the RMI images.

RMI images and grain size studies

RMI images were corrected for vignetting and other artifacts using a flat-field template produced by imaging the Mars sky in defocused mode. Exposure durations were generally between 5 and 20 ms. The process of mosaic generation is described in text S5.

Two different color schemes were used for the RMI images in this work: natural color, which was obtained by refining the red, green, and blue pixel intensities based on observation of a white target on the rover (*61*). The Gaussian stretch offers a different view of the image, by enhancing color differences that would be more difficult to see in the more natural color images. To obtain this stretch, each color channel composing the image was stretched independently, such that the intensity distribution of the pixels in each color layer follows the same Gaussian distribution. All RMI images in Fig. 2 and fig. S2 are in natural color except Fig. 2F, which uses the Gaussian stretch to enhance the visibility of the grain edges.

Grain sizes and grain size distributions were calculated on the basis of measurements from RMI images in three different regions of Séítah (fig. S2). Individual and composite RMI images were imported into NIH ImageJ (https://imagej.nih.gov/ij/). Scales for each image set were determined on the basis of the distance from SuperCam to the target and imported for each image set into ImageJ. The resolution of the RMI allowed characterization of grain sizes down to ~160 μm. Further description, including conversion from two to three dimensions, is provided in text S2.

LIBS spectra and derived elemental compositions

Nearly all LIBS observations were made with 30 laser shots, and the spectra collected from the first five shots were discarded to avoid dust contamination. The remaining 25 spectra were averaged together and processed. Elemental compositions were derived from LIBS spectra by methods described in (*62*) involving a library of >1000 spectra from >320 standards. Onboard standards (*61*, *63*) were not used in the calibration model but, instead, were used to check its accuracy and precision. Targets used in Tables 1 and 2 spanned a range of distances from 2.0 to 6.5 m; data in Fig. 5A used a few points at longer distances. Tests of the calibration model and analysis of Mars observations suggest that accuracies and SDs remain relatively constant within this distance range (*62*).

For Figs. 1 (B to D), 3, and 6 and Table 1, all LIBS data on bedrock targets were used except for those taken at excessive distances and for points with TiO_2 > 2.4 wt % due to a known deficiency in calibration of high-Ti compositions. Some other points with TiO_2 > 2.0 wt % and low Al were also removed because of interferences with the Al peaks (*62*). Data were also removed if the total emission was less than 10^{14} photons per pulse per square millimeter per steradian per nanometer (*62*), which usually indicates poor focus, or if the major element total was excessively high, e.g., >120 wt %. Laboratory calibrations are ongoing to address and improve on the results provided here.

Downloaded from https://www.science.org on November 01, 2022

SuperCam elemental abundances in the form of eight major-element oxides (*62*) are normally used without normalization. Sums of less than 100 wt % can provide information about the presence of other constituents such as CO_2, SO_3, Cl, H_2O, P_2O_5, MnO, and other minor and trace elements, if present in sufficient abundances. The abundances in Table 2 have been normalized, since we are interested in the igneous composition and the unquantified elements are generally products of alteration. The exceptions are P_2O_5 when present as apatite, and MnO, which is often in solution with Fe and Ti in mafic phases. The normalization makes exception for these elements using a total of 98 instead of 100 wt %. This is consistent with 0.4 wt % of MnO (quantification described in text S6) and the observation of a small amount of Ca-phosphorous materials by both SuperCam and PIXL, estimated on the order of 1.6 wt %. Table S3 gives the equivalent details without normalization.

Modal mineral abundances in Table 2 were derived, assuming that 5% of Fe is in the +3 charge state, with 95% in the +2 state. This assumption is consistent with the presence of iron oxides that we observed, especially in the Máaz fm. Assuming a larger fraction of Fe in the +2 state results in no iron oxides (contrary to those observed) and slightly higher olivine abundances in Séítah and Artuby. Modal mineral abundances for 0 and 10% Fe^{3+} are given in table S4.

The stoichiometric pyroxenes plotted in Fig. 5 were selected from all LIBS data up to Sol 217, calculating the stoichiometry using methods in (*64*). The selected pyroxene data points have a total of four (±0.2) total cations with six O including $Si^{4+} + Ti^{4+} = 2$ (±0.15) and Ti + Fe + Mg + Ca + Na + K = 2 (±0.15); $0 < Ca < 0.55$; $0.85 < (Fe + Mg + Ca)/Si < 1.15$; $Al/Si < 0.1$; 2 (±0.15) = $Si^{4+} + Ti^{4+}$; totals of the eight major-element oxides = 82 to 105 wt %; $Al_2O_3 <$ 5 wt %, $Na_2O <$ 1.5 wt %; and $K_2O <$ 0.5 wt %. The selected stoichiometric olivine data points have a total of three (±0.2) cations with four O including $Si^4+ = 1$ (±0.15) and (Fe + Mg)/Si in the range of 1.5 to 2, lower than the theoretical value of 2 but in agreement with the value measured on Mars on the onboard olivine standard (Fig. 3).

VISIR and Raman spectra

The VISIR spectra presented in Fig. 4A were obtained using two SuperCam spectrometers. VIS reflectance spectra were taken with a spectrometer covering 535 to 853 nm, the same used for LIBS and Raman spectra (*21*). Its calibration is described in (*65*). For each observation, 50 VIS spectra were collected and averaged on board for downlink. The IR spectra were collected with a wavelength-scanning spectrometer (*22*, *23*), using 80- to 140-μs exposures for each channel. The IR spectrometer was calibrated on the ground before launch (*66*). Full characterization of the instrument and its performance assessment are ongoing. Both VIS and IR spectra are ratioed to those collected on a white calibration target (*61*). Details of the laboratory spectra in Fig. 4B are given in text S7.

Data considered for IR band-depth statistics used rock targets of the Máaz fm, excluding observations with major shadowing, regolith and dust cover (validated by inspection of RMI images), radio-frequency power drops, and saturated measurements. The band depth was obtained by dividing the spectra (lightly smoothed using wavelet denoising) by their continuums (modeled as upper convex hulls of the spectra), where one minus the continuum-removed spectra values at the band centers is equal to the band depth (*67*). For the 2.28-μm band depth, bands centered between 2.26 and 2.3 μm were considered. This is generally the Fe-OH absorption range and the extent of band positions observed in the Máaz fm spectra. For attribution of pyroxene in the Máaz fm and Artuby ridge, spectral deconvolution was used (*68*).

A SuperCam Raman spectrum obtained from a light-toned spot in the Bellegarde abrasion patch displayed peaks diagnostic of sodium perchlorate, shown in Fig. 4C. This spectrum was obtained by averaging the signal accumulated over 200 laser shots at 10 Hz, collected in 20 exposures of 905 ms each with the intensifier gain set to 3400. All of the Raman spectra were processed by denoising the signal, subtracting the nonlaser "dark" spectra, and removing a laser-induced signal produced in the ~6-m fiber connecting the telescope on the mast with the spectrometers in the rover body (*21*).

Uncertainties

Average elemental abundances in Table 1 are accompanied by the SEM, which is the SD divided by the square root of the number of observations. This SE is useful for comparing compositions to determine whether they differ from each other. SEMs are generally applicable for Gaussian distributions, which is not necessarily the case with the data presented here (see fig. S4 for histograms). Figure S3 shows distributions by quartile. Text S3 associated with figs. S4 and S5 show additional details on the statistical differences between the units.

Precisions for single observations, such as the points displayed in Figs. 1 (B to D), 3, 5, and 6 and figs. S3 and S8, were obtained from SDs of elemental abundances derived from observations made on a large number of standards during cleanroom characterization and on rover calibration targets (*62*). General precisions for SiO_2, TiO_2, Al_2O_3, FeO_T, MgO, CaO, Na_2O, and K_2O are ±1.6, 0.06, 0.7, 1.3, 0.5, 0.5, 0.3, 0.3 wt %, respectively [using the largest values from (*62*)]. These precisions were propagated from oxide weight % to molar abundances where applicable.

Accuracies are useful for comparisons with other instruments or to mineral compositions. SuperCam elemental abundance accuracies were determined by tests against standards that were not used to build the calibration models. The absolute accuracies vary as a function of the abundance of each element. General averaged one-sigma accuracies for SiO_2, TiO_2, Al_2O_3, FeO_T, MgO, CaO, Na_2O, and K_2O are ±6.1, 0.3, 1.8, 3.1, 1.1, 1.3, 0.5, 0.6 wt %, respectively (*62*). On the basis of experience with ChemCam, these are thought to be overly conservative in most cases, but it is possible that, for olivines, FeO_T and/or MgO accuracies are not within these standard accuracies, given that they are somewhat extreme values relative to the spectral library (see text S8).

The uncertainties associated with the derived densities reported in Table 2 were obtained by propagating the SEMs toward higher density compositions (increasing Fe and Mg; decreasing Si, Al, Na, and K), and vice versa. These uncertainties are measures of the precision, useful for comparing between units, e.g., to show that the density differences are statistically significant. Absolute accuracy of the predicted mineral compositions is given in table S5 and was obtained by propagating the accuracy extremes toward different mafic and felsic mineral groups, similar to the process described above for density.

SUPPLEMENTARY MATERIALS

Supplementary material for this article is available at https://science.org/doi/10.1126/sciadv.abo3399

Downloaded from https://www.science.org on November 01, 2022

REFERENCES AND NOTES

1. J. A. Grant, M. P. Golombek, S. A. Wilson, K. A. Farley, K. H. Williford, A. Chen, The science process for selecting the landing site for the 2020 Mars rover. *Planet. Space Sci.* **164**, 106–126 (2018).
2. C. I. Fassett, J. W. Head III, Fluvial sedimentary deposits on Mars: Ancient deltas in a crater lake in the Nili Fossae region. *Geophys. Res. Lett.* **32**, L14201 (2005).
3. N. Mangold, S. Gupta, O. Gasnault, G. Dromart, J. D. Tarnas, S. F. Sholes, B. Horgan, C. Quantin-Nataf, A. J. Brown, S. Le Mouelic, R. A. Yingst, J. F. Bell, O. Beyssac, T. Bosak, F. Calef III, B. L. Ehlmann, K. A. Farley, J. P. Grotzinger, K. Hickman-Lewis, S. Holm-Alwmark, L. C. Kah, J. Martinez-Frias, S. M. McLennan, S. Maurice, J. I. Nunez, A. M. Ollila, P. Pilleri, J. W. Rice Jr., M. Rice, J. I. Simon, D. L. Shuster, K. M. Stack, V. Z. Sun, A. H. Treiman, B. P. Wiess, R. C. Wiens, A. J. Williams, N. R. Williams, K. H. Williford, Perseverance rover reveals an ancient delta-lake system and flood deposits at Jezero crater, Mars. *Science* **374**, 711–717 (2021).
4. B. L. Ehlmann, J. F. Mustard, S. L. Murchie, F. Poulet, J. L. Bishop, A. J. Brown, W. M. Calvin, R. N. Clark, D. J. Des Marais, R. E. Milliken, L. H. Roach, T. L. Roush, G. A. Swayze, J. J. Wray, Orbital identification of carbonate-bearing rocks on Mars. *Science* **322**, 1828–1832 (2008).
5. B. L. Ehlmann, J. F. Mustard, G. A. Swayze, R. N. Clark, J. L. Bishop, F. Poulet, D. J. Des Marais, L. H. Roach, R. E. Milliken, J. J. Wray, O. Barnouin-Jha, S. L. Murchie, Identification of hydrated silicate minerals on Mars using MRO-CRISM: Geologic context near Nili Fossae and implications for aqueous alteration. *J. Geophys. Res.* **114**, E00D08 (2009).
6. A. J. Brown, S. J. Hook, A. M. Baldridge, J. K. Crowley, N. T. Bridges, B. J. Thomson, G. M. Marion, C. R. de Souza Filho, J. L. Bishop, Hydrothermal formation of clay-carbonate alteration assemblages in the Nili Fossae region of Mars. *Earth Planet. Sci. Lett.* **297**, 174–182 (2010).
7. T. A. Goudge, J. F. Mustard, J. W. Head, C. I. Fassett, S. M. Wiseman, Assessing the mineralogy of the watershed and fan deposits of the Jezero crater paleolake system, Mars. *J. Geophys. Res. Planets* **120**, 775–808 (2015).
8. B. H. N. Horgan, R. B. Anderson, G. Dromart, E. S. Amador, M. S. Rice, The mineral diversity of Jezero crater: Evidence for possible lacustrine carbonates on Mars. *Icarus* **339**, 113526 (2020).
9. A. M. Zastrow, T. D. Glotch, Distinct carbonate lithologies in Jezero crater, Mars. *Geophys. Res. Lett.* **48**, e2020GL092365 (2021).
10. J. D. Tarnas, K. M. Stack, M. Parente, A. H. D. Koeppel, J. F. Mustard, K. R. Moore, B. H. N. Horgan, F. P. Seelos, E. A. Cloutis, P. B. Kelemen, D. Flannery, A. J. Brown, K. R. Frizzell, P. Pinet, Characteristics, origins, and biosignature preservation potential of carbonate-bearing rocks within and outside of Jezero crater. *J. Geophys. Res. Planets* **126**, e2021JE006898 (2021).
11. J. B. Pollack, J. F. Kasting, S. M. Richardson, K. Poliakoff, The case for a wet, warm climate on early Mars. *Icarus* **71**, 203–224 (1987).
12. T. A. Goudge, J. F. Mustard, J. W. Head, C. I. Fassett, Constraints on the history of open-basin lakes on Mars from the composition and timing of volcanic resurfacing. *J. Geophys. Res. Planets* **117**, E00J21 (2012).
13. T. A. Goudge, R. E. Milliken, J. W. Head, J. F. Mustard, C. I. Fassett, Sedimentological evidence for a deltaic origin of the western fan deposit in Jezero crater, Mars and implications for future exploration. *Earth Planet. Sci. Lett.* **458**, 357–365 (2017).
14. S. Shahrzad, K. M. Kinch, T. A. Goudge, C. I. Fassett, D. H. Needham, C. Quantin-Nataf, C. P. Knudsen, Crater statistics on the dark-toned, mafic floor unit in Jezero crater, Mars. *Geophys. Res. Lett.* **46**, 2408–2416 (2019).
15. K. M. Stack, N. R. Williams, F. Calef III, V. Z. Sun, K. H. Williford, K. A. Farley, S. Eide, D. Flannery, C. Hughes, S. R. Jacob, L. C. Kah, F. Meyen, A. Molina, C. Quantin-Nataf, M. Rice, P. Russell, E. Scheller, C. H. Seeger, W. J. Abbey, J. B. Adler, H. Amundsen, R. B. Anderson, S. M. Angel, G. Arana, J. Atkins, M. Barrington, T. Berger, R. Borden, B. Boring, A. Brown, B. L. Carrier, P. Conrad, H. Dypvik, S. A. Fagents, Z. E. Gallegos, B. Garczynski, K. Golder, F. Gomez, Y. Goreva, S. Gupta, S.-E. Hamran, T. Hicks, E. D. Hinterman, B. N. Horgan, J. Hurowitz, J. R. Johnson, J. Lasue, R. E. Kronyak, Y. Liu, J. M. Madariaga, N. Mangold, J. McClean, N. Miklusicak, D. Nunes, C. Rojas, K. Runyon, N. Schmitz, N. Scudder, E. Shaver, J. SooHoo, R. Spaulding, E. Stanish, L. K. Tamppari, M. M. Tice, N. Turenne, P. A. Willis, R. A. Yingst, Photogeologic map of the Perseverance rover field site in jezero crater constructed by the Mars 2020 Science team. *Space Sci. Rev.* **216**, 217 (2020).
16. V. Z. Sun, K. M. Stack, Geologic Map of Jezero Crater and the Nili Planum Region, Mars, USGS Scientific Investigations Map 3464 (2020); https://doi.org/10.3133/sim3464.
17. S. Holm-Alwmark, K. M. Kinch, M. D. Hansen, S. Shahrzad, K. Svennevig, W. J. Abbey, R. B. Anderson, F. J. Calef III, S. Gupta, E. Hauber, B. H. N. Horgan, L. C. Kah, J. Knade, N. B. Miklusicak, K. M. Stack, V. Z. Sun, J. D. Tarnas, C. Quantin-Nataf, Stratigraphic relationships in Jezero crater, Mars: Constraints on the timing of fluvial-lacustrine activity from orbital observations. *J. Geophys. Res. Planets* **126**, e2021JE006840 (2021).
18. J. F. Mustard, M. Adler, A. Allwood, D. S. Bass, D. W. Beaty, J. F. Bell III, W. B. Brinckerhoff, M. Carr, D. J. Des Marais, B. Drake, K. S. Edgett, J. Eigenbrode, L. T. Elkins-Tanton, J. A. Grant, S. M. Milkovich, D. Ming, C. Moore, S. Murchie, T. C. Onstott, S. W. Ruff, M. A. Sephton, A. Steele, A. Treiman, "Report of the Mars 2020 Science Definition Team" (Mars Exploration Program Analysis Group, 2013), 154 pp; http://mepag.jpl.nasa.gov/reports/MEP/Mars_2020_SDT_Report_Final.pdf.
19. D. W. Beaty, M. M. Grady, H. Y. McSween, E. Sefton-Nash, B. L. Carrier, F. Altieri, Y. Amelin, E. Ammannito, M. Anand, L. G. Benning, J. L. Bishop, L. E. Borg, D. Boucher, J. R. Brucato, H. Busemann, K. A. Campbell, A. D. Czaja, V. Debaille, D. J. Des Marais, M. Dixon, B. L. Ehlmann, J. D. Farmer, D. C. Fernandez-Remolar, J. Filiberto, J. Fogarty, D. P. Glavin, Y. S. Goreva, L. J. Hallis, A. D. Harrington, E. M. Hausrath, C. D. K. Herd, B. Horgan, M. Humayun, T. Kleine, J. Kleinhenz, R. Mackelprang, N. Mangold, L. E. Mayhew, J. T. McCoy, F. M. McCubbin, S. M. McLennan, D. E. Moser, F. Moynier, J. F. Mustard, P. B. Niles, G. G. Ori, F. Raulin, P. Rettberg, M. A. Rucker, N. Schmitz, S. P. Schwenzer, M. A. Sephton, R. Shaheen, Z. D. Sharp, D. L. Shuster, S. Siljeström, C. L. Smith, J. A. Spry, A. Steele, T. D. Swindle, I. L. ten Kate, N. J. Tosca, T. Usui, M. J. Van Kranendonk, M. Wadhwa, B. P. Weiss, S. C. Werner, F. Westall, R. M. Wheeler, J. Zipfel, M. P. Zorzano, The potential science and engineering value of samples delivered to Earth by Mars sample return: International MSR Objectives and Samples Team (iMOST). *Meteorit Planet. Sci.* **54**, S3–S152 (2019).
20. S. C. Schon, J. W. Head, C. I. Fassett, An overfilled lacustrine system and progradational delta in Jezero crater, Mars: Implications for Noachian climate. *Planet. Spa. Sci.* **67**, 28–45 (2012).
21. R. C. Wiens, S. Maurice, S. H. Robinson, A. E. Nelson, P. Cais, P. Bernardi, R. T. Newell, S. Clegg, S. K. Sharma, S. Storms, J. Deming, D. Beckman, A. M. Ollila, O. Gasnault, R. B. Anderson, Y. André, S. M. Angel, G. Arana, E. Auden, P. Beck, J. Becker, K. Benzerara, S. Bernard, O. Beyssac, L. Borges, B. Bousquet, K. Boyd, M. Carey, J. Carlson, K. Castro, J. Celis, B. Chide, K. Clark, E. Cloutis, E. C. Cordoba, A. Cousin, M. Dale, L. Deflores, D. Delapp, M. Deleuze, M. Dirmyer, C. Donny, G. Dromart, M. G. Duran, M. Egan, J. Ervin, C. Fabre, A. Fau, W. Fischer, O. Forni, T. Fouchet, R. Fresquez, J. Frydenvang, D. Gasway, I. Gontijo, J. Grotzinger, X. Jacob, S. Jacquinod, J. R. Johnson, R. A. Klisiewicz, J. Lake, N. Lanza, J. Laserna, J. Lasue, S. Le Mouelic, C. Legett, R. Leveille, E. Lewin, G. Lopez-Reyes, R. Lorenz, E. Lorigny, S. P. Love, B. Lucero, J. M. Madariaga, M. Madsen, S. Madsen, N. Mangold, J. A. Manrique, J. P. Martinez, J. Martinez-Frias, K. P. McCabe, T. H. McConnochie, J. M. McGlown, S. M. McLennan, N. Melikechi, P.-Y. Meslin, J. M. Michel, D. Mimoun, A. Misra, G. Montagnac, F. Montmessin, V. Mousset, N. Murdoch, H. Newsom, L. A. Ott, Z. R. Ousnamer, L. Pares, Y. Parot, R. Pawluczyk, C. G. Peterson, P. Pilleri, P. Pinet, G. Pont, F. Poulet, C. Provost, B. Quertier, H. Quinn, W. Rapin, J.-M. Reess, A. H. Regan, A. L. Reyes-Newell, P. J. Romano, C. Royer, F. Rull, B. Sandoval, J. H. Sarrao, V. Sautter, M. J. Schoppers, S. Schroeder, D. Seitz, T. Shepherd, P. Sobron, B. Dubois, V. Sridhar, M. J. Toplis, I. Torre-Fdez, I. A. Trettel, M. Underwood, A. Valdez, J. Valdez, D. Venhaus, P. Willis, The SuperCam instrument suite on the NASA Mars 2020 rover: Body unit and combined system tests. *Space Sci. Rev.* **217**, 4 (2021).
22. S. Maurice, R. C. Wiens, P. Bernardi, P. Cais, S. Robinson, T. Nelson, O. Gasnault, J. M. Reess, M. Deleuze, F. Rull, J. A. Manrique, S. Abbaki, R. B. Anderson, Y. Andre, S. M. Angel, G. Arana, T. Battault, P. Beck, K. Benzerara, S. Bernard, J. P. Berthias, O. Beyssac, M. Bonafous, B. Bousquet, M. Boutillier, A. Cadu, K. Castro, F. Chapron, B. Chide, K. Clark, E. Clavé, S. Clegg, E. Cloutis, C. Collin, E. C. Cordoba, A. Cousin, J. C. Dameury, W. D'Anna, Y. Daydou, A. Debus, L. Deflores, E. Dehouck, D. Delapp, G. De Los Santos, C. Donny, A. Doressoundiram, G. Dromart, B. Dubois, A. Dufour, M. Dupieux, M. Egan, J. Ervin, C. Fabre, A. Fau, W. Fischer, O. Forni, T. Fouchet, J. Frydenvang, S. Gauffre, M. Gauthier, V. Gharakanian, O. Gilard, I. Gontijo, R. Gonzalez, D. Granena, J. Grotzinger, R. Hassen-Khodja, M. Heim, Y. Hello, G. Hervet, O. Humeau, X. Jacob, S. Jacquinod, J. R. Johnson, D. Kouach, G. Lacombe, N. Lanza, L. Lapauw, J. Laserna, J. Lasue, L. Le Deit, S. Le Mouelic, E. Le Comte, Q. M. Lee, C. Legett, R. Leveille, E. Lewin, C. Leyrat, G. Lopez-Reyes, R. Lorenz, B. Lucero, J. M. Madariaga, S. Madsen, M. Madsen, N. Mangold, F. Manni, J. F. Mariscal, J. Martinez-Frias, K. Mathieu, R. Mathon, K. P. McCabe, T. McConnochie, S. M. McLennan, J. Mekki, N. Melikechi, P. Y. Meslin, Y. Micheau, Y. Michel, J. M. Michel, D. Mimoun, A. Misra, G. Montagnac, C. Montaron, F. Montmessin, J. Moros, V. Mousset, Y. Morizet, N. Murdoch, R. T. Newell, H. Newsom, N. Nguyen Tuong, A. M. Ollila, G. Orttner, L. Oudda, L. Pares, J. Parisot, Y. Parot, R. Perez, D. Pheav, L. Picot, P. Pilleri, C. Pilorget, P. Pinet, G. Pont, F. Poulet, C. Quantin-Nataf, B. Quertier, D. Rambaud, W. Rapin, P. Romano, L. Roucayrol, C. Royer, M. Ruellan, B. F. Sandoval, V. Sautter, M. J. Schoppers, S. Schroeder, H. C. Seran, S. K. Sharma, P. Sobron, M. Sodki, A. Sournac, V. Sridhar, D. Standarovsky, S. Storms, N. Striebig, M. Tatat, M. Toplis, I. Torre-Fdez, N. Toulemont, C. Velasco, M. Veneranda, D. Venhaus, C. Virmontois, M. Viso, P. Willis, K. W. Wong, The SuperCam instrument suite on the Mars 2020 rover: Science objectives and mast-unit description. *Space Sci. Rev.* **217**, 47 (2021).
23. T. Fouchet, J.-M. Reess, F. Montmessin, R. Hassen-Khodja, N. Nguyen-Tuong, O. Humeau, S. Jacquinod, L. Lapauw, J. Parisot, M. Bonafous, P. Bernardi, F. Chapron, A. Jeanneau, C. Collin, D. Zeganadin, P. Nibert, S. Abbaki, C. Montaron, C. Blanchard, V. Arslanyan, O. Achelhi, C. Colon, C. Royer, V. Hamm, M. Beuzit, F. Poulet, C. Pilorget, L. Mandon, O. Forni, A. Cousin, O. Gasnault, P. Pilleri, B. Dubois, C. Quantin, P. Beck, O. Beyssac, S. Le Mouelic,

Downloaded from https://www.science.org on November 01, 2022

J. R. Johnson, T. H. McConnochie, S. Maurice, R. C. Wiens, The SuperCam infrared spectrometer for the Perseverance rover of the Mars 2020 mission. *Icarus* **373**, 114773 (2022).
24. K. A. Farley, K. M. Stack, B. H. N. Horgan, J. Tarnas, V. Z. Sun, D. L. Shuster, J. I. Simon, J. A. Hurowitz, K. R. Moore, E. L. Scheller, M. E. Schmidt, T. V. Kizovski, P. S. Russell, P. Vasconcelos, N. J. Tosca, O. Beyssac, T. Bosak, B. L. Ehlmann, L. E. Mayhew, S. M. McLennan, A. H. Treiman, R. C. Wiens, K. H. Williford, *et al.*, Aqueously altered igneous rocks on the floor of Jezero crater, Mars. *Science*, abo2196 (2022).
25. S.-E. Hamran, D. A. Paige, H. E. F. Amundsen, T. Berger, S. Brovoll, L. Carter, T. Casademont, L. Damsgard, H. Dypvik, S. Eide, R. Ghent, J. Kohler, M. Mellon, D. C. Nunes, D. Plettemeier, P. Russell, M. Siegler, M. J. Oyan, Ground penetrating radar observations of subsurface structures in the floor of Jezero crater, Mars. *Sci. Adv.* **8**, abp8564 (2022).
26. J. Bell *et al.*, Geological and meteorological imaging results from the Mars 2020 Perseverance rover in Jezero crater. *Sci. Adv.* **8**, abo4856 (2022).
27. H. W. Nesbitt, R. E. Wilson, Recent chemical weathering of basalts. *Am. J. Sci.* **292**, 740–777 (1992).
28. E. B. Rampe, D. F. Blake, T. F. Bristow, D. W. Ming, D. T. Vaniman, R. V. Morris, C. N. Achilles, S. J. Chipera, S. M. Morrison, V. M. Tu, A. S. Yen, N. Castle, G. W. Downs, R. T. Downs, J. P. Grotzinger, R. M. Hazen, A. H. Treiman, T. S. Peretyazhko, D. J. D. Marais, R. C. Walroth, P. I. Craig, J. A. Crisp, B. Lafuente, J. M. Morookain, P. C. Sarrazin, M. T. Thorpe, J. C. Bridges, L. A. Edgar, C. M. Fedo, C. Freissinet, R. Gellert, P. R. Mahaffy, H. E. Newsom, J. R. Johnson, L. C. Kah, K. L. Siebach, J. Schieber, V. Z. Sun, A. R. Vasavada, D. Wellington, R. C. Wiens; MSL Science Team, Mineralogy and geochemistry of sedimentary rocks and eolian sediments in Gale crater, Mars: A review after six Earth years of exploration with Curiosity. *Geochemistry* **80**, 125605 (2020).
29. Y. Liu, M. M. Tice, M. E. Schmidt, A. H. Treiman, T. V. Kizovski, J. A. Hurowitz, A. C. Allwood, J. Henneke, D. A. K. Pedersen, S. J. VanBommel, M. W. M. Jones, A. L. Knight, B. J. Orenstein, B. C. Clark, W. T. Elam, C. M. Heirwegh et al., An olivine cumulate outcrop on the floor of Jezero crater, Mars. *Sci. Adv.* **8**, abo2756 (2022).
30. A. J. Brown, C. E. Viviano, T. A. Goudge, Olivine-carbonate mineralogy of the Jezero Crater region. *J. Geophys. Res. Planets* **125**, e2019JE006011 (2020).
31. J. Filiberto, R. Dasgupta, Fe2+-Mg partitioning between olivine and basaltic melts: Applications to genesis of olivine-phyric shergottites and conditions of melting in the martian interior. *Earth Planet. Sci. Lett.* **304**, 527–537 (2011).
32. N. H. Sleep, B. F. Windley, Archean plate tectonics: Constraints and inferences. *J. Geol.* **90**, 363–379 (1982).
33. O. Namur, B. Abily, G. Ceuleneer, A. E. Boudreau, F. Blanchette, J. W. M. Bush, B. Charlier, J.-C. Duchesne, M. D. Higgins, D. Morata, T. F. D. Nielson, B. O'driscoll, K. N. Pang, T. Peacock, C. J. Spandler, A. Toramaru, I. V. Veksler, Igneous layering in basaltic magma chambers, in *Layered Intrusions*, B. Charlier, O. Naur, R. Latypov, C. Tegner, Eds. (Springer, 2015), pp. 75–152.
34. M. W. Schmidt, M. Forien, G. Solferino, N. Bagdassarov, Settling and compaction of olivine in basaltic magmas: An experimental study on the time scales of cumulate formation. *Contrib. Mineral. Petrol.* **164**, 959–976 (2012).
35. C. Paola, S. M. Wiele, M. A. Reinhart, Upper-regime parallel lamination as the result of turbulent sediment transport and low-amplitude bed forms. *Sedimentology* **36**, 47–59 (1989).
36. J. Bridge, J. Best, Preservation of planar laminae due to migration of low-relief bed waves over aggrading upper-stage plane beds: Comparison of experimental data with theory. *Sedimentology* **44**, 253–262 (1997).
37. D. A. V. Stow, M. Johansson, Deep-water massive sands: Nature, origin, and hydrocarbon implications. *Mar. Pet. Geol.* **17**, 145–174 (2000).
38. P. E. Potter, A. E. Scheidegger, Bed thickness and grain size: Graded beds. *Sedimentology* **7**, 233–240 (1966).
39. F. Felletti, R. Bersezio, Validation of Hurst statistics: A predictive tool to discriminate turbiditic sub-environments in a confined basin. *Pet. Geosci.* **16**, 401–412 (2010).
40. C. H. Kremer, M. S. Bramble, J. F. Mustard, Origin and emplacement of the circum-Isidis olivine-rich unit. *Lunar Planet. Sci.* **49**, 1545 (2018).
41. L. Mandon, C. Quantin-Nataf, P. Thollot, N. Mangold, L. Lozac'h, G. Dromart, P. Beck, E. Dehouck, S. Breton, C. Millot, M. Volat, Refining the age, emplacement and alteration scenarios of the olivine-rich unit in the Nili Fossae region, Mars. *Icarus* **336**, 113436 (2020).
42. N. A. Stroncik, H.-U. Schmincke, Evolution of palagonite: Crystallization, chemical changes, and element budget. *Geochem. Geophys. Geosyst.* **2**, 2000GC000102 (2001).
43. J. H. J. Bedard, The development of compositional and textural layering in Archaean komatiites and in Proterozoic komatiitic basalts from Cape Smith, Quebec, Canada, in *Origins of Igneous Layering*, I. Parsons, Ed. (D. Reidel, 1987) pp. 399–418.
44. C. D. K. Herd, Reconciling redox: Making spatial and temporal sense of oxygen fugacity variations in martian igneous rocks. *Lunar Planet. Sci.* **50**, 2746 (2019).
45. T. J. Lapen, M. Righter, R. Andreasen, A. J. Irving, A. M. Satkoski, B. L. Beard, K. Nishiizumi, A. J. T. Jull, M. W. Caffee, Two billion years of magmatism recorded from a single Mars meteorite ejection site. *Sci. Adv.* **3**, e1600922 (2017).
46. A. Udry, J. M. D. Day, 1.34 billion-year-old magmatism on Mars evaluated from the co-genetic nakhlite and chassignite meteorites. *Geochim. Cosmochim. Acta* **238**, 292–315 (2018).
47. A. Udry, G. H. Howarth, T. J. Lapen, M. Righter, Petrogenesis of the NWA 7320 enriched martian gabbroic shergottite: Insight into the martian crust. *Geochim. Cosmochim. Acta* **204**, 1–18 (2017).
48. D. Xirouchakis, D. S. Draper, C. S. Schwandt, A. Lanzirotti, Crystallization conditions of Los Angeles, a basaltic Martian meteorite. *Geochim. Cosmochim. Acta* **66**, 1867–1880 (2002).
49. A. R. Santos, C. B. Agee, F. M. McCubbin, C. K. Shearer, P. V. Burger, R. Tartèse, M. Anand, Petrology of igneous clasts in Northwest Africa 7034: Implications for the petrologic diversity of the martian crust. *Geochim. Cosmochim. Acta* **157**, 56–85 (2015).
50. A. Udry, G. H. Howarth, C. Herd, J. M. D. Day, T. J. Lapen, J. Filiberto, What martian meteorites reveal about the interior and surface of Mars. *J. Geophys. Res. Planets* **55**, e2020JE006523 (2020).
51. R. R. Rahib, A. Udry, G. H. Howarth, J. Gross, M. Paquet, L. M. Combs, D. L. Laczniak, J. M. D. Day, Mantle source to near-surface emplacement of enriched and intermediate poikilitic shergottites in Mars. *Geochim. Cosmochim. Acta* **266**, 463–496 (2019).
52. P. Pinet, S. Chevrel, Spectral identification of geological units on the surface of Mars related to the presence of silicates from Earth-based near-infrared telescopic charge-coupled device imaging. *J. Geophys. Res.* **95**, 14435–14446 (1990).
53. J. C. Bridges, L. J. Hicks, A. H. Treiman, Chapter 5 - Carbonates on Mars, in *Volatiles in the Martian Crust*, J. Filiberto, S. P. Schwenzer, Eds. (Elsevier, 2019) pp. 89–118.
54. A. Steele, L. G. Benning, R. Wirth, A. Schreiber, T. Araki, F. M. McCubbin, M. D. Fries, L. R. Nittler, J. Wang, L. J. Hallis, P. G. Conrad, C. Conley, S. Vitale, A. C. O'Brien, V. Riggi, K. Rogers, Organic synthesis associated with serpentinization and carbonation on early Mars. *Science* **375**, 172–177 (2022).
55. W. C. Koeppen, V. E. Hamilton, Global distribution, composition, and abundance of olivine on the surface of Mars from thermal infrared data. *J. Geophys. Res.* **113**, E05001 (2008).
56. A. Ody, F. Poulet, J.-P. Bibring, D. Loizeau, J. Carter, B. Gondet, Y. Langevin, Global investigation of olivine on Mars: Insights into crust and mantle compositions. *J. Geophys. Res. Planets* **118**, 234–262 (2013).
57. A. D. Rogers, N. H. Warner, M. P. Golombek, J. W. Head III, J. C. Cowart, Areally extensive surface bedrock exposures on Mars: Many are clastic rocks, not lavas. *Geophys. Res. Lett.* **45**, 1767–1777 (2018).
58. J. F. Mustard, F. Poulet, J. W. Head, N. Mangold, J.-P. Bibring, S. M. Pelkey, C. I. Fassett, Y. Langevin, G. Neukum, Mineralogy of the Nili Fossae region with OMEGA/Mars Express data: 1. Ancient impact melt in the Isidis Basin and implications for the transition from the Noachian to Hesperian. *J. Geophys. Res.* **112**, E08S03 (2007).
59. L. Richan, H. L. Gibson, M. G. Houlé, C. M. Lesher, Mode of emplacement of Archean komatiitic tuffs and flows in the Selkirk Bay area, Melville Peninsula, Nunavut, Canada. *Precambrian Res.* **263**, 174–196 (2015).
60. M. S. Bramble, J. F. Mustard, M. R. Salvatore, The geological history of Northeast Syrtis Major, Mars. *Mars. Icarus* **293**, 66–93 (2017).
61. J. A. Manrique, G. Lopez-Reyes, A. Cousin, F. Rull, F. S. Maurice, R. C. Wiens, M. B. Madsen, J. M. Madariaga, O. Gasnault, J. Aramendia, G. Arana, P. Beck, S. Bernard, P. Bernardi, M. H. Bernt, A. Berrocal, O. Beyssac, P. Cais, C. Castro, K. Castro, S. M. Clegg, E. Cloutis, G. Dromart, C. Drouet, B. Dubois, D. Escribano, C. Fabre, A. Fernandez, O. Forni, V. Garcia-Baonza, I. Gontijo, J. Johnson, J. Laserna, J. Lasue, S. Madsen, E. Mateo-Marti, J. Medina, P.-Y. Meslin, G. Montagnac, A. Moral, J. Moros, A. M. Ollila, C. Ortega, O. Prieto-Ballesteros, J. M. Reess, S. Robinson, J. Rodriguez, J. Saiz, J. A. Sanz-Arranz, I. Sard, V. Sautter, P. Sobron, M. Toplis, M. Veneranda, SuperCam calibration targets: Design and development. *Space Sci. Rev.* **216**, 138 (2020).
62. R. B. Anderson, O. Forni, A. Cousin, R. C. Wiens, S. M. Clegg, J. Frydenvang, T. S. J. Gabriel, A. Ollila, S. Schroeder, O. Beyssac, E. Gibbons, D. S. Vogt, E. Clavé, J.-A. Manrique, C. Legett IV, P. Pilleri, R. T. Newell, J. Sarrao, S. Maurice, G. Arana, K. Benzerara, P. Bernardi, S. Bernard, B. Bousquet, A. J. Brown, C. Alverez-Llamas, B. Chide, E. Cloutis, J. Comellas, S. Connell, E. Dehouck, D. M. Delapp, A. Essunfeld, C. Fabre, T. Fouchet, C. Garcia-Florentino, L. Garcia-Gomez, P. Gasda, O. Gasnault, E. Hausrath, N. L. Lanza, J. Laserna, J. Lasue, G. Lopez, J. M. Madariaga, L. Mandon, N. Mangold, P.-Y. Meslin, M. Nachon, A. E. Nelson, H. Newsom, A. L. Reyes-Newell, S. Robinson, F. Rull, S. Sharma, J. I. Simon, P. Sobron, I. T. Fernandez, A. Udry, D. Venhaus, S. M. McLennan, R. V. Morris, B. Ehlmann, Post-landing major element quantification using SuperCam laser induced breakdown spectroscopy. *Spectrochim. Acta Part B At. Spectrosc.* **188**, 106347 (2022).
63. A. Cousin, V. Sautter, C. Fabre, G. Dromart, G. Montagnac, C. Drouet, P.-Y. Meslin, O. Gasnault, O. Beyssac, S. Bernard, E. Cloutis, O. Forni, P. Beck, T. Fouchet, J. R. Johnson, J. Lasue, A. M. Ollila, P. De Parseval, S. Gouy, B. Caron, J. M. Madariaga, G. Arana, M. B. Madsen, J. Laserna, J. Moros, J. A. Manrique, G. Lopez-Reyes, F. Rull, S. Maurice, R. C. Wiens, SuperCam calibration targets on board the Perseverance rover: Fabrication and quantitative characterization. *Spectrochim. Acta Part B At. Spectrosc.* **188**, 106341 (2021).
64. V. Payré, K. L. Siebach, R. Dasgupta, A. Udry, E. B. Rampe, S. M. Morrison, Constraining ancient magmatic evolution on Mars using crystal chemistry of detrital igneous minerals

Downloaded from https://www.science.org on November 01, 2022

in the sedimentary Bradbury group, Gale crater, Mars. *J. Geophys. Res. Planets* **125**, e2020JE006467 (2020).
65. C. Legett IV, R. T. Newell, A. L. Reyes-Newell, A. E. Nelson, P. Bernardi, S. C. Bener, O. Forni, D. M. Venhaus, S. M. Clegg, A. M. Ollila, P. Pilleri, V. Sridhar, S. Maurice, R. C. Wiens, Optical calibration of the SuperCam instrument body unit spectrometers. *Appl. Optics* **61**, 2967–2974 (2022).
66. C. Royer, F. Poulet, J.-M. Reess, C. Pilorget, V. Hamm, T. Fouchet, S. Maurice, O. Forni, R. C. Wiens, Pre-launch radiometric calibration of the infrared spectrometer onboard SuperCam for the Mars2020 rover. *Rev. Sci. Instrum.* **91**, 063105 (2020).
67. L. Mandon, P. Beck, C. Quantin-Nataf, E. Dehouck, A. Pommerol, Z. Yoldi, R. Cerubini, L. Pan, M. Martinot, V. Sautter, Martian meteorites reflectance and implications for rover missions. *Icarus* **366**, 114517 (2021).
68. L. Mandon, C. Quantin-Nataf, C. Royer, P. Beck, T. Fouchet, J. R. Johnson, O. Forni, F. Montmessin, C. Pilorget, F. Poulet, S. Le Mouelic, E. Dehouck, O. Beyssac, A. Brown, J. Tarnas, S. Maurice, R. C. Wiens, SuperCam team, Infrared reflectance of rocks and regolith at Jezero crater: One year of SuperCam Observations. *Lunar Planet Sci.* **LIII**, 1631 (2022).
69. G. Montagnac, "Raman spectra of some chlorate minerals" (SSHADE/REAP, OSUG Data Center, Dataset/Spectral Data, 2000). doi:10.26302/SSHADE/EXPERIMENT_GM_20220122, www.sshade.eu/data/EXPERIMENT_GM_20220122.
70. C. Cornwall, J. L. Bandfield, T. N. Titus, B. C. Schrieber, D. R. Montgomery, Physical abrasion of mafic minerals and basalt grains: Application to martian aeolian deposits. *Icarus* **256**, 13–21 (2015).
71. M. D. Higgins, Measurement of crystal size distributions. *Am. Mineral.* **85**, 1105–1116 (2000).
72. D. J. Morgan, D. A. Jerram, On estimating crystal shape for crystal size distribution analysis. *J. Volcanol. Geotherm. Res.* **154**, 1–7 (2006).
73. P. J. Gasda, R. B. Anderson, M. Dubey, A. Cousin, O. Forni, S. M. Clegg, A. M. Ollila, N. Lanza, R. C. Wiens, Multivariate and ensemble manganese calibration models for SuperCam, in *53rd Lunar and Planetary Science Conference*, The Woodlands, Texas, 7 to 11 March 2022 abstract #1646, The Lunar and Planetary Institute (2022).
74. G. J. Taylor, The bulk composition of Mars. *Chem. Erde* **73**, 401–420 (2013).
75. J. L. Bishop, Visible and near-infrared reflectance spectroscopy, in *Remote Compositional Analysis: Techniques for Understanding Spectroscopy, Mineralogy, and Geochemistry of Planetary Surfaces* (Cambridge Univ. Press, 2019), pp. 68–101.
76. J. L. Bishop, M. D. Lane, M. D. Dyar, A. J. Brown, Reflectance and emission spectroscopy study of four groups of phyllosilicates: Smectites, kaolinite-serpentines, chlorites and micas. *Clay Miner.* **43**, 35–54 (2008).
77. J. Hanley, V. F. Chevrier, B. L. Davis, T. S. Altheide, A. Francis, Reflectance spectra of low-temperature chloride and perchlorate hydrates and their relevance to the martian surface, in The New Martian Chemistry Workshop, abstract #8010, the Lunar and Planetary Institute (2009).
78. C. M. Pieters, T. Hiroi, RELAB (Reflectance Experiment Laboratory): A NASA multiuser spectroscopy facility, in *Lunar Planetary Science Conference*, XXXV, abstract #1720, the Lunar and Planetary Institute (2004).
79. E. L. Scheller, J. R. Hollis, E. L. Cardarelli, A. Steele, L. W. Beegle, R. Bhartia, P. Conrad, K. Uckert, S. Sharma, B. L. Ehlmann, W. J. Abbey, S. A. Asher, K. C. Benison, E. L. Berger, B. L. Bleefeld, A. S. Burton, S. V. Bykov, L. DeFlores, K. A. Farley, D. M. Fey, T. Fornaro, A. C. Fox, M. Fries, K. Hickman-Lewis, J. E. Huggett, S. Imbeah, L. C. Kah, P. Kelmen, M. R. Kennedy, T. Kizovski, C. Lee, F. M. McCubbin, K. Moore, B. E. Nixon, C. R. Sanchez-Vahamonde, R. D. Roppel, S. Siljeström, J. I. Simon, S. O. Shkolyar, D. Shuster, R. J. Smith, K. S. Morgan, K. Steadman, A. Werynski, A. J. Williams, B. Wogsland, R. C. Wiens, K. H. Williford, K. Winchell, R. Wingling, A. Yanchilina, SHERLOC Team, Aqueous alteration processes and implications for organic geochemistry in Jezero crater, Mars. *Sci. Adv.* **8**, abo5204 (2022).

Acknowledgments: We are grateful to all of the Mars 2020 Project participants who have made this work possible, including the science definition team and management; those who developed the hardware for the rover, the launch vehicle, and the cruise stage; those participating in the cruise operation and landing; and those operating the rover and its instruments. SDG. **Funding:** Funding was provided by the following sources: NASA's Mars exploration program, including contracts NNH15AZ24I and NNH13ZDA018O to LANL. LANL LDRD code XWHW contributed to calibrations. A portion of this research was carried out at the Jet Propulsion Laboratory, California Institute of Technology, under a contract with the National Aeronautics and Space Administration (80NM0018D0004). NASA RSSPS grants supported J.I.S., grant number 80NSSC20K0239 supported L. Hausrath, grant number 80NSSC20K0240 supported L. Mayhew, and grant number 80NSSC21K0330 supported A.U. CNRS and CNES supported the work in France. DLR supported S.Sc. and D.S.V. The Swedish National Space Agency (contracts 137/19 and 2021-00092) supported S.Si. The Natural Sciences and Engineering Research Council of Canada (NSERC) and the Canadian Space Agency (CSA) supported E.C., S.C., and N.T. The Ministry of Economy and Competitiveness (MINECO, SPAIN) grant PID2019-107442RB-C31 supported F.R., G.L.R., J.A.M., and M.V. **Author contributions:** Investigation/operations: R.C.W., A.U., O.B., C.Q.-N., N.Ma., A.C., L.May., T.Bo., O.F., S.M., A.B., K.B., J.R.J., L.May., S.M.M., R.B.A., S.M.C., L.C., B.H.N.H., L.K., C.L., J.M.M., P.-Y.M., A.M.O., S.K.S., J.I.S., T.E.A.-M., C.A.-L., S.M.A., G.A., P.B., T.B., K.C., B.C., E.C., S.C., E.D., G.D., T.F., R.F., J.F., O.G., E.G., S.G., L.H., X.J., H.K., E.Ke., E.Kn., J.L., G.L.R., J.A.M., T.M., F.M., N.M., P.P., C.R., D.L.S., S.Si., A.S., R.J.S., J.T., N.T., M.V., D.S.V., B.P.W., P.W., K.M.S., K.H.W., and K.A.F. Calibrations: R.C.W., A.U., O.B., A.C., L.Man., O.F., K.B., S.M., R.B.A., S.M.C., T.S.J.G., P.G., C.L., J.M.M., P.-Y.M., A.M.O., F.P., T.E.A., S.M.A., G.A., P.B., S.B., T.B., B.B., E.C., E.D., T.F., O.G., L.H., N.L., R.Le., G.L.R., N.Me., J.A.M., T.M., F.M., P.Pil., C.P., W.R., C.R., S.Sc., and D.S.V. Supervision: R.C.W., O.B., C.Q.-N., A.C., O.F., J.R.J., S.M., S.M.C., J.M.M., A.M.O., E.C., W.F., T.F., O.G., J.Lasu., R.Lo., G.L.R., D.M., F.R., K.M.S., K.H.W., and K.A.F. Visualization/images/plots: R.C.W., A.U., O.B., C.Q.-N., N.Ma., L.Man., T.B., S.M., K.B., S.M.M., L.C., T.S.J.G., J.H., C.L., J.M.M., G.D., O.G., S.L.M., and P.Pil. Writing—original drafts: R.C.W., A.U., O.B., C.Q.-N., N.Ma., L.Man., T.Bo., S.M., V.S., A.B., K.B., J.R.J., L.May., S.M.M., P.G., J.H., L.K., P.-Y.M., S.Si., C.A.-L., and K.M.S. Writing—review and editing: R.C.W., A.U., O.B., C.Q.-N., N.Ma., L.Man., T.B., S.M., V.S., A.B., J.R.J., L.May., S.M.M., B.H.N.H., F.P., S.K.S., S.Si., J.I.S., B.B., E.C., E.D., J.F., L.H., J.M.-F., N.M., F.M., J.M., C.P., P.Pin., D.L.S., R.J.S., J.T., B.P.W., and P.W. Various members of the SuperCam Team also contributed in operations and calibrations. **Competing interests:** The authors declare that they have no competing interests. **Data and materials availability:** All data are available in the NASA Planetary Data System (https://pds-geosciences.wustl.edu/missions/mars2020/supercam.htm), in the paper, and/or the Supplementary Materials.

Submitted 7 February 2022
Accepted 31 May 2022
Published 25 August 2022
10.1126/sciadv.abo3399

Downloaded from https://www.science.org on November 01, 2022

Science Advances

Compositionally and density stratified igneous terrain in Jezero crater, Mars

Roger C. WiensArya UdryOlivier BeyssacCathy Quantin-NatafNicolas MangoldAgnès CousinLucia MandonTanja BosakOlivier ForniScott M. McLennanViolaine SautterAdrian BrownKarim BenzeraraJeffrey R. JohnsonLisa MayhewSylvestre MauriceRyan B. AndersonSamuel M. CleggLarry CrumplerTravis S. J. GabrielPatrick GasdaJames HallBriony H. N. HorganLinda KahCarey Legett IVJuan Manuel MadariagaPierre-Yves MeslinAnn M. OllilaFrancois PouletClement RoyerShiv K. SharmaSandra SiljeströmJustin I. SimonTayro E. Acosta-MaedaCesar Alvarez-LlamasS. Michael AngelGorka AranaPierre BeckSylvain BernardTanguy BertrandBruno BousquetKepa CastroBaptiste ChideElise ClavéEd CloutisStephanie ConnellErwin DehouckGilles DromartWoodward FischerThierry FouchetRaymond FrancisJens FrydenvangOlivier GasnaultErin GibbonsSanjeev GuptaElisabeth M. HausrathXavier JacobHemani KaluchaEvan KellyElise KnutsenNina LanzaJavier LasernaJeremie LasueStéphane Le MouélicRichard LeveilleGuillermo Lopez ReyesRalph LorenzJose Antonio ManriqueJesus Martinez-FriasTim McConnochieNoureddine MelikechiDavid MimounFranck MontmessinJavier MorosNaomi MurdochPaolo PilleriCedric PilorgetPatrick PinetWilliam RapinFernando RullSusanne SchröderDavid L. ShusterRebecca J. SmithAlexander E. StottJesse TarnasNathalie TurenneMarco VenerandaDavid S. VogtBenjamin P. WeissPeter WillisKathryn M. StackKenneth H. WillifordKenneth A. Farley

Sci. Adv., 8 (34), eabo3399. • DOI: 10.1126/sciadv.abo3399

View the article online
https://www.science.org/doi/10.1126/sciadv.abo3399
Permissions
https://www.science.org/help/reprints-and-permissions

Downloaded from https://www.science.org on November 01, 2022

Use of this article is subject to the Terms of service

Science Advances (ISSN) is published by the American Association for the Advancement of Science. 1200 New York Avenue NW, Washington, DC 20005. The title *Science Advances* is a registered trademark of AAAS.
Copyright © 2022 The Authors, some rights reserved; exclusive licensee American Association for the Advancement of Science. No claim to original U.S. Government Works. Distributed under a Creative Commons Attribution NonCommercial License 4.0 (CC BY-NC).

Science Advances
AAAS

Supplementary Materials for

Compositionally and density stratified igneous terrain in Jezero crater, Mars

Roger C. Wiens *et al.*

Corresponding author: Roger C. Wiens, rwiens@purdue.edu

Sci. Adv. **8**, eabo3399 (2022)
DOI: 10.1126/sciadv.abo3399

The PDF file includes:

Texts S1 to S11
Figs. S1 to S8
Tables S1 to S6
Legends for data S1 to S3
Legend for Reference S1
References

Other Supplementary Material for this manuscript includes the following:

Data S1 to S3
Reference S1

Supplementary Text

S1. Máaz fm Compositions: Pavers vs. Ch'al-like

Throughout the early portion of the traverse, to Sol 177, two main types of bedrock morphologies were encountered. One type corresponds to flat-lying rocks called pavers, while the second type corresponds to high-standing rocks that protrude above the ground. We use the term "Ch'al-like" for rocks that protrude significantly above the surface. The term comes from a Máaz fm member identified in (24) as characterized by massive boulders to the east of the traverse. The member was named after target "Ch'al" that was observed by SuperCam VISIR at a distance of > 15 m. While no rocks of the Ch'al mb were observed by LIBS up to Sol 289, the Ch'al target showed VISIR spectral similarities to high-standing rocks along the traverse. Additionally, RMI, LIBS, and VISIR observations were made in the Ch'al mb shortly after Sol 289 which confirmed that the Ch'al-like rocks presented here are in fact the same or at least very similar to the Ch'al mb rocks. The high-standing rocks along the traverse are thus "Ch'al-like," not technically part of the Ch'al mb in the current definition in (24) but compositionally, morphologically, and texturally very similar.

Both pavers and Ch'al-like targets are granular. Pavers are dustier and therefore lighter-toned whereas the Ch'al-like rocks are darker. Some Ch'al-like rocks are rounded and not blocky. The classification between these types of rocks was made visually from the context images, either the Navcam mosaic or the Mastcam-Z images. We used the description and science rationale described by the uplink operational team, and revised it when appropriate, using the Mastcam-Z documentation images. Float rocks and a few layered targets at Mure were not included in either of these two categories.

Table S2 shows the mean compositions of targets classified as pavers and as Ch'al-like in the Máaz fm up to Sol 177. The trend from more evolved Ch'al-like rocks to more primitive pavers does not represent contamination of the latter by dust or by a coating having the composition of dust. Our elemental calibration gives a FeO_T abundance for fine-grained regolith material in Jezero of ~14 wt%, significantly lower than the FeO_T abundance of Ch'al-like rocks (16.6±1.0 wt%), and much lower than that of pavers (19.5±0.8 wt%; Table S2). Attributing paver compositions to a combination of Ch'al-like rock and fine-grained dust does not work, as the trend goes the wrong direction. The difference in composition also cannot be attributed to a silica coating on Ch'al-like rocks, as they are also enriched in aluminum and alkali elements. Likewise, aqueous alteration to produce paver compositions from Ch'al-like rocks does not seem to have occurred, as no significant Al-enriched clay minerals were seen (Fig. 6). Leaching would decrease the relative concentration of MgO along with K_2O, Na_2O, CaO, and SiO_2, and increase relative concentrations of Al_2O_3, TiO_2, and ferric Fe, and these trends are not seen. Physical abrasion to produce pavers also does not work, as it preferentially removes mafic minerals (70).

Analysis was done to determine whether Ch'al-like rocks represent a topographically and stratigraphically higher original position than the pavers do. All of the Ch'al-like targets except for one come from near the landing site and the Van Zyl helicopter observation site (all Sol < 120) and show a slight trend of decreasing SiO_2 with increasing sol # (Fig. 1B). The OEB landing site is several meters higher than the latter part of the traverse through the Máaz fm prior to Artuby ridge, e.g., at the southern point of Séítah. However, the difference is minor, such that potential dips of the strata would result in more vertical difference than the current topography. In that sense, much of the later part of the traverse through the Máaz fm east of Séítah was much closer to Séítah than the original landing site is (Fig. 1A). Hamran et al. (25) indicates subsurface layers are dipping away from Séítah on its eastern side, similar to that seen on the SW side by RIMFAX in the subsurface and visually at the surface along Artuby ridge, adding further elevation difference to the original orientation of the bedrock. In summary, the portion of the traverse farthest eastward of Séítah, where the most Ch'al-like targets were observed, is likely the highest-elevation portion of the traverse in terms of the original stratigraphic positions of the rocks. However, given the current data, a quantitative estimate of original relative elevations is not feasible.

S2. Grain Size Distributions

Size frequency distributions have been used widely in the geosciences to understand the formation and emplacement of geological deposits. The broad utility of these datasets derives from the distinctive shapes of size frequency distributions, which provide critical information about the nucleation and growth of crystals in an open system, changes in crystal size during maturation under closed system conditions, and the physical segregation of size populations.

The grains within the RMI images were readily defined by having discrete, identifiable edges in the best cases (e.g., Fig. 2F). In these samples, the rare instances where grains may have been intergrown were not measured, and the majority of the matrix around individual grains in the Séítah region is not identifiable as containing discrete grains. Visual determination of grain size, however, is affected by the pixel scale of the RMI images. RMI images have a target-projected pixel size of 37 to 92 µm over the most common range of distances (2-5 m) used to identify grain scale textures of rocks. Identification of grain size and the initial recognition of grain edges typically used 5-10 pixels; in this sample, the absence of clearly identifiable matrix suggested grain sizes within the matrix less than ~160 µm. However, most RMI targets preserved surfaces that either have been polished by wind abrasion, or were in various states of disintegration, in which case grains are harder to identify. In these cases, grains were measured where the surface permitted unique identification of grain edges, or where grain facets could be readily identified and differentiated from adjacent grains.

An initial measurement set of 25 grains per target image set was used to determine the extent to which two-dimensional shape was likely to affect measurements. These measurements showed that grains are dominantly equant (defined as the ratio between the longest axis and the perpendicular short axis being < 1:2). The presence of largely equant grains reduces the need to use of software to convert 2D to 3D crystal measurements that are based on known grain mineralogy (71, 72). Such conversion is also unsuited to these measurements because the mineralogical composition of individual grains is not generally known.

In all cases, Séítah materials show a tight grain size distribution, with a broadly normal distribution, where the similarity of mean and mode describe only slight skewness, to both larger and smaller grain sizes. Many Séítah targets around Bastide and Brac outcrops (Bastide and Caille regions, respectively, Fig. S2) reveal crystals with a mean diameter of 1.53±0.08 mm, and only the stratigraphically uppermost exposed Séítah layers (targets Issole and Sagnes, located in the Issole region) show finer grain size, with an average of 1.07±0.09 mm.

S3. Statistical Analysis of Compositional Differences between the Máaz fm, Artuby Ridge, and Séítah

Figure S4 shows histograms of major element oxide distributions in the Máaz fm, Artuby ridge, and Séítah. Statistical analyses were made to show the significant differences among combinations of elements. SiO_2+Al_2O_3 is significantly higher in the Máaz fm compared to Artuby (Kolmogorov Smirnov and Mann-Whitney tests $p < 10^{-5}$) and Séítah (Kolmogorov Smirnov and Mann-Whitney tests $p < 10^{-5}$), but not significantly different from the pitted rocks of the Content mb. Séítah has a significantly lower alkali sum compared to Artuby (Fig. S4B; Kolmogorov Smirnov and Mann-Whitney tests $p < 10^{-5}$), Máaz fm (Kolmogorov Smirnov and Mann-Whitney tests $p < 10^{-5}$) and Content mb (Kolmogorov Smirnov and Mann-Whitney tests $p < 10^{-5}$). The sum of FeO+MgO (Fig. S4C) is significantly higher in Séítah compared to Artuby (Kolmogorov Smirnov and Mann-Whitney tests $p < 10^{-5}$) and Máaz (Kolmogorov Smirnov and Mann-Whitney tests $p < 10^{-5}$). A similar increase from Máaz to Séítah is observed in MgO wt% data alone. Artuby rocks have the highest CaO content, followed by Máaz (Kolmogorov Smirnov and Mann-Whitney tests $p < 10^{-5}$) and then Séítah (Kolmogorov Smirnov and Mann-Whitney tests $p < 10^{-5}$). The Content mb rocks in the Séítah fm have higher values of Na_2O +

K_2O wt% compared to the rocks in Máaz, but exhibit no other statistically significant differences among the major element oxide weight percents. The same tests confirm the statistical significance among the values of major element oxide compositions stated in Table 1.

An analysis was done by using the Principal Component Analysis (PCA) method, using as input the abundances of the elements presented in Table 1, averaged by target. The results are shown in Figure S5 as a plot of the scores between PC-2 (second Principal Component) and PC-1 that explain 64% of the total variance among samples. The positive PC-1 range is related to Al_2O_3, Na_2O and K_2O while the negative PC-1 direction is related to FeO_T and MgO, such that more felsic rocks (feldspar and plagioclase) are located in the right part of the plot while more mafic rocks (olivine and Fe-rich pyroxenes) are in the left part. A positive PC-2 range is related to TiO_2 and CaO enrichments, suggesting increased augite. The positions on Fig. S5 of mineral standards on board the rover reinforce these trends.

S4. Additional Details on Table 2: Data Subset, Normalization, and CIPW Norm Assumptions

For the CIPW norm calculations shown in Table 2, we extracted the igneous compositions, removing the alteration products as much as possible. Some of the key elements present in alteration products are not currently quantified, including S, Cl, C, and H due to weak emission lines or other challenges in calibration. These elements normally comprise the missing material, not present in the sum of the eight element oxides quantified by LIBS (SiO_2, TiO_2, Al_2O_3, FeO_T, MgO, CaO, Na_2O, and K_2O). We can assume they have been added during alteration. To retrieve the original igneous compositions, we can normalize our compositions to near 100 wt% without them. One element that was likely part of the original igneous composition that is not quantified by LIBS is phosphorous, and along with Mn, we reserve 2.0 wt% for the oxides of these two elements plus any additional minor to trace elements unaccounted for (e.g., Cr_2O_3, NiO), thus normalizing the eight quantified elements to 98.0 wt% as described in Methods.

However, this simple normalization does not remove excess of cations that would have been the product of deposition of salts. We can explore their influence by looking at the observation points with low major-element totals (Data File S1). Our investigation suggests that up to 20-25% of the MgO and a lesser percentage of CaO in Máaz could be due to accumulation of sulfates and other precipitates. On the other hand, in Séítah, it is likely that MgO and FeO are scavenged in place by carbonate to produce the alteration products there. We minimize the effects of alteration by removing the points with the lowest totals, below 80 wt%. This removed slightly more than 20% of the data points in Artuby, which has the highest fraction of low totals. The largest proportional effect was on MgO, consistent with the reports in the section on alteration that one of the main alteration products is hydrated Mg sulfate. A specific comparison of normalized abundances before and after removing points with totals < 80 wt% indicates that all mean abundances of the units are within 0.2 wt% of their previous values except as follows: MgO in Artuby dropped by 0.7 wt%, a nearly 20% reduction, given its relatively low abundance prior to the modification; CaO dropped by 0.3 wt% in Artuby, a reduction of slightly less than 5%; Al_2O_3 in Artuby dropped by 0.6 wt%, a reduction of < 10%; FeO_T increased in the Máaz fm by 1.0 wt%, indicating low iron in the removed points. The resulting mean abundances are given for each unit in the top portion of Table 2.

To obtain the CIPW norm mineral abundances in the lower portion of Table 2, we estimated $Fe^{2+}/\Sigma Fe = 0.95$, which was used based on the presence of a few iron oxide grains observed by SuperCam. The effect of varying the iron oxidation state is shown in Table S4 for $Fe^{2+}/\Sigma Fe = 1.0$ and 0.90. The main differences are the presence and abundance of iron oxide grains and the abundances of pyroxene and olivine, making 8.4 wt% difference on the latter. While we used the same oxidation state for all three units, the units could in fact have different oxidation states.

While the CIPW norm calculation is useful, it gives model results that are not necessarily correct for the conditions at Jezero crater. The CIPW norm was designed to model crystallization in a homogeneous melt, not a cumulate. The calculated density is that produced by melts of a given composition as they cool, not taking into account porosity. In Máaz, quartz is suggested by the model although the dataset contains only one point with $SiO_2 > 75$ wt%. Actual quartz, if it occurred in large enough grains, would plot in Figure 3 at the origin, and what we see instead are many points that are lower than plagioclase and to the left of diopside, suggesting excess silica, potentially on rims of grains or interstitially. This excess silica could be quartz grains that are too small to identify as such by SuperCam, or they could be some unidentified phase. Another mineral, orthoclase, is inferred by potassium abundances, although no pure orthoclase was observed with LIBS, and VISIR did not observe orthoclase signatures.

Finally, we propagated the mean accuracy of the LIBS calibration (62) to the CIPW norm in the same way that we did for the precision of the density, given in Methods. The results shown in Table S5, indicates that, within error, it is possible that the olivine abundance of Séítah could be as high as the upper 50s wt%. Apatite is not derived from LIBS (the small P_2O_5 abundance is assumed), so it is not shown in Tables 2 and S3. Density is not given in Table S5 because we are interested in the differences in density more than their absolute numbers. The precision uncertainty for density is given in Table 2.

S5. RMI Mosaic Generation

RMI mosaics were produced starting from SuperCam's processed products ("CDR" files, for Clean Data Records), following these steps. First, we optimized the relative positions of all images, in time order. Second, we stitched the images together using different fusion techniques to compute the region in which several RMI images overlap. Finally, we enhanced the contrast to produce a "Gaussian stretched" version of the mosaic shown in Fig. 2F.

To calculate the relative positions of the RMI images in a mosaic, we calculated the approximate relative position of the images using measured azimuth and elevation coordinates of the mast. Then, a match-filter algorithm refined this position by applying offsets (both in x and y) to the image added to the merge to find the maximum correlation position. Once these offsets were set, the images were merged together and the process was iterated over all the images forming the mosaic. At the end of this step, all the images were assigned x and y coordinates. We then produced a stitched image by merging overlapping regions.

S6. Manganese Abundances

Using a preliminary calibration for MnO (73), we have determined MnO compositions of the points observed by SuperCam. The median composition of the olivine- and pyroxene-rich Séítah bedrock is 0.44 wt% MnO, essentially identical to the bulk silicate Mars value of 0.44 wt% (74). Máaz, including Artuby ridge, has a median of ~0.32 wt% MnO, slightly less than Séítah. Only 17 targets up to sol 259 have > 1 wt% MnO, and all but three of these targets are in the Máaz fm. One target in particular, Tseebii (sol 112; Ch'al-like target), has ~11 wt% MnO. Some targets with 1-2 wt% MnO tend to be enriched in FeO_T, or have elevated CaO, Na_2O, and K_2O. The occurrence of a few localized MnO enrichments may imply either very local (closed system) aqueous alteration has occurred, or that fluids precipitated soluble elements within these targets. We tend to favor the former interpretation, as there are no obvious diagenetic textures (e.g., nodules, veins) within these targets.

S7. Additional Details on Fig. 4

The "Penne" spectrum exhibits a strong and large absorption in the 0.7-1.8 µm range, manifested as a rise in reflectance over this wavelength region, a feature related to the presence of Fe-bearing olivine (for a review, see 75). Additional absorptions at 1.93 µm and 2.32 µm indicate the presence of a hydrated phase and a carbonate or an Mg-OH-bearing phase respectively (for a review, see 75). The "Bidziil" spectrum shows absorptions at 1.42, 1.92, 2.28 and 2.40 µm, distinctive of the presence of Fe-phyllosilicates; the 2.28 µm band, in particular, is attributed to Fe-OH in nontronite (e.g., 76). The "Tsosts'idts'áadah" spectrum does not exhibit these absorptions, except for a band near 1.9 µm distinctive of water, that is enlarged and centered at longer wavelength (1.94 µm) compared to the "Bidziil" spectrum. Additionally, the "Tsosts'idts'áadah" spectrum shows a strong red slope in the 1.3-1.8 µm range indicative of Fe. Overall, these features are consistent with the presence of oxyhydroxide (for a review, see 76). The "Bellegarde" spectrum shows dual absorptions at 1.92 and 2.14 µm. This spectral feature is observed in laboratory spectra of monohydrated sulfates of the kieserite family (for a review, see 76) but was also reported for perchlorates (77), though perchlorate spectra are broadly lacking from spectral databases. Pure kieserite usually exhibits a weaker absorption in the 1.4-1.8 µm range which is not observed here. Finally, the "Guillaumes" spectrum shows spectral similarities with the "Bellegarde" spectrum, except for the absence of an absorption at 2.14 µm and the presence of a weak absorption near 2.2 µm. This is indicative of the presence of either an Al-OH phase, a Si-OH phase or gypsum (for a review, see 75).

All of the spectra shown in Fig. 4 except for the Máaz target were taken after LIBS, benefiting from the removal of dust provided by that technique. Additionally, Bellegarde and Guillaumes observations were made in abrasion patches, not on the rock surfaces. Laboratory reflectance spectra on minerals (Fig. 4B) come from the Reflectance Experiment Laboratory (RELAB) spectral library (78). The spectra are from F1CC15 (kieserite), CBJB26 (nontronite), C1JB45 (ferrihydrite), C1PO47 (olivine), and LACB06A (magnesite).

S8. Additional Details on LIBS Calibrations and Compositional Bias

The LIBS elemental calibration has not been fully optimized. The calibration uses a relatively large spectral library (62) with the on-board standards (61) left out, so they can be used as a check on the calibration accuracy. The onboard standards provide benchmarks for nearly pure

mineral compositions, and show some calibration biases. An example is in Fig. 3A, in which the onboard olivine standards plot below the expected value of (Mg+Fe)/Si = 2.0 due to an overestimation of the Si abundances in olivines. By comparison with MgO, the compositions derived from LIBS data on Mars slightly underestimate FeO in the olivine calibration target, yielding an average Mg number of 69 on Mars compared to 64 obtained by other means on Earth (62, 63). Consequently, all olivine Mg numbers on Mars that fall in a similar range as the olivine calibration target are likely overestimated by the same quantity. This likely bias has not been corrected. Another example of bias is the position of the andesine standard in Fig. 3A, which should ideally plot at molar Al/Si ~0.55. Inclusion of the onboard standards in the plot shows that the Jezero crater feldspars have An numbers equal to and below that of the andesine standard.

The biases shown by the onboard standards are generally within the stated (1-sigma) accuracy of the technique. The LIBS elemental calibration work is ongoing, and further advances require collection of additional spectra in the laboratory; the laboratory instrument is being set up for this work.

S9. SuperCam Elemental Chemistry in the Abrasion Patches.

Compositions obtained by SuperCam in the abrasion patches provide tie-points to observations (29, 79) made in their respective units by the PIXL and the Scanning Habitable Environments with Raman and Luminescence for Organics and Chemicals (SHERLOC) instruments. Both Guillaumes and Bellegarde have relatively low SiO_2 and MgO, as low as any unabraded targets along the traverse up to Guillaumes, and higher iron than the average compositions of the Máaz fm and Artuby ridge (Table 1). Although Guillaumes morphologically resembles a paver (26), it appears more similar in composition to the Artuby group and is less felsic compared to Máaz as observed earlier along the traverse. The Mars 2020 team's stratigraphic model places Guillaumes and Bellegarde only about ~2-3 m apart in elevation (26). Both abraded surfaces appear to be stratigraphically below a majority of the Máaz rocks explored earlier in the mission, those before Sol 135 (Fig. 1A). Within Séítah, the Garde and Dourbes abrasion patches appear to be more representative of the larger data set (344 observations) of SuperCam Séítah observations. Dourbes appears to be slightly lower in alkali elements, Al_2O_3, and SiO_2 relative to the overall Séítah data set (Table 1).

S10. Image sources

Image sources are given in Table S6. Designations are those from the NASA website where all raw imaging data are accessible: https://mars.nasa.gov/mars2020/multimedia/raw-images/. When Navcam and SuperCam images are mosaics made from a series of images, numbers correspond to the first and last image number of the series.

S11. Continuing List of SuperCam Team Members and Contributors

These SuperCam and Mars 2020 team members contributed to calibration of the instrument and collection of the data, and in rare cases, a comment on the manuscript. It is a continuing list from the co-authors listed at the beginning of the manuscript.

Daniel Applin[26], Roberta Beal[1], Pernelle Bernardi[7], Jean-Yves Bonnet[43], Magali Bouyssou Mann[43], Matthew Brand[1], Philippe Caïs[44], Gwénaël Caravaca[6], Antoine Charpentier[43], Jade Comellas[19], Lauren Deflores[28], Dorothea Delapp[1], Tomas Delgado[22], Christophe Donny[43], Alain Doressoundiram[7], Ari Essunfeld[1], Cecile Fabre[45], Alberto G. Fairen[46], Cristina Garcia-Florentino[17], Laura Gomez[22], Ivair Gontijo[28], Jennifer Huidobro[17], Gaetan Lacombe[33], Carene Larmat[1], Eric Lewin[24], Cynthia Little[47], Eric Lorigny[43], Morten Madsen[29], Frederique Meunier[43], Gilles Montagnac[4], Valerie Mousset[43], Anthony Nelson[1], Raymond Newell[1], Colleen O'Shea[11], Laurent Peret[43], John Porter[19], Adriana Reyes-Newell[1], Scott Robinson[47], Ludovic Rochas[43], Margaret Root[1], Joseph Sarrao[1], Mark A. Sephton[31],Amanda Sheridan[1], Uriah Wolf[26]

[43]Centre National d'Etudes Spatiales, Toulouse, France
[44]Laboratoire d'Astrophysique de Bordeaux (CNRS, Univ. Bordeaux), France
[45]GéoRessources, CNRS, Univ. Lorraine, Nancy, France
[46]Department of Astronomy, Cornell University, Ithaca, New York, USA
[47]Planetary Science Institute, Tucson, Arizona, USA

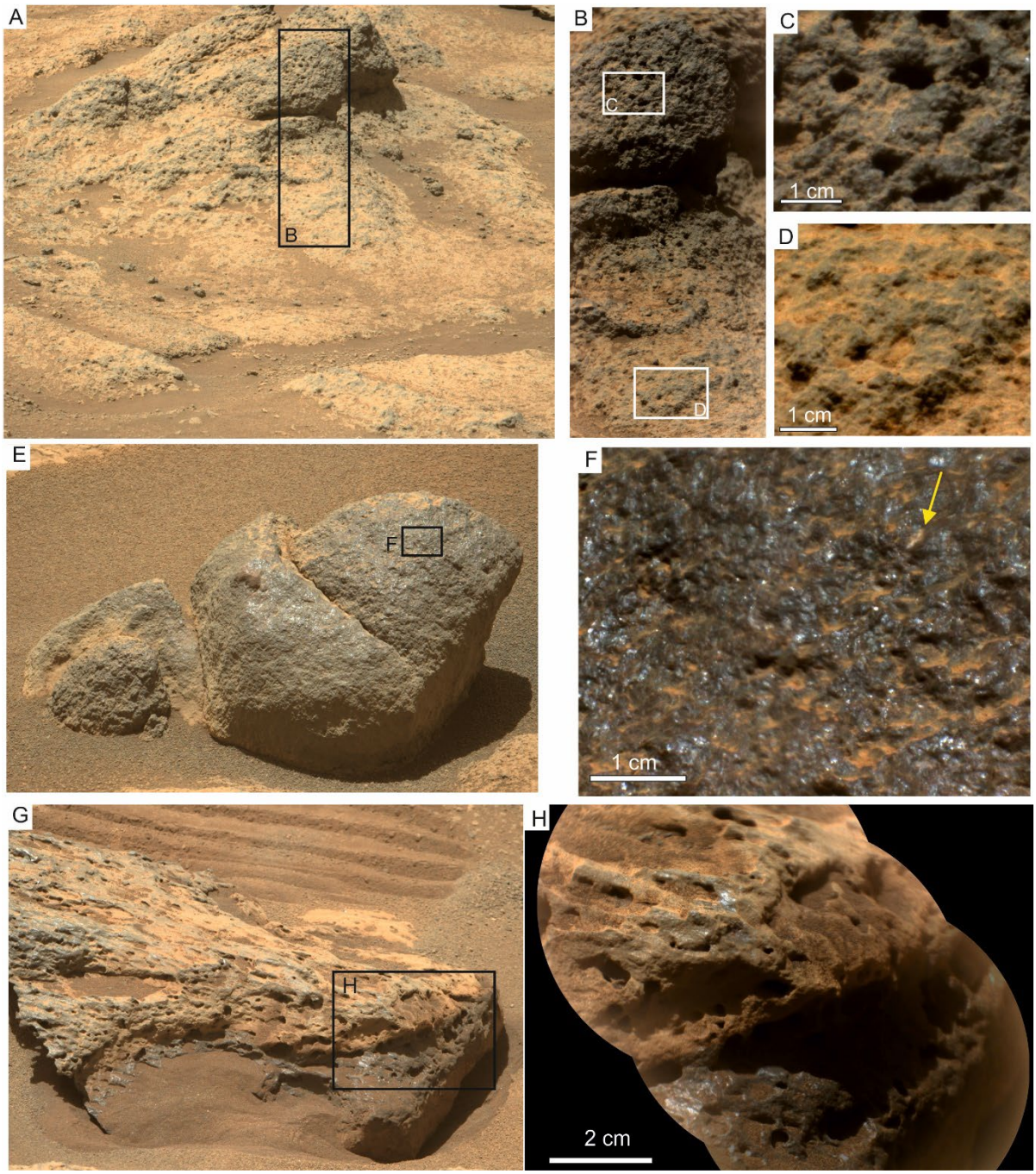

Fig. S1. **Rock textures at Mastcam-Z (left side) and SuperCam-RMI scale (right side). (A-D)** Target Mirabeau (sol 139) showing the transition from Máaz fm pavers to high-standing morphology. Rock texture is granular at mm-scale in both terrains and local pits. **(E-F)** Target Hoolhnili (Sol 86; Ch'al-like) with polished rock surface. Texture is granular at a mm scale and displays local light-toned grains (yellow arrow). **(G-H)** Target Raton (Sol 130; Máaz fm) displaying pitted texture with cm-scale cavities and no obvious grains visible. Image designations are given in Table S6.

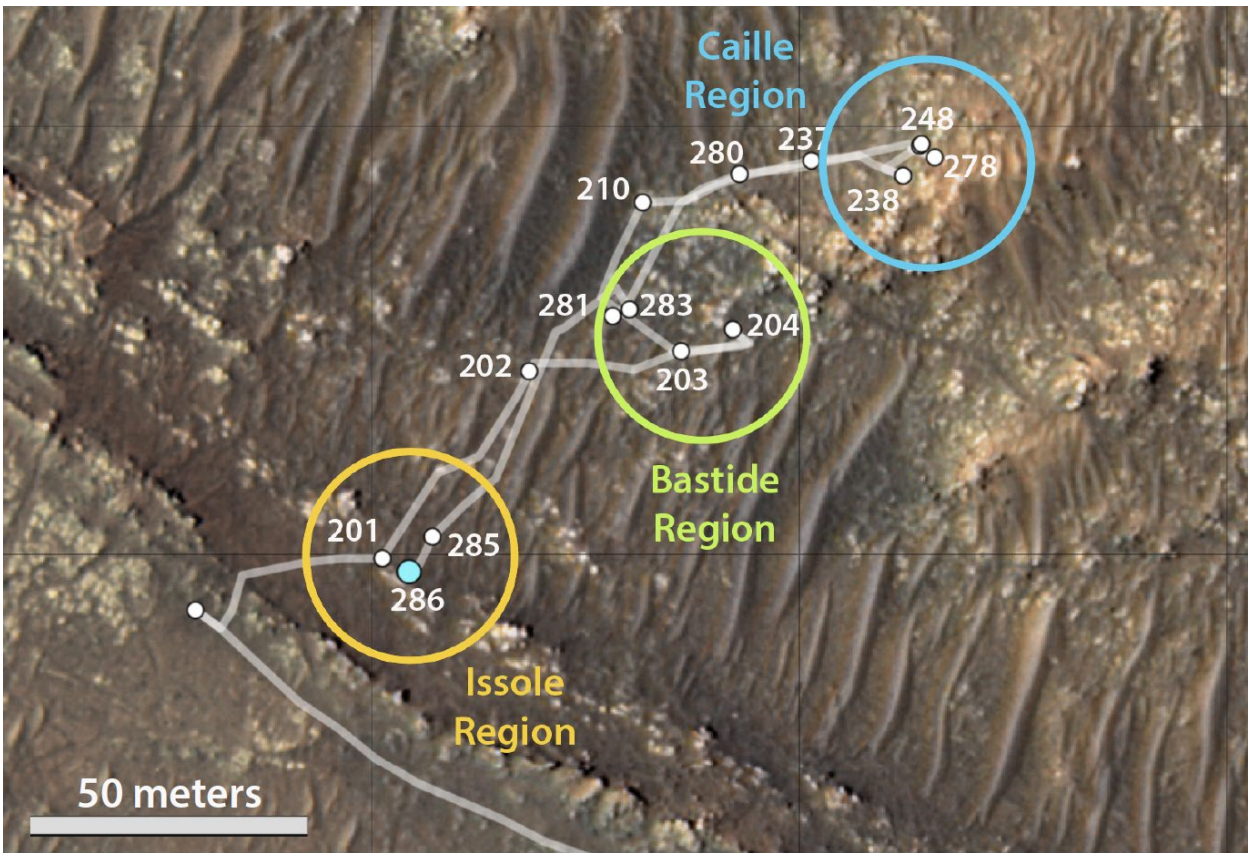

Fig. S2. Localities of grain-size analyses. RMI targets used in grain size analysis of Séítah targets, given in Table S1, are from these regions. Three discrete localities are noted, which reflect areas of intensive SuperCam observations. Image is from MRO/HiRISE. NASA/JPL-Caltech/ASU.

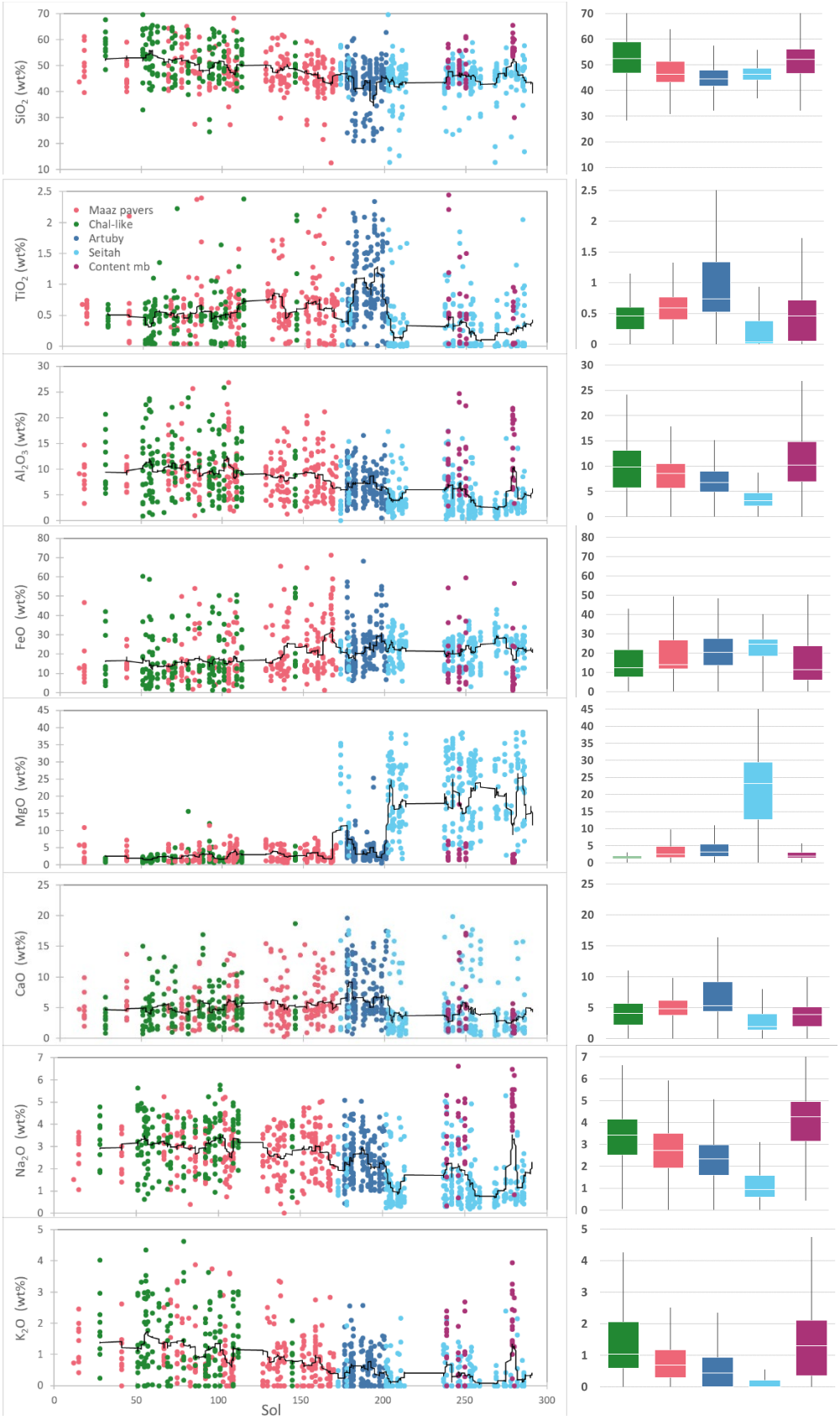

Fig. S3. Major element oxide compositions by sol number. A subset of these are in Fig. 1. The solid line is a running mean of 31 observations. Box plots at right show median, first and third quartiles, and tenth and ninetieth percentiles.

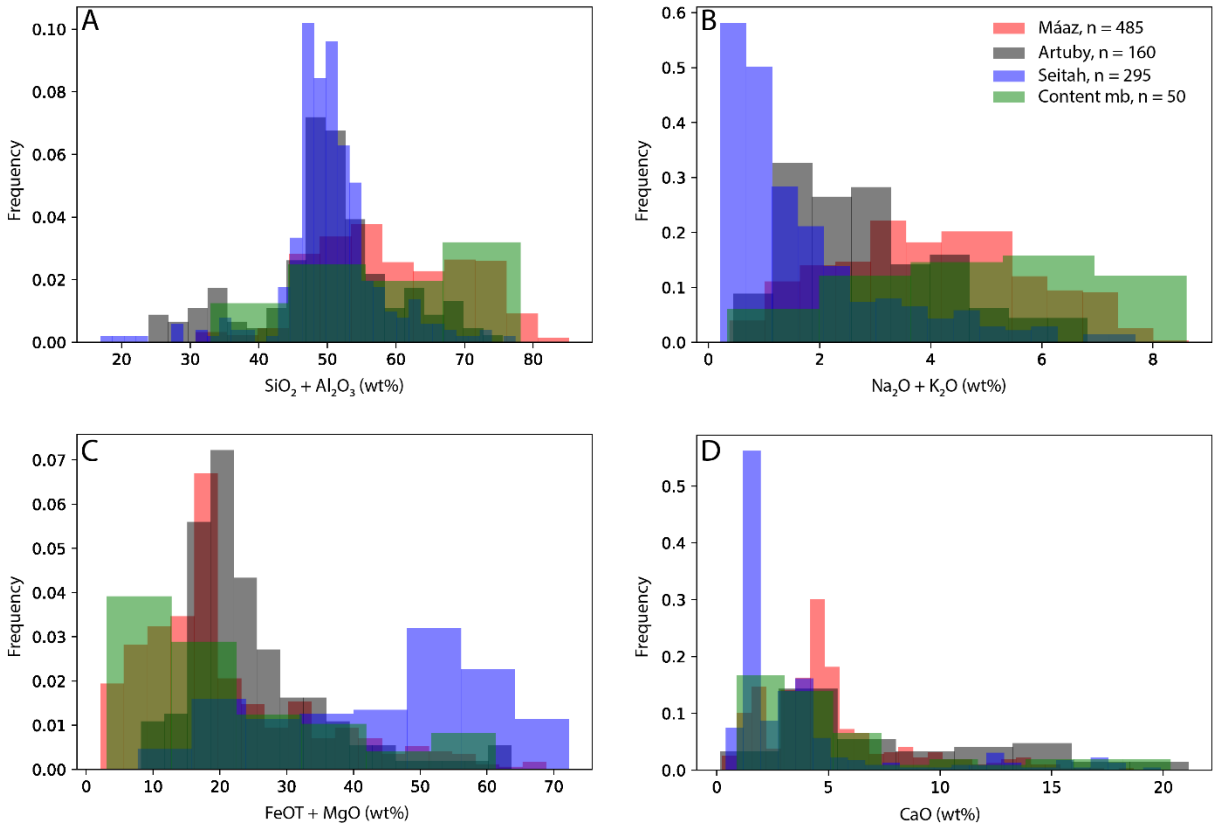

Fig. S4. Histograms of major element oxide distributions in the Máaz fm, Artuby ridge, and Séítah. (A) Distributions of SiO_2+Al_2O_3 in wt% from all data points. **(B)** Alkali wt% distributions. **(C)** Sum of MgO and FeO_T. **(D)** Distribution of CaO wt%. The y-axes represent the fraction of the total number of points that are in each bin. These are normalized so that the area under the curve is equal to one.

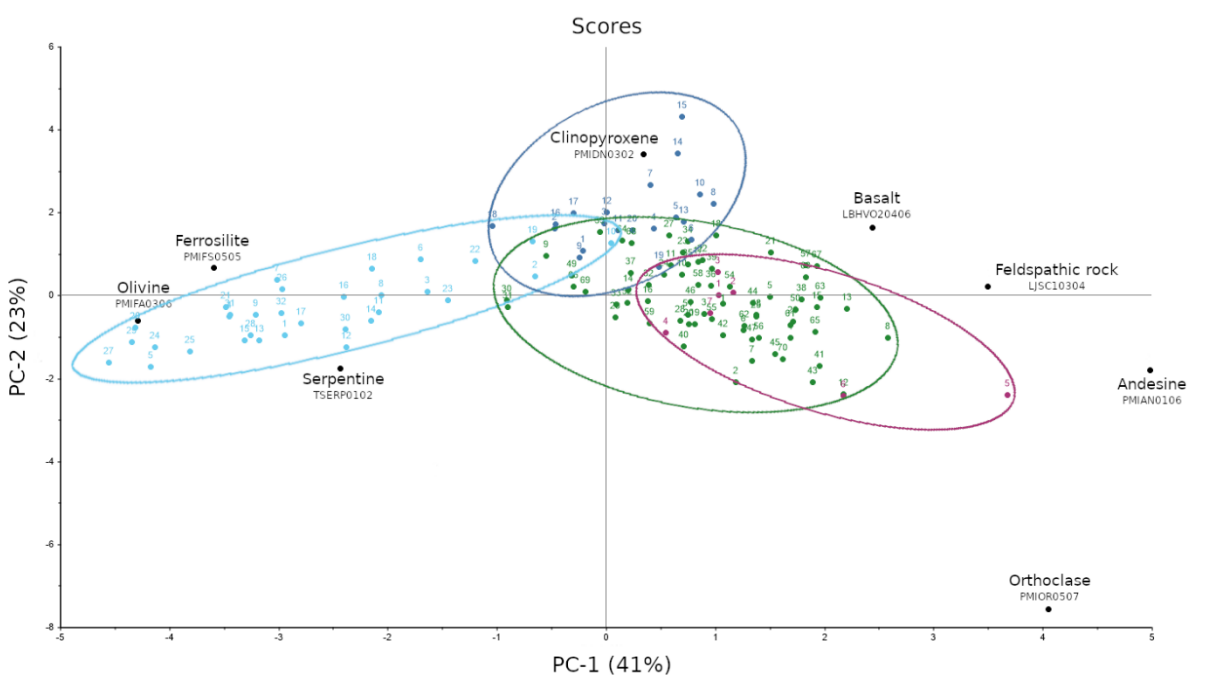

Fig. S5. Principal component analysis (PCA) of SuperCam LIBS target compositions. The first two principal components are plotted from a PCA analysis of LIBS major-element oxide (MOC) compositions averaged by target. Targets are numbered within each unit; correspondence between numbers and target names are given in Data File S3. Light blue represents the Séítah fm, dark blue represents Artuby ridge, green is for the Máaz fm, and fuchsia represents the Content mb. The ellipses are merely to guide the eye. The positions of several on-board calibration targets are shown in black and labeled.

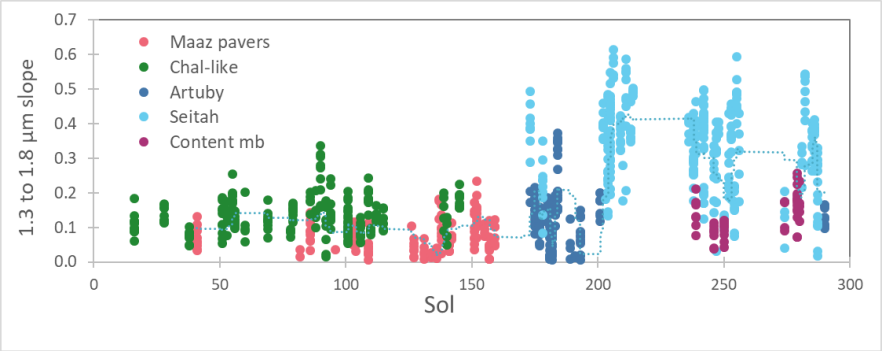

Fig. S6. **Spectral slopes from 1.3 to 1.8 µm, captured by the SuperCam IR spectrometer**. Strong slopes in this range are diagnostic of olivine, as noted in Séítah. Compare with the plot of MgO in Figs. 1C and S3.

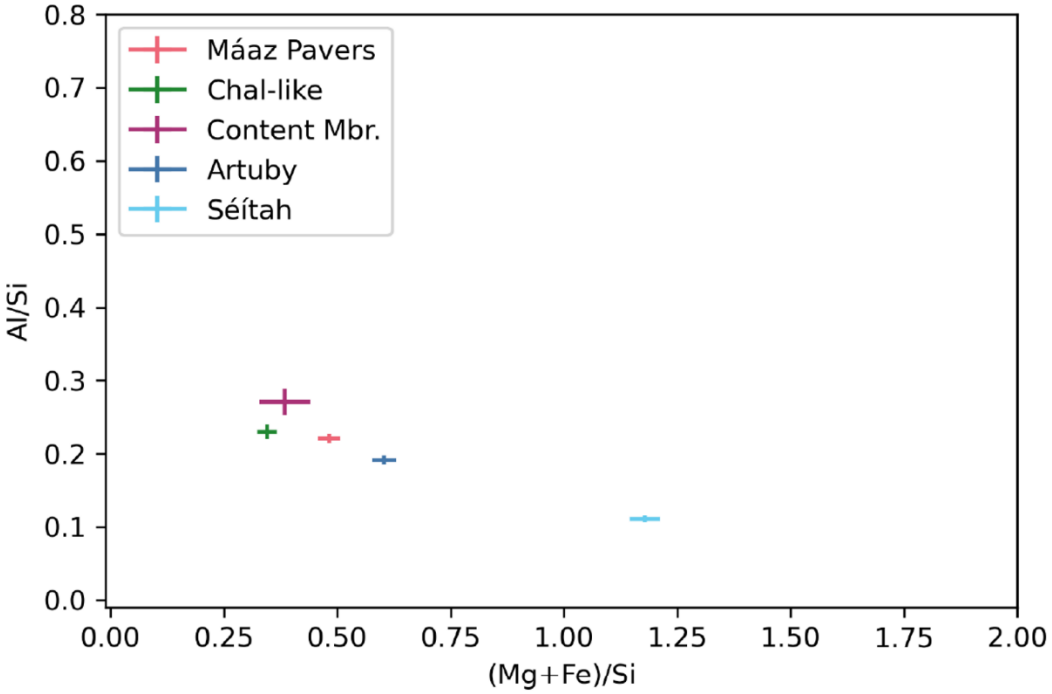

Fig. S7. Standard errors of the mean compositions plotted in Fig. 3. See Fig. 3A-B for reference.

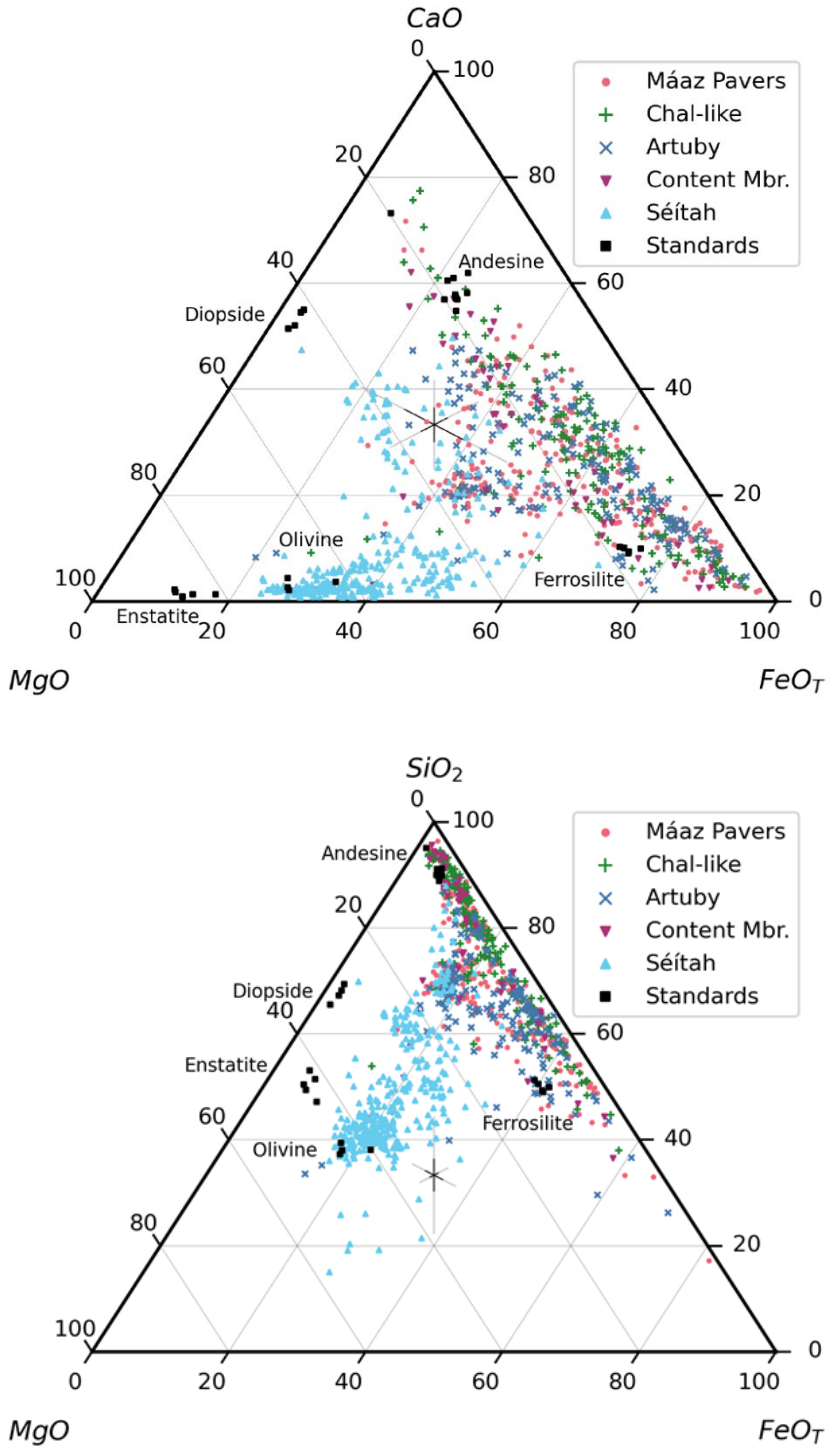

Fig. S8. CaO-MgO-FeO and SiO_2-MgO-FeO diagrams. These ternary diagrams show the relative molar abundances of Ca, Mg, Si, and Fe, indicating that all Máaz observations of mafic minerals, including at Artuby, are very iron-rich, while Séítah olivines and pyroxenes are distinctly different, both containing more Mg. Error bars indicate mean precision (dark lines) and accuracy (light lines).

Table S1.

Grain sizes of Séítah materials, in millimeters.

Target	Sol	N	Mean	St. Dev.	Mode
Issole[1]	202	141	1.13	0.19	1.10
Estoublaisse[1]	285	140	1.57	0.15	1.42
Bezaudun[1]	286	180	1.35	0.18	1.39
Sagnes[1]	291	115	1.00	0.20	0.83
Monier[2]	205	97	1.49	0.26	1.42
Mairola[2]	205	108	1.52	0.29	1.82
Cine[2]	206	95	1.57	0.28	1.72
Norante[2]	282	143	1.62	0.17	1.54
Brac[3]	247	117	1.62	0.20	1.60
Pierlas[3]	252	137	1.50	0.29	1.43
Ferres[3]	254	112	1.45	0.16	1.54
Ubraye[3]	255	126	1.58	0.18	1.42

1 = Issole region; 2 = Bastide region; 3 = Caille region; see Fig. S2.

Table S2.

Mean compositions of Máaz pavers and Ch'al-like rocks.

Mean wt%	SiO_2	TiO_2	Al_2O_3	FeO_T	MgO	CaO	Na_2O	K_2O	Total	N
Máaz Ch'al-like	52.6(.6)	0.47(.03)	10.3(.4)	16.6(1.0)	1.9(.1)	4.7(.2)	3.3(.1)	1.3(.1)	91.3	177
Máaz pavers	47.5(.5)	0.62(.03)	8.9(.3)	19.5(0.8)	3.1(.1)	5.5(.2)	2.7(.1)	0.9(.1)	88.8	268

Standard errors of the means are in parentheses

Table S3.

CIPW norms and calculated parameters derived from non-normalized abundances of the main observed units.

Weight %	Máaz	Artuby	Séítah
SiO_2	50.3	46.0	46.2
TiO_2	0.6	0.9	0.2
Al_2O_3	9.6	6.8	4.0
FeO_T	18.8	23.4	23.3
MgO	2.5	3.5	22.1
CaO	5.1	7.1	3.8
Na_2O	3.0	2.5	1.3
K_2O	1.1	0.5	0.2
Quartz	5.2	0.0	0.0
Plagioclase	34.9	27.0	15.5
Orthoclase	6.5	3.0	1.2
Diopside	4.7	16.4	3.2
Hypersthene	35.5	39.0	33.8
Olivine	0.0	0.2	43.6
Ilmenite	1.1	1.7	0.4
Magnetite	1.5	1.9	1.9
An # plagioclase	26.0	20.7	27.8
Mg #	19.1	21.0	62.9
Density (g/cc)	3.11	3.28	3.38

Elemental abundance totals are not normalized; assume Fe^{2+}/total Fe = 0.95.

Table S4.

Effect of iron oxidation state on CIPW norms (in wt%) and derived parameters for the range of $Fe^{2+}/\Sigma Fe$ = 0.9 and 1.0.

	Máaz fm		Artuby		Séítah	
$Fe^{2+}/\Sigma Fe$	0.90	1.0	0.90	1.0	0.90	1.0
Quartz	6.8	4.3	1.5	0.0	0.0	0.0
Plagioclase	37.9	37.9	29.2	29.2	15.2	15.2
Orthoclase	7.1	7.1	3.6	3.6	1.2	1.2
Diopside	4.8	4.8	17.4	17.5	1.5	1.6
Hypersthene	35.1	40.7	38.9	38.7	37.2	32.2
Olivine	0.0	0.0	0.0	5.3	36.9	45.3
Ilmenite	1.1	1.1	1.7	1.7	0.4	0.4
Magnetite	3.3	0.0	4.1	0.0	3.6	0.0
Apatite	4.2	4.2	4.2	4.2	4.2	4.2
An# plagioclase	25.3	25.3	20.6	20.6	26.5	26.5
Mg#	19.3	19.2	21.1	21.1	62.8	62.8
Density (g/cc)	3.09	3.10	3.27	3.28	3.38	3.37

Table S5.

SuperCam LIBS MOC accuracies propagated to CIPW norms (wt%) and parameters.

	Máaz	Artuby	Séítah
Quartz	±3.2	±2.9	±0.0
Plagioclase	±8.0	±5.1	±3.2
Orthoclase	±3.5	±3.6	±2.4
Diopside	±0.0	±3.7	±1.7
Hypersthene	±7.6	±3.9	±17.2
Olivine	±0.0	±7.2	±17.6
Ilmenite	±0.6	±0.6	±0.5
Magnetite	±0.3	±0.3	±0.3
An# plagioclase	±7.5	±0.8	±11.5
Mg#	±4.2	±2.9	±2.0

Table S6.
Image designations.

Figure Number	Target Name	Sol Number	Image Number	Instrument
Fig. 2A		46	ZR0_0046_0671038623_156ECM_N0031416ZCAM08011_034085J	Mastcam-Z
Fig. 2B	Peppermint	46	LRF_0046_0671037542_147EBY_N0031416SCAM05046_0010I6J to LRF_0046_0671037804_141EBY_N0031416SCAM05046_0030I6J	SuperCam
Fig. 2C		175	NLF_0175_0682484237_056ECM_N0061752NCAM00419_04_195J to NLF_0175_0682484615_116ECM_N0061752NCAM03175_04_195J	Navcam
Fig. 2D	Grasse	177	LRF_0177_0682649631_508EBY_N0061752SCAM01177_0100I6J	SuperCam
Fig. 2E		205	NLF_0205_0685144010_882EBY_N0071836NCAM01205_04_0LLJ to NRF_0205_0685144010_882EBY_N0071836NCAM01205_01_0LLJ	Navcam
Fig. 2F	Cine	206	LRF_0206_0685220408_265EBY_N0071836SCAM01206_0050I6J	SuperCam
Fig. 2G		238	NLF_0238_0688077582_521ECM_N0072326NCAM03238_10_195J to NLF_0238_0688077582_521ECM_N0072326NCAM03238_01_195J	
Fig. 2H	Content	239	LRF_0239_0688155183_382EBY_N0072326SCAM02239_0050I6J	SuperCam
Fig. S1A		139	ZR0_0139_0679280525_956EBY_N0051812ZCAM08148_1100LMJ	Mastcam-Z
Fig. S1B-D	Mirabeau	139	LRF_0139_0679278019_466EBY_N0051812SCAM01139_0010I6J to LRF_0139_0679279930_232EBY_N0051812SCAM01139_0100I6J	SuperCam
Fig. S1E		86	ZR0_0086_0674575422_936EBY_N0040000ZCAM03136_1100LUJ	Mastcam-Z
Fig. S1F	Hoolhnili	86	LRF_0086_0674572608_242EBY_N0040000SCAM04086_0050I6J	SuperCam
Fig. S1G		130	ZR0_0130_0678477023_473EBY_N0042222ZCAM03175_1100LMJ	Mastcam-Z
Fig. S1H	Raton	130	LRF_0130_0678473978_180EBY_N0042222SCAM01130_0010I6J to LRF_0130_0678475861_269EBY_N0042222SCAM01130_0100I6J	SuperCam

Data S1. Major-Element Oxide Compositions. Compositions of LIBS observation points in Máaz pavers, Máaz Ch'al-like rocks, Artuby ridge rocks, Séítah fm, and Content mb rocks.

Data S2. IR 1.3-1.8 µm slopes. The slopes of IR spectra observed throughout the traverse are plotted vs. sol # in Fig. S6. The data are provided in file Data S2.

Data S3. Target Numbering for Fig. S5. This data table provides the corresponding target name for each target number in Fig. S5.

Reference S1. References for meteorite data in Fig. 5B.

REFERENCES AND NOTES

1. J. A. Grant, M. P. Golombek, S. A. Wilson, K. A. Farley, K. H. Williford, A. Chen, The science process for selecting the landing site for the 2020 Mars rover. *Planet. Space Sci.* **164**, 106–126 (2018).

2. C. I. Fassett, J. W. Head III, Fluvial sedimentary deposits on Mars: Ancient deltas in a crater lake in the Nili Fossae region. *Geophys. Res. Lett.* **32**, L14201 (2005).

3. N. Mangold, S. Gupta, O. Gasnault, G. Dromart, J. D. Tarnas, S. F. Sholes, B. Horgan, C. Quantin-Nataf, A. J. Brown, S. Le Mouelic, R. A. Yingst, J. F. Bell, O. Beyssac, T. Bosak, F. Calef III, B. L. Ehlmann, K. A. Farley, J. P. Grotzinger, K. Hickman-Lewis, S. Holm-Alwmark, L. C. Kah, J. Martinez-Frias, S. M. McLennan, S. Maurice, J. I. Nunez, A. M. Ollila, P. Pilleri, J. W. Rice Jr., M. Rice, J. I. Simon, D. L. Shuster, K. M. Stack, V. Z. Sun, A. H. Treiman, B. P. Wiess, R. C. Wiens, A. J. Williams, N. R. Williams, K. H. Williford, Perseverance rover reveals an ancient delta-lake system and flood deposits at Jezero crater, Mars. *Science* 374, 711–717 (2021).

4. B. L. Ehlmann, J. F. Mustard, S. L. Murchie, F. Poulet, J. L. Bishop, A. J. Brown, W. M. Calvin, R. N. Clark, D. J. Des Marais, R. E. Milliken, L. H. Roach, T. L. Roush, G. A. Swayze, J. J. Wray, Orbital identification of carbonate-bearing rocks on Mars. *Science* **322**, 1828–1832 (2008).

5. B. L. Ehlmann, J. F. Mustard, G. A. Swayze, R. N. Clark, J. L. Bishop, F. Poulet, D. J. Des Marais, L. H. Roach, R. E. Milliken, J. J. Wray, O. Barnouin-Jha, S. L. Murchie, Identification of hydrated silicate minerals on Mars using MRO-CRISM: Geologic context near Nili Fossae and implications for aqueous alteration. *J. Geophys. Res.* **114**, E00D08 (2009).

6. A. J. Brown, S. J. Hook, A. M. Baldridge, J. K. Crowley, N. T. Bridges, B. J. Thomson, G. M. Marion, C. R. de Souza Filho, J. L. Bishop, Hydrothermal formation of clay-carbonate alteration assemblages in the Nili Fossae region of Mars. *Earth Planet. Sci. Lett.* **297**, 174–82 (2010).

7. T. A. Goudge, J. F. Mustard, J. W. Head, C. I. Fassett, S. M. Wiseman, Assessing the mineralogy of the watershed and fan deposits of the Jezero crater paleolake system, Mars. *J. Geophys. Res. Planets* **120**, 775–808 (2015).

8. B. H. N. Horgan, R. B. Anderson, G. Dromart, E. S. Amador, M. S. Rice, The mineral diversity of Jezero crater: Evidence for possible lacustrine carbonates on Mars. *Icarus* **339**, 113526 (2020).

9. A. M. Zastrow, T. D. Glotch, Distinct carbonate lithologies in Jezero crater, Mars. *Geophys. Res. Lett.* **48**, e2020GL092365 (2021).

10. J. D. Tarnas, K. M. Stack, M. Parente, A. H. D. Koeppel, J. F. Mustard, K. R. Moore, B. H. N. Horgan, F. P. Seelos, E. A. Cloutis, P. B. Kelemen, D. Flannery, A. J. Brown, K. R. Frizzell, P. Pinet, Characteristics, origins, and biosignature preservation potential of carbonate-bearing rocks within and outside of Jezero crater. *J. Geophys. Res. Planets* **126**, e2021JE006898 (2021).

11. J. B. Pollack, J. F. Kasting, S. M. Richardson, K. Poliakoff, The case for a wet, warm climate on early Mars, *Icarus* **71**, 203–224 (1987).

12. T. A. Goudge, J. F. Mustard, J. W. Head, C. I. Fassett, Constraints on the history of open-basin lakes on Mars from the composition and timing of volcanic resurfacing. *J. Geophys. Res. Planets* **117**, E00J21 (2012).

13. T. A. Goudge, R. E. Milliken, J. W. Head, J. F. Mustard, C. I. Fassett, Sedimentological evidence for a deltaic origin of the western fan deposit in Jezero crater, Mars and implications for future exploration, *Earth Planet. Sci. Lett.* **458**, 357–365 (2017).

14. S. Shahrzad, K. M. Kinch, T. A. Goudge, C. I. Fassett, D. H. Needham, C. Quantin-Nataf, C. P. Knudsen, Crater statistics on the dark-toned, mafic floor unit in Jezero crater, Mars, *Geophys. Res. Lett.* **46**, 2408–2416 (2019).

15. K. M. Stack, N. R. Williams, F. Calef III, V. Z. Sun, K. H. Williford, K. A. Farley, S. Eide, D. Flannery, C. Hughes, S. R. Jacob, L. C. Kah, F. Meyen, A. Molina, C. Quantin-Nataf, M. Rice, P. Russell, E. Scheller, C. H. Seeger, W. J. Abbey, J. B. Adler, H. Amundsen, R. B. Anderson, S. M. Angel, G. Arana, J. Atkins, M. Barrington, T. Berger, R. Borden, B. Boring, A. Brown, B. L. Carrier, P. Conrad, H. Dypvik, S. A. Fagents, Z. E. Gallegos, B. Garczynski, K. Golder, F. Gomez, Y. Goreva, S. Gupta, S.-E. Hamran, T. Hicks, E. D. Hinterman, B. N. Horgan, J. Hurowitz, J. R. Johnson, J. Lasue, R. E. Kronyak, Y. Liu, J. M. Madariaga, N. Mangold, J. McClean, N. Miklusicak,

D. Nunes, C. Rojas, K. Runyon, N. Schmitz, N. Scudder, E. Shaver, J. SooHoo, R. Spaulding, E. Stanish, L. K. Tamppari, M. M. Tice, N. Turenne, P. A. Willis, R. A. Yingst, Photogeologic map of the Perseverance rover field site in jezero crater constructed by the Mars 2020 Science team. *Space Sci. Rev.* **216**, 217 (2020).

16. V. Z. Sun, K. M. Stack, Geologic Map of Jezero Crater and the Nili Planum Region, Mars, USGS Scientific Investigations Map 3464 (2020); https://doi.org/10.3133/sim3464.

17. S. Holm-Alwmark, K. M. Kinch, M. D. Hansen, S. Shahrzad, K. Svennevig, W. J. Abbey, R. B. Anderson, F. J. Calef III, S. Gupta, E. Hauber, B. H. N. Horgan, L. C. Kah, J. Knade, N. B. Miklusicak, K. M. Stack, V. Z. Sun, J. D. Tarnas, C. Quantin-Nataf, Stratigraphic relationships in Jezero crater, Mars: Constraints on the timing of fluvial-lacustrine activity from orbital observations. *J. Geophys. Res. Planets* **126**, e2021JE006840 (2021).

18. J. F. Mustard, M. Adler, A. Allwood, D. S. Bass, D. W. Beaty, J. F. Bell III, W. B. Brinckerhoff, M. Carr, D. J. Des Marais, B. Drake, K. S. Edgett, J. Eigenbrode, L. T. Elkins-Tanton, J. A. Grant, S. M. Milkovich, D. Ming, C. Moore, S. Murchie, T. C. Onstott, S. W. Ruff, M. A. Sephton, A. Steele, A. Treiman, "Report of the Mars 2020 Science Definition Team" (Mars Exploration Program Analysis Group, 2013), 154 pp; http://mepag.jpl.nasa.gov/reports/MEP/Mars_2020_SDT_Report_Final.pdf.

19. D. W. Beaty, M. M. Grady, H. Y. McSween, E. Sefton-Nash, B. L. Carrier, F. Altieri, Y. Amelin, E. Ammannito, M. Anand, L. G. Benning, J. L. Bishop, L. E. Borg, D. Boucher, J. R. Brucato, H. Busemann, K. A. Campbell, A. D. Czaja, V. Debaille, D. J. Des Marais, M. Dixon, B. L. Ehlmann, J. D. Farmer, D. C. Fernandez-Remolar, J. Filiberto, J. Fogarty, D. P. Glavin, Y. S. Goreva, L. J. Hallis, A. D. Harrington, E. M. Hausrath, C. D. K. Herd, B. Horgan, M. Humayun, T. Kleine, J. Kleinhenz, R. Mackelprang, N. Mangold, L. E. Mayhew, J. T. McCoy, F. M. McCubbin, S. M. McLennan, D. E. Moser, F. Moynier, J. F. Mustard, P. B. Niles, G. G. Ori, F. Raulin, P. Rettberg, M. A. Rucker, N. Schmitz, S. P. Schwenzer, M. A. Sephton, R. Shaheen, Z. D. Sharp, D. L. Shuster, S. Siljeström, C. L. Smith, J. A. Spry, A. Steele, T. D. Swindle, I. L. ten Kate, N. J. Tosca, T. Usui, M. J. Van Kranendonk, M. Wadhwa, B. P. Weiss, S. C. Werner, F. Westall, R. M. Wheeler, J. Zipfel, M. P. Zorzano, The potential science and engineering value of samples delivered to Earth by Mars sample

return: International MSR Objectives and Samples Team (iMOST). *Meteorit Planet. Sci.* **54**, S3-S152 (2019).

20. S. C. Schon, J. W. Head, C. I. Fassett, An overfilled lacustrine system and progradational delta in Jezero crater, Mars: Implications for Noachian climate, *Planet. Spa. Sci.* **67**, 28–45 (2012).

21. R. C. Wiens, S. Maurice, S. H. Robinson, A. E. Nelson, P. Cais, P. Bernardi, R. T. Newell, S. Clegg, S. K. Sharma, S. Storms, J. Deming, D. Beckman, A. M. Ollila, O. Gasnault, R. B. Anderson, Y. André, S. Michael Angel, G. Arana, E. Auden, P. Beck, J. Becker, K. Benzerara, S. Bernard, O. Beyssac, L. Borges, B. Bousquet, K. Boyd, M. Carey, J. Carlson, K. Castro, J. Celis, B. Chide, K. Clark, E. Cloutis, E. C. Cordoba, A. Cousin, M. Dale, L. Deflores, D. Delapp, M. Deleuze, M. Dirmyer, C. Donny, G. Dromart, M. G. Duran, M. Egan, J. Ervin, C. Fabre, A. Fau, W. Fischer, O. Forni, T. Fouchet, R. Fresquez, J. Frydenvang, D. Gasway, I. Gontijo, J. Grotzinger, X. Jacob, S. Jacquinod, J. R. Johnson, R. A. Klisiewicz, J. Lake, N. Lanza, J. Laserna, J. Lasue, S. Le Mouelic, C. Legett, R. Leveille, E. Lewin, G. Lopez-Reyes, R. Lorenz, E. Lorigny, S. P. Love, B. Lucero, J. M. Madariaga, M. Madsen, S. Madsen, N. Mangold, J. A. Manrique, J. P. Martinez, J. Martinez-Frias, K. P. McCabe, T. H. McConnochie, J. M. McGlown, S. M. McLennan, N. Melikechi, P.-Y. Meslin, J. M. Michel, D. Mimoun, A. Misra, G. Montagnac, F. Montmessin, V. Mousset, N. Murdoch, H. Newsom, L. A. Ott, Z. R. Ousnamer, L. Pares, Y. Parot, R. Pawluczyk, C. Glen Peterson, P. Pilleri, P. Pinet, G. Pont, F. Poulet, C. Provost, B. Quertier, H. Quinn, W. Rapin, J.-M. Reess, A. H. Regan, A. L. Reyes-Newell, P. J. Romano, C. Royer, F. Rull, B. Sandoval, J. H. Sarrao, V. Sautter, M. J. Schoppers, S. Schroeder, D. Seitz, T. Shepherd, P. Sobron, B. Dubois, V. Sridhar, M. J. Toplis, I. Torre-Fdez, I. A. Trettel, M. Underwood, A. Valdez, J. Valdez, D. Venhaus, P. Willis, The SuperCam instrument suite on the NASA Mars 2020 rover: Body unit and combined system tests. *Space Sci. Rev.* **217**, 4 (2021).

22. S. Maurice, R. C. Wiens, P. Bernardi, P. Cais, S. Robinson, T. Nelson, O. Gasnault, J. M. Reess, M. Deleuze, F. Rull, J. A. Manrique, S. Abbaki, R. B. Anderson, Y. Andre, S. M. Angel, G. Arana, T. Battault, P. Beck, K. Benzerara, S. Bernard, J. P. Berthias, O. Beyssac, M. Bonafous, B. Bousquet, M. Boutillier, A. Cadu, K. Castro, F. Chapron, B. Chide, K. Clark, E. Clavé, S. Clegg, E. Cloutis, C. Collin, E. C. Cordoba, A. Cousin, J. C. Dameury, W. D'Anna, Y. Daydou, A. Debus, L. Deflores, E. Dehouck, D. Delapp, G. De Los Santos, C. Donny, A. Doressoundiram, G. Dromart, B. Dubois, A.

Dufour, M. Dupieux, M. Egan, J. Ervin, C. Fabre, A. Fau, W. Fischer, O. Forni, T. Fouchet, J. Frydenvang, S. Gauffre, M. Gauthier, V. Gharakanian, O. Gilard, I. Gontijo, R. Gonzalez, D. Granena, J. Grotzinger, R. Hassen-Khodja, M. Heim, Y. Hello, G. Hervet, O. Humeau, X. Jacob, S. Jacquinod, J. R. Johnson, D. Kouach, G. Lacombe, N. Lanza, L. Lapauw, J. Laserna, J. Lasue, L. Le Deit, S. Le Mouelic, E. Le Comte, Q. M. Lee, C. Legett, R. Leveille, E. Lewin, C. Leyrat, G. Lopez-Reyes, R. Lorenz, B. Lucero, J. M. Madariaga, S. Madsen, M. Madsen, N. Mangold, F. Manni, J. F. Mariscal, J. Martinez-Frias, K. Mathieu, R. Mathon, K. P. McCabe, T. McConnochie, S. M. McLennan, J. Mekki, N. Melikechi, P. Y. Meslin, Y. Micheau, Y. Michel, J. M. Michel, D. Mimoun, A. Misra, G. Montagnac, C. Montaron, F. Montmessin, J. Moros, V. Mousset, Y. Morizet, N. Murdoch, R. T. Newell, H. Newsom, N. Nguyen Tuong, A. M. Ollila, G. Orttner, L. Oudda, L. Pares, J. Parisot, Y. Parot, R. Perez, D. Pheav, L. Picot, P. Pilleri, C. Pilorget, P. Pinet, G. Pont, F. Poulet, C. Quantin-Nataf, B. Quertier, D. Rambaud, W. Rapin, P. Romano, L. Roucayrol, C. Royer, M. Ruellan, B. F. Sandoval, V. Sautter, M. J. Schoppers, S. Schroeder, H. C. Seran, S. K. Sharma, P. Sobron, M. Sodki, A. Sournac, V. Sridhar, D. Standarovsky, S. Storms, N. Striebig, M. Tatat, M. Toplis, I. Torre-Fdez, N. Toulemont, C. Velasco, M. Veneranda, D. Venhaus, C. Virmontois, M. Viso, P. Willis, K. W. Wong, The SuperCam instrument suite on the Mars 2020 rover: Science objectives and mast-unit description. *Space Sci. Rev.* **217**, 47 (2021).

23. T. Fouchet, J.-M. Reess, F. Montmessin, R. Hassen-Khodja, N. Nguyen-Tuong, O. Humeau, S. Jacquinod, L. Lapauw, J. Parisot, M. Bonafous, P. Bernardi, F. Chapron, A. Jeanneau, C. Collin, D. Zeganadin, P. Nibert, S. Abbaki, C. Montaron, C. Blanchard, V. Arslanyan, O. Achelhi, C. Colon, C. Royer, V. Hamm, M. Beuzit, F. Poulet, C. Pilorget, L. Mandon, O. Forni, A. Cousin, O. Gasnault, P. Pilleri, B. Dubois, C. Quantin, P. Beck, O. Beyssac, S. Le Mouelic, J. R. Johnson, T. H. McConnochie, S. Maurice, R. C. Wiens, The SuperCam infrared spectrometer for the Perseverance rover of the Mars 2020 mission. *Icarus* **373**, 114773 (2022).

24. K. A. Farley, K. M. Stack, B. H. N. Horgan, J. Tarnas, V. Z. Sun, D. L. Shuster, J. I. Simon, J. A. Hurowitz, K. R. Moore, E. L. Scheller, M. E. Schmidt, T. V. Kizovski, P. S. Russell, P. Vasconcelos, N. J. Tosca, O. Beyssac, T. Bosak, B. L. Ehlmann, L. E. Mayhew, S. M. McLennan, A. H. Treiman, R. C. Wiens, K. H. Williford, *et al.*, Aqueously altered igneous rocks on the floor of Jezero crater, Mars. *Science*, submitted (2022).

25. S.-E. Hamran, D. A. Paige, H. E. F. Amundsen, T. Berger, Sverre Brovoll, L. Carter, T. Casademont, L. Damsgard, H. Dypvik, S. Eide, R. Ghent, J. Kohler, M. Mellon, D. C. Nunes, D. Plettemeier, P. Russell, M. Siegler, M. J. Oyan, Ground penetrating radar observations of subsurface structures in the floor of Jezero crater, Mars. *Sci. Adv.* **8**, abp8564 (2022).

26. J. Bell *et al*., Geological and meteorological imaging results from the Mars 2020 Perseverance rover in Jezero crater. *Sci. Adv.* **8**, abo4856 (2022).

27. H. W. Nesbitt, R. E. Wilson, Recent chemical weathering of basalts. *Am. J. Sci.*, **292**, 740–777 (1992).

28. E. B. Rampe, D. F. Blake, T. F. Bristow, D. W. Ming, D. T. Vaniman, R. V. Morris, C. N. Achilles, S. J. Chipera, S. M. Morrison, V. M. Tu, A. S. Yen, N. Castle, G. W. Downs, R. T. Downs, J. P. Grotzinger, R. M. Hazen, A. H. Treiman, T. S. Peretyazhko, D. J. Des Marais, R. C. Walroth, P. I. Craig, J. A. Crisp, B. Lafuente, J. M. Morookain, P. C. Sarrazin, M. T. Thorpe, J. C. Bridges, L. A. Edgar, C. M. Fedo, C. Freissinet, R. Gellert, P. R. Mahaffy, H. E. Newsom, J. R. Johnson, L. C. Kah, K. L. Siebach, J. Schieber, V. Z. Sun, A. R. Vasavada, D. Wellington, R. C. Wiens; MSL Science Team, Mineralogy and geochemistry of sedimentary rocks and eolian sediments in Gale crater, Mars: A review after six Earth years of exploration with Curiosity. *Geochemistry* **80**, 125605 (2020).

29. Y. Liu, M. M. Tice, M. E. Schmidt, A. H. Treiman, T. V. Kizovski, J. A. Hurowitz, A. C. Allwood, J. Henneke, D. A. K. Pedersen, S. J. VanBommel, M. W. M. Jones, A. L. Knight, B. J. Orenstein, B. C. Clark, W. T. Elam, C. M. Heirwegh, *et al.*, An olivine cumulate outcrop on the floor of Jezero crater, Mars. *Science*, in press (2022).

30. A. J. Brown, C. E. Viviano, T. A. Goudge, Olivine-carbonate mineralogy of the Jezero Crater region. *J. Geophys. Res. Planets* **125**, e2019JE006011 (2020).

31. J. Filiberto, R. Dasgupta, Fe2+-Mg partitioning between olivine and basaltic melts: Applications to genesis of olivine-phyric shergottites and conditions of melting in the martian interior. *Earth Planet. Sci. Lett.* **304**, 527–537 (2011).

32. N. H. Sleep, B. F. Windley, Archean plate tectonics: Constraints and inferences. *J. Geol.* **90**, 363–379 (1982).

33. O. Namur, B. Abily, G. Ceuleneer, A. E. Boudreau, F. Blanchette, J. W. M. Bush, B. Charlier, J.-C. Duchesne, M. D. Higgins, D. Morata, T. F. D. Nielson, B. O'driscoll, K. N. Pang, T. Peacock, C. J. Spandler, A. Toramaru, I. V. Veksler, Igneous layering in basaltic magma chambers, in *Layered Intrusions*, B. Charlier, O. Naur, R. Latypov, C. Tegner, Eds. (Springer, 2015), pp. 75–152.

34. M. W. Schmidt, M. Forien, G. Solferino, N. Bagdassarov, Settling and compaction of olivine in basaltic magmas: An experimental study on the time scales of cumulate formation. *Contrib. Mineral. Petrol.* **164**, 959–976 (2012).

35. C. Paola, S. M. Wiele, M. A. Reinhart, Upper-regime parallel lamination as the result of turbulent sediment transport and low-amplitude bed forms. *Sedimentology* **36**, 47–59 (1989).

36. J. Bridge, J. Best, Preservation of planar laminae due to migration of low-relief bed waves over aggrading upper-stage plane beds: Comparison of experimental data with theory. *Sedimentology* **44**, 253–262 (1997).

37. D. A. V. Stow, M. Johansson, Deep-water massive sands: Nature, origin, and hydrocarbon implications, *Mar. Pet. Geol.* **17**, 145–174 (2000).

38. P. E. Potter, A. E. Scheidegger, Bed thickness and grain size: Graded beds. *Sedimentology* **7**, 233–240 (1966).

39. F. Felletti, R. Bersezio, Validation of Hurst statistics: A predictive tool to discriminate turbiditic sub-environments in a confined basin. *Pet. Geosci.* **16**, 401–412 (2010).

40. C. H. Kremer, M. S. Bramble, J. F. Mustard, Origin and emplacement of the circum-Isidis olivine-rich unit. *Lunar Planet. Sci.* **49**, 1545 (2018).

41. L. Mandon, C. Quantin-Nataf, P. Thollot, N. Mangold, L. Lozac'h, G. Dromart, P. Beck, E. Dehouck, S. Breton, C. Millot, M. Volat, Refining the age, emplacement and alteration scenarios of the olivine-rich unit in the Nili Fossae region, Mars. *Icarus* **336**, 113436 (2020).

42. N. A. Stroncik, H.-U. Schmincke, Evolution of palagonite: Crystallization, chemical changes, and element budget. *Geochem. Geophys. Geosyst.* **2**, 2000GC000102 (2001).

43. J. H. J. Bedard, The development of compositional and textural layering in Archaean komatiites and in Proterozoic komatiitic basalts from Cape Smith, Quebec, Canada, in *Origins of Igneous Layering*, I. Parsons, Ed. (D. Reidel, 1987) pp. 399–418.

44. C. D. K. Herd, Reconciling redox: Making spatial and temporal sense of oxygen fugacity variations in martian igneous rocks. *Lunar Planet. Sci.* **50**, 2746 (2019).

45. T. J. Lapen, M. Righter, R. Andreasen, A. J. Irving, A. M. Satkoski, B. L. Beard, K. Nishiizumi, A. J. T. Jull, M. W. Caffee Two billion years of magmatism recorded from a single Mars meteorite ejection site. *Sci. Adv.* **3**, e1600922 (2017).

46. A. Udry, J. M. D. Day, 1.34 billion-year-old magmatism on Mars evaluated from the co-genetic nakhlite and chassignite meteorites. *Geochim. Cosmochim. Acta* **238**, 292–315 (2018).

47. A. Udry, G. H. Howarth, T. J. Lapen, M. Righter, Petrogenesis of the NWA 7320 enriched martian gabbroic shergottite: Insight into the martian crust. *Geochim. Cosmochim. Acta* **204**, 1–18 (2017).

48. D. Xirouchakis, D. S. Draper, C. S. Schwandt, A. Lanzirotti, Crystallization conditions of Los Angeles, a basaltic Martian meteorite, *Geochim. Cosmochim. Acta* **66**, 1867–1880 (2002).

49. A. R. Santos, C. B. Agee, F. M. McCubbin, C. K. Shearer, P. V. Burger, R. Tartèse, M. Anand, Petrology of igneous clasts in Northwest Africa 7034: Implications for the petrologic diversity of the martian crust. *Geochim. Cosmochim. Acta* **157**, 56–85 (2015).

50. A. Udry, G. H. Howarth, C. Herd, J. M. D. Day, T. J. Lapen, J. Filiberto, What martian meteorites reveal about the interior and surface of Mars. *J. Geophys. Res. Planets* **55**, e2020JE006523 (2020).

51. R. R. Rahib, A. Udry, G. H. Howarth, J. Gross, M. Paquet, L. M. Combs, D. L. Laczniak, J. M. D. Day Mantle source to near-surface emplacement of enriched and intermediate poikilitic shergottites in Mars. *Geochim. Cosmochim. Acta* **266**, 463–496 (2019).

52. P. Pinet, S. Chevrel, Spectral identification of geological units on the surface of Mars related to the presence of silicates from Earth-based near-infrared telescopic charge-coupled device imaging. *J. Geophys. Res.* **95**, 14435–14446 (1990).

53. J. C. Bridges, L. J. Hicks, A. H. Treiman, Chapter 5 - Carbonates on Mars, in *Volatiles in the Martian Crust*, J. Filiberto, S. P. Schwenzer, Eds. (Elsevier, 2019) pp. 89–118.

54. A. Steele, L. G. Benning, R. Wirth, A. Schreiber, T. Araki, F. M. McCubbin, M. D. Fries, L. R. Nittler, J. Wang, L. J. Hallis, P. G. Conrad, C. Conley, S. Vitale, A. C. O'Brien, V. Riggi, K. Rogers, Organic synthesis associated with serpentinization and carbonation on early Mars. *Science* **375**, 172–177 (2022).

55. W. C. Koeppen, V. E. Hamilton, Global distribution, composition, and abundance of olivine on the surface of Mars from thermal infrared data. *J. Geophys. Res.* **113**, E05001 (2008).

56. A. Ody, F. Poulet, J.-P. Bibring, D. Loizeau, J. Carter, B. Gondet, Y. Langevin, Global investigation of olivine on Mars: Insights into crust and mantle compositions. *J. Geophys. Res. Planets* **118**, 234–262 (2013).

57. A. D. Rogers, N. H. Warner, M. P. Golombek, J. W. Head III, J. C. Cowart, Areally extensive surface bedrock exposures on Mars: Many are clastic rocks, not lavas. *Geophys. Res. Lett.* **45**, 1767–1777 (2018).

58. J. F. Mustard, F. Poulet, J. W. Head, N. Mangold, J.-P. Bibring, S. M. Pelkey, C. I. Fassett, Y. Langevin, G. Neukum, Mineralogy of the Nili Fossae region with OMEGA/Mars Express data: 1. Ancient impact melt in the Isidis Basin and implications for the transition from the Noachian to Hesperian. *J. Geophys. Res.* **112**, E08S03 (2007).

59. L. Richan, H. L. Gibson, M. G. Houlé, C. M. Lesher, Mode of emplacement of Archean komatiitic tuffs and flows in the Selkirk Bay area, Melville Peninsula, Nunavut, Canada, *Precambrian Res.* **263**, 174–196 (2015).

60. M. S. Bramble, J. F. Mustard, M. R. Salvatore, The geological history of Northeast Syrtis Major, Mars, *Mars. Icarus* **293**, 66–93 (2017).

61. J. A. Manrique, G. Lopez-Reyes, A. Cousin, F. Rull, F. S. Maurice, R. C. Wiens, M. B. Madsen, J. M. Madariaga, O. Gasnault, J. Aramendia, G. Arana, P. Beck, S. Bernard, P. Bernardi, M. H. Bernt, A. Berrocal, O. Beyssac, P. Cais, C. Castro, K. Castro, S. M. Clegg, E. Cloutis, G. Dromart, C. Drouet, B. Dubois, D. Escribano, C. Fabre, A. Fernandez, O. Forni, V. Garcia-Baonza, I. Gontijo, J. Johnson, J. Laserna, J. Lasue, S. Madsen, E. Mateo-Marti, J. Medina, P.-Y. Meslin, G. Montagnac, A. Moral, J. Moros, A. M. Ollila, C. Ortega, O. Prieto-Ballesteros, J. M. Reess, S. Robinson, J. Rodriguez, J. Saiz, J. A. Sanz-Arranz, I. Sard, V. Sautter, P. Sobron, M. Toplis, M. Veneranda, SuperCam calibration targets: Design and development. *Space Sci. Rev.* **216**, 138 (2020).

62. R. B. Anderson, O. Forni, A. Cousin, R. C. Wiens, S. M. Clegg, J. Frydenvang, T. S. J. Gabriel, A. Ollila, S. Schroeder, O. Beyssac, E. Gibbons, D. S. Vogt, E. Clavé, J.-A. Manrique, C. Legett IV, P. Pilleri, R. T. Newell, J. Sarrao, S. Maurice, G. Arana, K. Benzerara, P. Bernardi, S. Bernard, B. Bousquet, A. J. Brown, C. Alverez-Llamas, B. Chide, E. Cloutis, J. Comellas, S. Connell, E. Dehouck, D. M. Delapp, A. Essunfeld, C. Fabre, T. Fouchet, C. Garcia-Florentino, L. Garcia-Gomez, P. Gasda, O. Gasnault, E. Hausrath, N. L. Lanza, J. Laserna, J. Lasue, G. Lopez, J. M. Madariaga, L. Mandon, N. Mangold, P.-Y. Meslin, M. Nachon, A. E. Nelson, H. Newsom, A. L. Reyes-Newell, S. Robinson, F. Rull, S. Sharma, J. I. Simon, P. Sobron, I. Torre Fernandez, A. Udry, D. Venhaus, S. M. McLennan, R. V. Morris, B. Ehlmann, Post-landing major element quantification using SuperCam laser induced breakdown spectroscopy. *Spectrochim. Acta Part B At. Spectrosc.* **188**, 106347 (2022).

63. A. Cousin, V. Sautter, C. Fabre, G. Dromart, G. Montagnac, C. Drouet, P.-Y. Meslin, O. Gasnault, O. Beyssac, S. Bernard, E. Cloutis, O. Forni, P. Beck, T. Fouchet, J. R. Johnson, J. Lasue, A. M. Ollila, P. De Parseval, S. Gouy, B. Caron, J. M. Madariaga, G. Arana, M. B. Madsen, J. Laserna, J. Moros, J. A. Manrique, G. Lopez-Reyes, F. Rull, S. Maurice, R. C. Wiens, SuperCam calibration targets on board the Perseverance rover: Fabrication and quantitative characterization. *Spectrochim. Acta Part B At. Spectrosc.* **188**, 106341 (2021).

64. V. Payré, K. L. Siebach, R. Dasgupta, A. Udry, E. B. Rampe, S. M. Morrison, Constraining ancient magmatic evolution on Mars using crystal chemistry of detrital igneous minerals in the sedimentary Bradbury group, Gale crater, Mars. *J. Geophys. Res. Planets* **125**, e2020JE006467 (2020).

65. C. Legett IV, R. T. Newell, A. L. Reyes-Newell, A. E. Nelson, P. Bernardi, S. C. Bener, O. Forni, D. M. Venhaus, S. M. Clegg, A. M. Ollila, P. Pilleri, V. Sridhar, S. Maurice, R. C. Wiens, Optical calibration of the SuperCam instrument body unit spectrometers. *Appl. Optics***, 61**, 2967–2974 (2022).

66. C. Royer, F. Poulet, J.-M. Reess, C. Pilorget, V. Hamm, T. Fouchet, S. Maurice, O. Forni, R. C. Wiens, Pre-launch radiometric calibration of the infrared spectrometer onboard SuperCam for the Mars2020 rover. *Rev. Sci. Instrum.* **91**, 063105 (2020).

67. L. Mandon, P. Beck, C. Quantin-Nataf, E. Dehouck, A. Pommerol, Z. Yoldi, R. Cerubini, L. Pan, M. Martinot, V. Sautter, Martian meteorites reflectance and implications for rover missions. *Icarus* **366**, 114517 (2021).

68. L. Mandon, C. Quantin-Nataf, C. Royer, P. Beck, T. Fouchet, J. R. Johnson, O. Forni, F. Montmessin, C. Pilorget, F. Poulet, S. Le Mouelic, E. Dehouck, O. Beyssac, A. Brown, J. Tarnas, S. Maurice, R. C. Wiens; SuperCam team, Infrared reflectance of rocks and regolith at Jezero crater: One year of SuperCam Observations. *Lunar Planet Sci.* **LIII**, 1631 (2022).

69. G. Montagnac, "Raman spectra of some chlorate minerals" (SSHADE/REAP, OSUG Data Center, Dataset/Spectral Data, 2000). doi:10.26302/SSHADE/EXPERIMENT_GM_20220122, www.sshade.eu/data/EXPERIMENT_GM_20220122.

70. C. Cornwall, J. L. Bandfield, T. N. Titus, B. C. Schrieber, D. R. Montgomery, Physical abrasion of mafic minerals and basalt grains: Application to martian aeolian deposits. *Icarus* **256**, 13–21 (2015).

71. M. D. Higgins, Measurement of crystal size distributions. *Am. Mineral.* **85** 1105–1116 (2000).

72. D. J. Morgan, D. A. Jerram, On estimating crystal shape for crystal size distribution analysis. *J. Volcanol. Geotherm. Res.* **154**, 1–7 (2006).

73. P. J. Gasda, R. B. Anderson, M. Dubey, A. Cousin, O. Forni, S. M. Clegg, A. M. Ollila, N. Lanza, R. C. Wiens, Multivariate and ensemble manganese calibration models for SuperCam, in *53rd Lunar and Planetary Science Conference*, The Woodlands, Texas, 7 to 11 March 2022 abstract #1646, The Lunar and Planetary Institute (2022).

74. G. J. Taylor, The bulk composition of Mars. *Chem. Erde* **73**, 401–420 (2013).

75. J. L. Bishop, Visible and near-infrared reflectance spectroscopy, in *Remote Compositional Analysis: Techniques for Understanding Spectroscopy, Mineralogy, and Geochemistry of Planetary Surfaces* (Cambridge Univ. Press, 2019), pp. 68–101.

76. J. L. Bishop, M. D. Lane, M. D. Dyar, A. J. Brown, Reflectance and emission spectroscopy study of four groups of phyllosilicates: Smectites, kaolinite-serpentines, chlorites and micas. *Clay Miner.* **43**, 35–54 (2008).

77. J. Hanley, V. F. Chevrier, B. L. Davis, T. S. Altheide, A. Francis, Reflectance spectra of low-temperature chloride and perchlorate hydrates and their relevance to the martian surface, in The New Martian Chemistry Workshop, abstract #8010, the Lunar and Planetary Institute (2009).

78. C. M. Pieters, T. Hiroi, RELAB (Reflectance Experiment Laboratory): A NASA multiuser spectroscopy facility, in *Lunar Planetary Science Conference*, XXXV, abstract #1720, the Lunar and Planetary Institute (2004).

79. E. L. Scheller, J. R. Hollis, E. L. Cardarelli, A. Steele, L. W. Beegle, R. Bhartia, P. Conrad, K. Uckert, S. Sharma, B. L. Ehlmann, W. J. Abbey, S. A. Asher, K. C. Benison, E. L. Berger, B. L. Bleefeld, A. S. Burton, S. V. Bykov, L. DeFlores, K. A. Farley, D. M. Fey, T. Fornaro, A. C. Fox, M. Fries, K. Hickman-Lewis, J. E. Huggett, S. Imbeah, L. C. Kah, P. Kelmen, M. R. Kennedy, T. Kizovski, C. Lee, F. M. McCubbin, K. Moore, B. E. Nixon, C. R. Sanchez-Vahamonde, R. D. Roppel, S. Siljeström, J. I. Simon, S. O. Shkolyar, D. Shuster, R. J. Smith, K. S. Morgan, K. Steadman, A. Werynski, A. J. Williams, B. Wogsland, R. C. Wiens, K. H. Williford, K. Winchell, R. Wingling, A. Yanchilina; SHERLOC Team, Aqueous alteration processes and implications for organic geochemistry in Jezero crater, Mars, this volume (2022).